Helge Weydahl

Dynamic behaviour of fuel cells

Doctoral thesis
for the degree of doctor scientiarum

Trondheim, August 2006

Norwegian University of Science and Technology
Faculty of Natural Sciences and Technology
Department of Materials Science and Engineering

NTNU
Innovation and Creativity

NTNU
Norwegian University of Science and Technology

Doctoral thesis
for the degree of doctor scientiarum

Faculty of Natural Sciences and Technology
Department of Materials Science and Engineering

ISBN 82-471-7942-3 (printed version)
ISBN 82-471-7941-5 (electronic version)
ISSN 1503-8181

Doctoral theses at NTNU, 2006:94

Printed by NTNU-trykk

Acknowledgements

First of all, I wish to honour the memory of Professor Georg Hagen who was my supervisor until his passing in October 2004. His optimism and continuing enthusiasm during the course of his illness was an inspiration to us all. He is dearly missed.

I would like to thank my supervisors Dr. Børre Børresen and Professor Svein Sunde for their guidance and leadership through the course of my degree. I am most grateful to Dr. Steffen Møller-Holst who was my co-supervisor for the project. Thanks for showing me the importance of collaboration and joint efforts. I am also deeply thankful to Dr. Ann Mari Svensson, Dr. Trygve Burchardt and Dr. Knut Bech for their invaluable help and initiative.

I would also like to thank Dr. Steffen Møller-Holst, MSc Nils Arild Ringheim and MSc Ingve Sørfonn for initiating a visionary project and the Research Council of Norway and Aker Kværner Power and Automation Systems AS for providing the funding. Researchers at SINTEF Materials Technology and SINTEF Energy Research AS are also acknowledged for valuable contributions to the project.

Many thanks to Kjell Røkke and Martha Bjerknes for assisting me in solving practical and administrative challenges. Thanks also to Jan Ole Sundli at the instrument workshop and personnel at NTNU's workshop for providing bespoke equipment for my experiments.

I am very grateful to my colleagues at the department for informative discussions and an inspiring working environment. I would also like to thank Federico Zenith, who was my office-mate during my years in K4-212, for interesting discussions and frequent updates on Italian politics.

Many thanks to my friends and family in Trondheim for a memorable time. Thanks for all the fun! Finally, I would like to thank my parents for their support and prayers.

Summary

This thesis addresses the dynamic behaviour of proton exchange membrane fuel cells (PEMFCs) and alkaline fuel cells (AFCs). For successful implementation in automotive vehicles and other applications with rapidly varying power demands, the dynamic behaviour of the fuel cell is critical. Knowledge of the load variation requirements as well as the response time of the cell at load change is essential for identifying the need for and design of a buffer system.

The transient response of a PEMFC supplied with pure hydrogen and oxygen was investigated by load step measurements assisted by electrochemical impedance spectroscopy and chronoamperometry. Using an in-house designed resistance board, the uncontrolled response in both cell voltage and current upon step changes in a resistive load was observed. The PEMFC was found to respond quickly and reproducibly to load changes. Two transient processes limiting the fuel cell response were identified: i) A cathodic charge transfer process with a potential dependent response time and ii) a diffusion process with a constant response time. The diffusion transient only appeared at high current densities and was offset from the charge transfer transient by a temporarily stable plateau. Transient paths were plotted in the V-i diagram, matching a predicted pattern with overshooting cell voltage and current during a load step.

The transient response of a PEMFC was measured for various cathode gas compositions and gas utilisations (fraction of supplied reactant gas which is consumed in the fuel cell reaction). For a PEMFC operated on pure hydrogen and oxygen, the cell voltage response to current steps was fast, with response times in the range 0.01-1 s, depending on the applied current. For a PEMFC supplied with air as cathode gas, an additional relaxation process related to oxygen transport caused a slower response (appr. 0.1-2 s depending on the applied current). Response curves up to appr. 0.01 s were apparently unaffected by gas composition and utilisation and were most likely dominated by capacitive discharge of the double layer and reaction with surplus oxygen residing in the cathode. The utilisation of hydrogen had only a minor effect on the response curves, while the utilisation of air severely influenced the transient PEMFC response. Results suggested that air flow rates should be high to obtain rapid PEMFC response.

The load-following capability of a single PEMFC was studied by measuring the cell voltage response to a sinusoidal current load with large amplitudes. Effects on the cell voltage response when varying the DC value, amplitude and frequency of the current load were recorded. The load-following capability of the PEMFC was excellent in the operating range where changes in cell voltage were dominated by ohmic losses. No hysteresis in the cell voltage response was observed in this range for frequencies up to 1-10 Hz. In the operating range where changes in cell voltage were dominated by activation losses, hysteresis appeared at lower frequencies (>0.1 Hz) due to sluggish response in the voltage range near open circuit voltage. The increased mass transport limitation imposed when supplying the PEMFC with air caused hysteresis to appear at lower frequencies than for oxygen (above 0.1 Hz, compared to 1-10 Hz for oxygen).

The dynamic behaviour of an AFC supplied with pure oxygen and hydrogen was investigated by load step measurements assisted by electrochemical impedance spectroscopy (EIS). Load step measurements were carried out using an in-house designed resistance board which gave step changes in a purely resistive load. Resistive load steps between various operating points along the polarisation curve were carried out and the corresponding transient response in cell voltage and current was measured. The transient cell response consisted of an initial ohmic drop followed by a relaxation towards the new steady state. The observed response was slower at higher cell voltages. Measured response times varied on a time scale of appr. 10 ms to 10 s, depending on the initial and final voltages. Results from EIS measurements suggested that the potential dependent response time stemmed from the charge transfer reaction at the cathode. Transient response curves were plotted in the V-i diagram and shown to follow a pattern determined by the load resistance and ohmic resistance of the AFC. Results showed that when supplied with pure oxygen and hydrogen, the AFC responded sufficiently fast for automotive applications.

An iso-thermal, one-dimensional, transient model of an AFC cathode was developed, based on mass balances for oxygen and ionic species and flooded-agglomerate theory. Model results show the coupled effects of oxygen diffusion,

ion transport and propagation of local electrode potential on the response in current density to a cathodic step in electrode potential. For a set of base case parameters, oxygen diffusion and potential propagation, with characteristic time constants of 0.30 and 0.11 ms, respectively, dominated the current response up to appr. 1 ms, while the slower ion diffusion with time constant 5.0 s controlled the final relaxation towards steady state at appr. 60 s. A smaller agglomerate radius and electrode thickness and a smaller double layer capacitance gave faster electrode response. For a cathodic step in electrode potential, an overshoot in faradaic current appeared around 0.5 ms. This overshoot was related to an initially higher oxygen concentration in the agglomerates, but was masked by capacitive current for base case parameters. Simulated response in oxygen concentration profiles suggested that the potential dependent response time found in previous studies can be related to consumption of surplus oxygen in the catalyst layer.

Contents

Chapter 1

Introduction

1.1 Fuel cells and the hydrogen economy

An increasing world population and improving standard of living in larger parts of the world require a steady increase in energy supply. The International Energy Agency projects that if current trends continue, global primary energy demand would grow by more than 50% within 2030 [1], causing a proportional increase in carbon dioxide emissions. Considering the supposed impact of human emissions on climate change and the fact that fossil fuels are a limited source of energy, a gradual incorporation of renewable energy sources and more energy-efficient technology is imperative. An additional driving force for this transition is the will to become less dependent on oil supplies from politically unstable regions. Several countries (i.e. Japan [2], USA [3] and Iceland [4]) are setting ambitious goals to increase security of energy supply and introduce renewable energy sources in a larger scale.

Renewable energy sources such as wind and solar power are low-concentration energy sources that must be collected over large and often remote areas. Also, the supply of renewable energy is heavily dependent on geographical location, weather conditions and seasonal changes. Therefore, a flexible energy carrier is required to buffer the variations in supply and provide energy where needed. Hydrogen is considered a promising candidate since it is storable and non-polluting and can be produced from practically all sources of energy.

Electric energy is regained by combination of hydrogen and oxygen in a fuel cell (Figure 1.1). A fuel cell is a device that electrochemically converts the chemical energy of a fuel, such as hydrogen, and an oxidant, such as oxygen, to electrical energy [5]. Fuel and oxidant are supplied continuously to the fuel cell as reactants are consumed. Since electricity is produced directly from the electrochemical reaction, higher efficiencies than the conventional combustion engine are typically obtained.

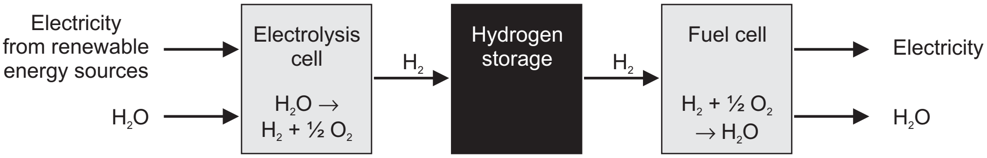

Figure 1.1: A sustainable energy system for the future, based on renewable energy sources and hydrogen as energy carrier.

Basically, a fuel cell consists of two electrodes (anode and cathode) separated by an ion conducting electrolyte [5, ch. 1.1]. At the cathode, oxygen is reduced, and at the anode, hydrogen is oxidised. In sum, the fuel cell reaction produces electricity and water. Fuel cells are categorised according to the electrolyte (Table 1.1). In the alkaline fuel cell (AFC), concentrated potassium hydroxide (KOH) is used as electrolyte, while a proton conducting polymer is used in a proton exchange membrane fuel cell (PEMFC).

The fuel cell principle was first reported by Christian Friedrich Schönbein and William Grove in 1839 [6]. Francis T. Bacon started his research into fuel cells in 1932 and developed the first large scale fuel cell in 1959 based on porous nickel electrodes and an alkaline electrolyte. During the early 1960s, Pratt & Whitney Aircraft developed power systems for the Apollo space missions based on AFC technology. The PEMFC was developed by Willard T. Grubb in 1957 and General Electric developed this technology further for the Gemini space

Technology	Electrolyte	Anode reaction	Cathode reaction
AFC	KOH	$2OH^- + H_2$ $\rightarrow 2H_2O + 2e^-$	$\frac{1}{2}O_2 + H_2O + 2e^-$ $\rightarrow 2OH^-$
PEMFC	Nafion®	$H_2 \rightarrow 2H^+ + 2e^-$	$\frac{1}{2}O_2 + 2H^+ + 2e^-$ $\rightarrow H_2O$

Table 1.1: Comparison of AFC and PEMFC technology.

missions in the early 1960s.

The oil crisis in the 1970s boosted the interest in fuel cells for terrestrial applications. A number of companies and governmental organisations were involved in research and development of various fuel cell technologies. During the 1980s and 90s, prototypes for a wide range of fuel cell powered products were developed, including stationary power generation, fuel cell cars and portable electronics. Today, impacts of global warming and limited oil resources are pushing fuel cells further towards commercialisation.

1.2 Dynamic behaviour of fuel cells

Investigations of fuel cell technology have mainly focused on reducing cost and improving stationary performance [7–10]. For successful implementation in applications with rapidly varying power demands, such as automobiles and portable electronics, also the dynamic behaviour of fuel cells is critical. PEMFCs are favoured for such applications due to their low operating temperature and high power density [11], but also the AFC has been proposed for automotive applications [12]. A rapid increase in power demand must be accompanied by a corresponding increase in power supply, either from the fuel cell or from energy buffers such as capacitors and batteries. Such auxiliary components add cost, space and weight to the application and should be carefully sized with regard to the dynamic characteristics of the fuel cell. If energy buffers do not provide sufficient compensation for power deficiencies, electronic components in the application may be damaged or malfunction. Rapid power changes may also be harmful to the fuel cell itself. Thus, a detailed characterisation of transient processes in fuel cells is critical for an adequate design of the buffer system. The dynamic behaviour of fuel cells is the topic of this thesis.

Another aspect is the influence of operating conditions on the dynamic response. Balance-of-plant (BoP) components controlling the supply of reactant gases, heating, humidification etc. must be designed to accommodate optimal fuel cell performance for the given application. BoP components also add to the complexity of the system and should be carefully selected. Detailed knowledge of operating conditions and their effect on transient fuel cell response is necessary for identifying an adequate system design.

Dynamic processes in fuel cells cover a wide time scale. Figure 1.2 categorises the various dynamic processes in PEMFCs and shows the approximate

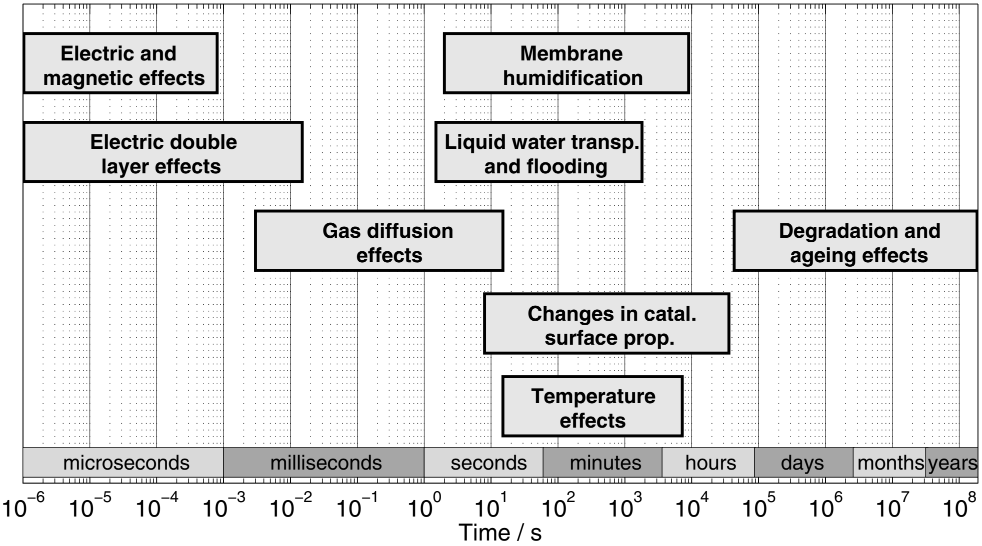

Figure 1.2: Dynamic processes in PEMFCs.

time range where they appear. For a step in cell current, the initial ohmic drop in cell voltage is determined by the internal ohmic resistance of the fuel cell. This change takes place instantaneously, but may be disturbed by electric and magnetic effects in cables and connections. A sudden change in electrode polarisation gives a discharge of the charge double layer of the electrodes and an increased reaction rate. An increased reaction rate changes the partial pressure of reactant gases in the catalytic layers, gas diffusion layers and gas channels, typically on a time scale of a few seconds [13–23]. Water produced in the electrochemical reaction also causes transient effects. In AFCs, water is produced in the anode and consumed in the cathode, possibly affecting electrolyte concentration and gas composition. In PEMFCs, water is produced in the cathode and transported through the gas diffusion layer or into the membrane [13, 20, 24–27]. Cathode flooding caused by accumulated liquid water in the cathode gas diffusion layer or gas channel takes place on a time scale of minutes [24]. In PEMFCs, product water also affects the water content of the membrane, which is decisive for the membrane conductivity [23, 28–37]. Humidification and dehumidification of the membrane occur on a time scale of seconds or several minutes, depending on the operating conditions of the fuel cell.

The active area in the electrodes can be covered by catalyst poisons such as CO [38–42] or by an oxide layer [43] giving rise to performance variations on a time scale of minutes to hours. Heat generated in the fuel cell changes its internal temperature. The relaxation to a new steady state temperature distribution occurs within minutes or hours and is determined by the thermal properties of the fuel cell materials, reactant gas flow rates, ambient temperature, etc. [19,30,44–48]. Local temperature changes are likely to occur much faster. During long-term operation at certain operating conditions, structural changes to the electrodes and electrolyte may arise, giving non-restorable performance degradation.

Compared to steady state analyses of PEMFC and AFC performance, the dynamic behaviour of fuel cells has gained very little attention in the open literature. Especially, reports on transient response measured on a sub-second time scale are scarce.

1.3 Problem statement

This thesis was written as a part of the project “Dynamic behaviour of fuel cell systems” aiming at a better understanding of the processes limiting the transient response of fuel cells. PEMFCs and AFCs were chosen as focus technologies within the project since both have been suggested for automotive applications where the dynamic behaviour is critical. Based on the motivation stated in the previous section, a set of key questions were formulated, setting the focus for the present thesis:

1. How fast do fuel cells respond to a load change?
2. Which processes limit the dynamic response of the fuel cell?
3. How does mass transport influence the dynamic response?
4. How well does the fuel cell follow a given load profile?
5. How do local changes in mass transport and potential propagation contribute to the total transient response?

Questions 1 through 4 were addressed for the PEMFC technology, and questions 1, 2 and 5 were addressed for the AFC technology.

1.4 Methodology

Experimental measurements constitute the main part of the work. Even though fuel cell stacks are typically used in real applications, measurements were carried out on single AFCs and PEMFCs in order to reveal the more fundamental limitations of the cells and avoid the complexity of a complete stack. For practical reasons, measurements were carried out near ambient temperature and pressure, even though pressurised systems at working temperatures 50-100 °C are common in automotive PEMFC applications (50-200 °C for AFCs [5, pg. 11]).

Measurements of sub-second fuel cell response require high-resolution data acquisition and controllable loads with very short switching times. Both in-house designed and commercially available equipment were used to carry out necessary measurements.

The dynamic fuel cell behaviour was tested by imposing various transient load profiles on the fuel cell and measuring the resulting response in cell voltage and current. Potential steps, current steps, steps in an ohmic load and a continuous, sinusoidal current were applied. By measuring the transient fuel cell response under various gas flow regimes, the effects of mass transport were assessed.

Electrochemical impedance spectroscopy (EIS) is a powerful tool to separate and identify physical processes with different relaxation times [49]. Using mathematical models or equivalent circuits representing these processes, qualitative and quantitative information can be extracted. Even though EIS only captures the transient behaviour of the fuel cell near a steady-state operating point, it gives valuable insight into the dynamic processes dominating at the given operating point.

Local dynamic processes and the coupling of these are difficult, if not impossible to measure. A mathematical model illustrates how various processes contribute to the dynamic response of the fuel cell. Question 5 in the problem statement was therefore addressed using a mathematical model.

1.5 Outline of the thesis

The thesis consists of five papers which have been or will be submitted in their present form to scientific journals. All papers are self-contained and can be read in any order. Repetition of a few elements was unavoidable in order to make each paper more readable. Contributions of co-authors to each paper are specified below.

Paper 1 addresses the autonomous response of a PEMFC to load steps in a purely ohmic load. This paper addresses questions 1 and 2 in the problem statement (ref. Section 1.3). Parts of this paper were presented at the 206th Meeting of the Electrochemical Society, October 2004, and the full paper was submitted to Journal of the Electrochemical Society, December 2005. Hagen advised the experimental work and contributed to data interpretation. Møller-Holst and Børresen advised the experimental work, contributed to data interpretation and reviewed all iterations of the paper.

In **Paper 2**, the effect of gas flow rate and gas composition on the dynamic response of a PEMFC is investigated. This paper addresses questions 1, 2 and 3 in the problem statement. Møller-Holst and Børresen advised the experimental work, contributed to data interpretation and reviewed all iterations of the paper.

Paper 3 focuses on the load-following capability of a PEMFC and addresses questions 3 and 4 in the problem statement. Møller-Holst and Børresen advised the experimental work, contributed to data interpretation and reviewed all iterations of the paper.

In **Paper 4** the same approach as in Paper 1 is applied to an AFC, adressing questions 1 and 2 in the problem statement. Different parts of this paper were presented as posters at the 1st European Hydrogen Energy Conference, 9th Ulm Electrochemical Talks and 2004 Fuel Cell Seminar. Svensson assisted in the analysis of impedance spectra, electrodes were manufactured by Lervik and Burchardt assisted in designing the AFC housing and contributed to data interpretation. Hagen advised the experimental work and contributed to data interpretation. Møller-Holst and Børresen advised the experimental work, contributed to data interpretation and reviewed all iterations of the paper.

Paper 5 presents a transient model of an AFC cathode and addresses questions 1, 2, 3 and 5 of the problem statement. Svensson and Sunde contributed to the model build-up and data interpretation and reviewed all iterations of the paper.

Conclusions and suggestions for further work are given in the last two chapters.

References

[1] IEA Energy Information Centre, www.iea.org, last visited May 2006.

[2] Agency for Natural Resources and Energy, Japan, www.enecho.meti.go.jp/english/policy/, last visited May 2006.

[3] FCVT Program of the US Department of Energy, www.eere.energy.gov/vehiclesandfuelcells/, last visited May 2006.

[4] Icelandic New Energy, www.newenergy.is, last visited May 2006.

[5] J. Larminie and A. Dicks, *Fuel cell systems explained*, John Wiley & Sons, Ltd., Hoboken (2000).

[6] G. Sandstede, E. J. Cairns, V. S. Bagotsky, and K. Wiesener, *Handbook of fuel cells*, vol. 1, chap. 12, John Wiley & Sons, Ltd., West Sussex, England (2003).

[7] K. B. Prater, *J. Power Sources*, **51**, 129 (1994).

[8] V. Mehta and J. S. Cooper, *J. Power Sources*, **114**, 32 (2003).

[9] G. F. McLean, T. Niet, S. Prince-Richard, and N. Djilali, *Int. J. Hydrogen Energy*, **27**, 507 (2002).

[10] P. Gouérec, L. Poletto, J. Denizot, E. Sanchez-Cortezon, and J. H. Miners, *J. Power Sources*, **129**, 193 (2004).

[11] S. Gottesfeld and T. A. Zawodzinski, in *Advances in Electrochemical Science and Engineering*, R. C. Alkire and D. M. Kolb, editors, vol. 5, pp. 195–301, Wiley-VCH, Weinheim, Germany (1997).

[12] K. Kordesch, V. Hacker, J. Gsellmann, M. Cifrain, G. Faleschini, P. Enzinger, R. Fankhauser, M. Ortner, M. Muhr, and R. R. Aronson, *J. Power Sources*, **86**, 162 (2000).

[13] D. Natarajan and T. V. Nguyen, *J. Electrochem. Soc.*, **148**, A1324 (2001).

[14] D. J. L. Brett, S. Atkins, N. P. Brandon, V. Vesovic, N. Vasileiadis, and A. R. Kucernak, *Electrochem. Comm.*, **3**, 628 (2001).

[15] J. M. Stockie, K. Promislow, and B. R. Wetton, *Int. J. Numer. Meth. Fluids*, **41**, 577 (2003).

[16] S. Um and C. Wang, *J. Power Sources*, **125**, 44 (2004).

[17] S. Kim, S. Shimpalee, and J. W. Van Zee, *J. Power Sources*, **135**, 110 (2004).

[18] S. Kim, S. Shimpalee, and J. W. Van Zee, *J. Power Sources*, **137**, 43 (2004).

[19] Y. Shan and S.-Y. Choe, *J. Power Sources*, **145**, 30 (2005).

[20] Q. Dong, J. Kull, and M. M. Mench, *J. Power Sources*, **139**, 106 (2005).

[21] S. Kim, S. Shimpalee, and J. W. Van Zee, *J. Electrochem. Soc.*, **152**, A1265 (2005).

[22] W.-M. Yan, C.-Y. Soong, F. Chen, and H.-S. Chu, *J. Power Sources*, **143**, 48 (2005).

[23] Y. Wang and C.-Y. Wang, *Electrochim. Acta*, **50**, 1307 (2005).

[24] W. He, G. Lin, and T. V. Nguyen, *AIChE J.*, **49**, 3221 (2003).

[25] M. M. Mench, C. Y. Wang, and M. Ishikawa, *J. Electrochem. Soc.*, **150**, A1052 (2003).

[26] R. Eckl, W. Zehtner, C. Leu, and U. Wagner, *J. Power Sources*, **138**, 137 (2004).

[27] C. Ziegler, H. M. Yu, and J. O. Sundmacher, *J. Electrochem. Soc.*, **152**, A1555 (2005).

[28] T. Okada, G. Xie, and Y. Tanabe, *J. Electroanal. Chem.*, **413**, 49 (1996).

[29] H. P. L. H. van Bussel, F. G. H. Koene, and R. K. A. M. Mallant, *J. Power Sources*, **71**, 218 (1998).

[30] S. O. Morner and S. A. Klein, *J. Solar Energy Eng.*, **123**, 225 (2001).

[31] J. F. Moxley, S. Tulyani, and J. B. Benziger, *Chem. Eng. Science*, **58**, 4705 (2003).

[32] J. Benziger, E. Chia, J. Moxley, C. Teuscher, and I. G. Kevrekidis, *AIChE J.*, **50**, 1889 (2004).

[33] E.-S. J. Chia, J. B. Benziger, and I. G. Kevrekidis, *AIChE J.*, **50**, 2320 (2004).

[34] J. Benziger, E. Chia, J. F. Moxley, and I. G. Kevrekidis, *Chem. Eng. Science*, **60**, 1743 (2005).

[35] F. Chen, Y. Su, C. Soong, W. Yan, and H. Chu, *J. Electroanal. Chem.*, **566**, 85 (2004).

[36] F. Chen, H.-S. Chu, C.-Y. Soong, and W.-M. Yan, *J. Power Sources*, **140**, 243 (2004).

[37] W. Friede, S. Raël, and B. Davat, *IEEE T. Power Electr.*, **19**, 1234 (2004).

[38] C. A. Schiller, F. Richter, E. Gülzow, and N. Wagner, *Phys. Chem. Chem. Phys.*, **3**, 2113 (2001).

[39] M. Murthy, M. Esayian, A. Hobson, S. MacKenzie, W. Lee, and J. W. Van Zee, *J. Electrochem. Soc.*, **148**, A1141 (2001).

[40] M. Murthy, M. Esayian, W. Lee, and J. W. Van Zee, *J. Electrochem. Soc.*, **150**, A29 (2003).

[41] K. K. Bhatia and C.-Y. Wang, *Electrochim. Acta*, **49**, 2333 (2004).

[42] J. Zhang, J. D. Fehribach, and R. Datta, *J. Electrochem. Soc.*, **151**, A689 (2004).

[43] F. A. Uribe and T. A. Zawodzinski, Jr., *Electrochim. Acta*, **47**, 3799 (2002).

[44] K. Strasser, *J. Power Sources*, **37**, 209 (1992).

[45] J. C. Amphlett, R. F. Mann, B. A. Peppley, P. R. Roberge, and A. Rodrigues, *J. Power Sources*, **61**, 183 (1996).

[46] W. H. Zhu, R. U. Payne, D. R. Cahela, and B. J. Tatarchuk, *J. Power Sources*, **128**, 231 (2004).

[47] X. Xue, J. Tang, A. Smirnova, R. England, and N. Sammes, *J. Power Sources*, **133**, 188 (2004).

[48] P. R. Pathapati, X. Xue, and J. Tang, *Renewable Energy*, **30**, 1 (2005).

[49] R. de Levie, *Adv. Electroch. El. Eng.*, **6**, 329 (1967).

Chapter 2

Transient response of a proton exchange membrane fuel cell

H. Weydahl[a], S. Møller-Holst[b], G. Hagen[a,†], and B. Børresen[a,c]

[a]Department of Materials Technology, NTNU, NO-7491 Trondheim, Norway
[b]SINTEF Materials and Chemistry, NO-7465 Trondheim, Norway
[c]Current affiliation: Statoil ASA, NO-7005 Trondheim, Norway

Abstract: The transient response of a proton exchange membrane fuel cell (PEMFC) supplied with pure hydrogen and oxygen was investigated by load step measurements assisted by electrochemical impedance spectroscopy and chronoamperometry. Using an in-house designed resistance board, the uncontrolled response in both cell voltage and current upon step changes in a resistive load was observed. The PEMFC was found to respond quickly and reproducibly to load changes. Two transient processes limiting the fuel cell response were identified: i) A cathodic charge transfer process with a potential dependent response time and ii) a diffusion process with a constant response time. The diffusion transient only appeared at high current densities and was offset from the charge transfer transient by a temporarily stable plateau. Transient paths were plotted in the V-i diagram, matching a predicted pattern with overshooting cell voltage and current during a load step.

[†] This paper is dedicated to the late Prof. Georg Hagen who contributed significantly to this work before his passing October 2004.

2.1 Introduction

Fuel cell technology may be utilised in a wide range of applications, from portable electronics to stationary power generation. For certain applications (e.g., vehicles) where the power requirement varies rapidly, the dynamic behaviour of the fuel cell is critical. If the fuel cell is sufficiently fast to supply the required power, one can cut down on the auxiliary buffer system (supercapacitors, batteries, etc.) and thereby save cost, weight and space.

The dynamic performance of proton exchange membrane fuel cells (PEMFCs) have been reported to some degree in the open literature. Dynamic processes have been studied by both experimental approaches and modelling. Most of the experimental studies consider slow processes, such as liquid water accumulation in the gas diffusion layer [1], changes in CO coverage on the anode [2] and relaxation of membrane water content [3–5]. The reported relaxation time of these processes ranges from about one minute to several hours. Some of the faster processes that have been studied experimentally include changes in cathode gas composition upon current steps [6] and over- and undershooting currents upon voltage steps [7–9]. A few studies report the dynamic behaviour of PEMFC stacks [10–14].

Dynamic modelling approaches usually combine a steady-state electrochemical model with time dependent mass balances [15–18]. In such approaches the modelled fuel cell response is governed by gas transport transients. Some authors also include the capacitive effect of the charge double layer in the electrochemical model, thereby providing a more realistic description of the initial fuel cell response [19–21]. Response in cell voltage or current to a load change have been simulated in several studies [15–17, 19–22], while some studies address more specific processes such as the effect of ripple currents [18], dynamic behaviour of water transport and water balance in the membrane [23–25], temperature transients [20, 26], effect of changing humidification and temperature of reactant gases [12, 27] and transport processes in the gas diffusion layer [28, 29].

Some studies take a more applied approach by assessing the dynamic interaction between PEMFCs and system components such as reformers [30–32], wind turbines [33] or batteries [10], while others simulate PEMFC operation in residential houses [34, 35] or automotive applications [36–41].

This literature review shows that many aspects of dynamic PEMFC behaviour have been studied, but response in the sub-second range is scarcely documented. Knowledge of fuel cell response in this time range is critical for applications where the load changes rapidly with time, and where over- or undershooting power can damage the application. Such knowledge will further provide design criteria for required buffer systems. If the PEMFC responds sufficiently fast to load changes, auxiliary buffer systems may even become obsolete.

To our best knowledge, only Van Zee and co-workers [7–9] have measured single PEMFC response with a time resolution sufficiently high to cover the time range below 1 second: They measured the effect of e.g., stoichiometry, fuel dilution and flow field design on the transient response of a single PEMFC. Their main focus was the over- and undershooting currents observed at low stoichiometry, but their results also showed that, when supplied with excess amounts of reactant gases, the PEMFC responded as fast as the electronic load that was used to control the cell voltage. This observation stresses the importance of using a load with sufficiently short switching time when measuring sub-second PEMFC response, otherwise you will only measure the dynamic behaviour of the load itself.

The aim of this study is to investigate how fast PEMFCs respond to load changes under minimal mass transport limitations and identify the processes which determine the observed response pattern. An in-house designed, passive load with short switching time was used to reveal the autonomous response of the PEMFC, undisturbed by external control loops. To minimise mass transport limitations, the PEMFC was supplied with pure oxygen in excess. This is not a realistic condition in most fuel cell applications, but simplifies the response pattern for easier interpretation. Load step measurements were assisted by electrochemical impedance spectroscopy (EIS) and chronoamperometry to identify response limiting processes.

2.2 Experimental

2.2.1 Hardware and experimental conditions

A membrane electrode assembly from W. L. Gore & Associates (PRIMEA® 5561, Pt/Ru anode 0.45 mg cm^{-2}, Pt cathode 0.4 mg cm^{-2}, 25 μm nominal membrane thickness) was sandwiched between two gas diffusion layers from E-TEK (ELAT® carbon only). The geometric electrode area was 6.25 cm^2. The membrane electrode assembly and gas diffusion layers were mounted in a fuel cell housing from ElectroChem Inc. (EFC05-01SP-REF).

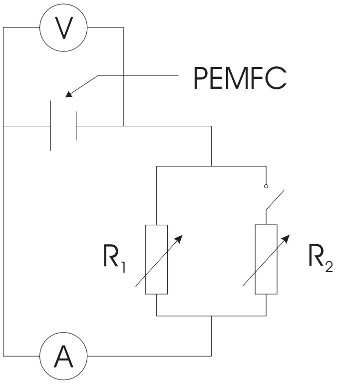

Figure 2.1: Circuit diagram for the resistance step measurements.

The electrodes were supplied with constant gas flows of hydrogen (99.999% purity) and oxygen (99.5% purity). To avoid any effects of fuel starvation, both gases were supplied in excess so that fuel utilisation never exceeded 50%. The gases were humidified at room temperature in separate sparging bottles. The temperature of the cathode hardware was monitored by a thermocouple from Omega®. No external heating was applied, and the operating temperature was 26 ± 1 °C during load step measurements, 29 ± 2 °C during EIS and 32 ± 1 °C during chronoamperometry. These temperature variations were considered too small to affect the results significantly.

2.2.2 Steps in external load resistance

Step changes in the external load resistance were obtained using an in-house designed resistance board consisting of a parallel combination of two Kool-Pak® power resistors, where one of the parallel branches was connected and disconnected using an IRF3704 MOSFET. A circuit diagram of the experimental set-up is shown in Figure 2.1. When R_2 is disconnected, the external load resistance, R_L, equals R_1, and when R_2 is connected, $R_L = R_1R_2/(R_1 + R_2)$. The transistor was controlled by a 50 MHz pulse generator from Wavetek (Model 166) via an ICL7667 CPL driver circuit powered by a PULS 36 W power supply. The transistor responded by connecting or disconnecting the R_2 branch within 30 μs revealing the unregulated response in both cell voltage and current upon a step change in a purely resistive load. The resistance in each branch was selected with a switch knob, so that various external load resistances could be realised.

The unregulated response in cell voltage and current was measured with an oscilloscope from Pico Technology Ltd (ADC-212). The current was measured with a Tektronix A6302 current probe connected to the oscilloscope via a Tektronix TM502A current probe amplifier.

2.2.3 Electrochemical impedance spectroscopy

EIS was carried out on a two-electrode setup using an IM6e electrochemical workstation and PP200 add-on module from ZAHNER® elektrik. The ac signal had an amplitude of 5 mV and a frequency range from 100 kHz to 100 mHz. The impedance was measured at 8 cell voltages (0.95, 0.90, 0.85 and 0.80-0.40 V with step intervals of 0.10 V). A complex non-linear least-squares fitting program, LEVM version 7.0, was used to fit equivalent circuit parameters to the measured impedance.

2.2.4 Chronoamperometry

Chronoamperometry was carried out on a two-electrode set-up with a PG-STAT20 potentiostat and BSTR 10A current booster, both from AUTOLAB®. During these tests, the cell voltage was kept at 0.990 V (close to the open circuit voltage) for at least 10 seconds before the next cell voltage was assessed. Potential steps from 0.990 V to six lower cell voltages (0.90, 0.80,... and 0.40 V) were investigated.

2.3 Theory and analysis methods

2.3.1 Steps in external load resistance

The fuel cell voltage is determined by the reversible voltage and the various losses in the fuel cell. These losses are typically related to ohmic resistance in the fuel cell hardware, reaction overpotentials of both anode and cathode and reactant transport limitations. The characteristics of the fuel cell response is determined by the processes involved and their corresponding relaxation times.

Typical response curves for cell voltage and current upon a step decrease in external load resistance are sketched in Figure 2.2. When the external load resistance, R_L, is instantaneously reduced, the cell current instantaneously

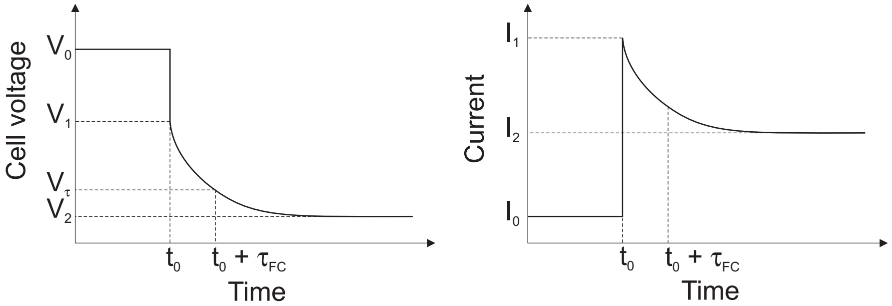

Figure 2.2: Sketch of typical transient responses in cell voltage (left) and current (right) upon a step change from high to low external load resistance (not to scale).

increases from I_0 to I_1. This gives an instantaneous drop in the cell voltage from V_0 to V_1 due to the ohmic resistance of the fuel cell. Ohm's law applies, giving $(V_1 - V_0)/(I_1 - I_0) = -R_\Omega$, where R_Ω is the ohmic resistance of the fuel cell.

After the ohmic drop, cell voltage relaxes towards its new steady state value, V_2. Since the external load is purely resistive, the current relaxes towards its new steady state value, I_2, at the same rate as the cell voltage, since $I(t) = V(t)/R_L$, according to Ohm's law.

As a measure of the fuel cell response time, τ_{FC} is used. This quantity is the time it takes for the cell voltage to decrease from V_1 to V_τ, where the value of V_τ is implicitly given by

$$\left| \frac{V_\tau - V_2}{V_1 - V_2} \right| = e^{-1} \tag{2.1}$$

where e is Euler's number. Thus, τ_{FC} corresponds to the time constant of exponential decay, even though the observed response curves were not purely exponential.

Since the switching time of the transistor was 30 μs, V_1 and I_1 were determined by linearly extrapolating the curve elements between 30 and 90 μs back to $t = 0$.

As shown in Figure 2.3 the theoretical response in cell voltage and current can be plotted in the V-i diagram, showing deviation from the polarisation curve, as reported previously by our group [42]. As interpreted by Zenith et al. [43], the instantaneous ohmic drop will follow a straight line with slope $-R_\Omega$

from (V_0, I_0) to (V_1, I_1), according to Ohm's law. Constant load resistance, R_L, is represented by straight lines through origo. The relaxation towards steady state from (V_1, I_1) to (V_2, I_2) will follow this line since $V(t) = R_L I(t)$. Thus (V_1, I_1) is found as the intersection between $R_L I$ and the straight line from V_0 with slope $-R_\Omega$.

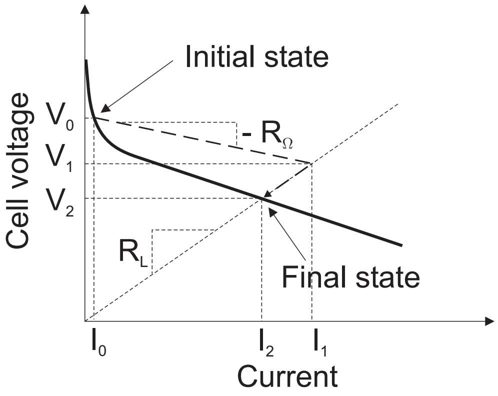

Figure 2.3: Sketch of transient path (dashed line) between two steady-state operating points on the polarisation curve (thick solid line) when the external load resistance is changed from a high value V_0/I_0 to a lower value $V_2/I_2 = R_L$. R_Ω is the ohmic resistance of the fuel cell. Remaining symbols are explained in Figure 2.2.

When controlling cell voltage or current by using a potentiostat, the transient paths will have a significantly different shape, as shown in Figure 2.4. A step in current will follow a constant current path towards the new steady state, while a step in cell voltage will follow a constant voltage path (Figure 2.4, left). The instantaneous ohmic drop in both cases will still follow a straight line from (V_0, I_0) with slope R_L. Thus, the overshoot in cell current will be much larger for a potential step than for a step in the external load resistance. This also shows that steps in cell voltage up to high cell voltages can impose a reversal of the cell current, which may cause damage to the fuel cell electrodes (Figure 2.4, right).

2.3.2 Electrochemical impedance spectroscopy

EIS was applied to identify the processes limiting the dynamic response of the PEMFC. The equivalent circuit used to model the impedance spectra has

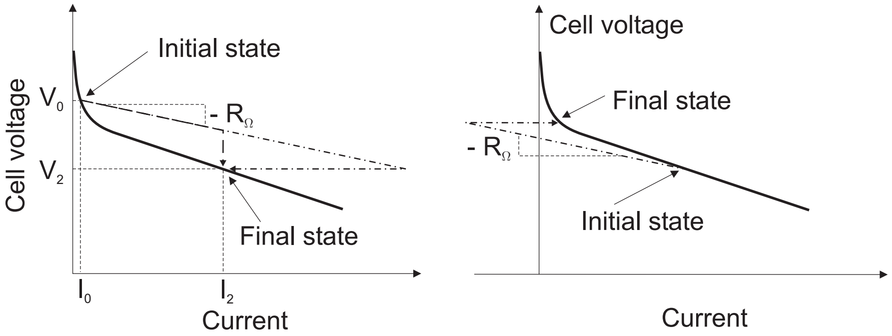

Figure 2.4: Left: Sketch of transient paths for a step in current from I_0 to I_2 (dashed line) and for a step in cell voltage from V_0 to V_2 (dash-dotted line). The steady-state polarisation curve is shown as a thick solid line. Right: Sketch of transient path for a step in cell voltage from a low to a high value, leading to temporary reversal of the current.

been proposed earlier by i.e., Ciureanu and Roberge [44] and is shown in Figure 2.5. The ohmic resistance between the electrodes, mainly due to the ohmic resistance in the membrane, is represented by R_Ω. The two parallel combinations of a resistance and a constant phase element (CPE) represent the charge transfer processes in the anode and cathode. CPEs are used instead of capacitances since measured impedance spectra contained depressed semicircles, which are typical for porous electrodes [45]. Thus, R_a and R_c represent the anode and cathode charge transfer resistances, respectively, while CPE$_a$ and CPE$_c$ correspond to the distributed double layer capacitance of the porous anode and cathode, respectively.

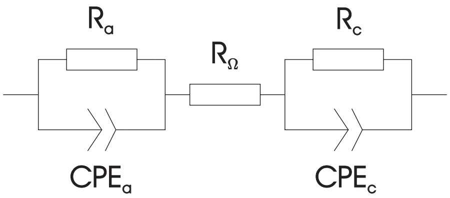

Figure 2.5: Equivalent circuit for the PEMFC [44]. R_Ω is the ohmic resistance between the electrodes, R_a and R_c are the anode and cathode charge transfer resistances, respectively, and CPE$_a$ and CPE$_c$ are the anode and cathode CPEs, respectively.

The impedance of a CPE is [46]

$$Z_{\mathrm{CPE}} = \frac{1}{T(i\omega)^{\phi}}, \tag{2.2}$$

where ω is the angular frequency, T and ϕ are the CPE fitting parameters and $i = \sqrt{-1}$. The corresponding capacitance of the cathode CPE is [46]

$$C_c = \left[T_c (R_{\Omega}^{-1} + R_c^{-1})^{\phi_c - 1} \right]^{1/\phi_c}, \tag{2.3}$$

where T_c and ϕ_c are the fitting parameters of the cathode CPE. This capacitance can be used to estimate the response time of the equivalent circuit, τ_{EC}, according to

$$\tau_{EC} = R_c C_c, \tag{2.4}$$

where the anode contribution has been assumed negligible. Equation 2.4 corresponds to the theoretical time constant of a parallel combination of a resistance and capacitance.

2.4 Results and discussion

2.4.1 Steps from high to low external load resistance

The initial response in cell voltage and current to a step decrease in the external load resistance is shown in Figure 2.6. The cell voltage apparently exhibited a fast ohmic drop followed by a slower relaxation towards the new steady state. Correspondingly, the current density jumped to a higher value and then decayed towards the new steady state. In the time domain shown, there was a pronounced potential dependence of the fuel cell response: The fuel cell responded slower for steps with higher final voltages, V_2. This relaxation process is most likely due to a charge transfer process at the cathode, as will be discussed further in Section 2.4.3.

Figure 2.7 shows steps c and d in Figure 2.6 on a logarithmic time scale. For these steps, a second relaxation process appeared at appr. 0.1 s, after a temporarily stable plateau in cell voltage and current. It was verified that the external load resistance was constant during this transient, also, the same behaviour was observed using a potentiostat (see Section 2.4.4), so the second transient was not caused by interference from the experimental set-up. It was

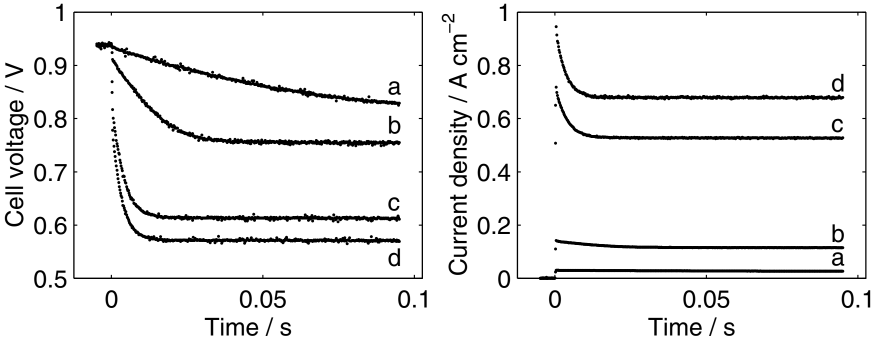

Figure 2.6: First 100 ms of the transient response in cell voltage and current density upon a step change in the external load resistance from 200 Ω to (a) 5.0 Ω, (b) 1.0 Ω, (c) 0.19 Ω and (d) 0.14 Ω.

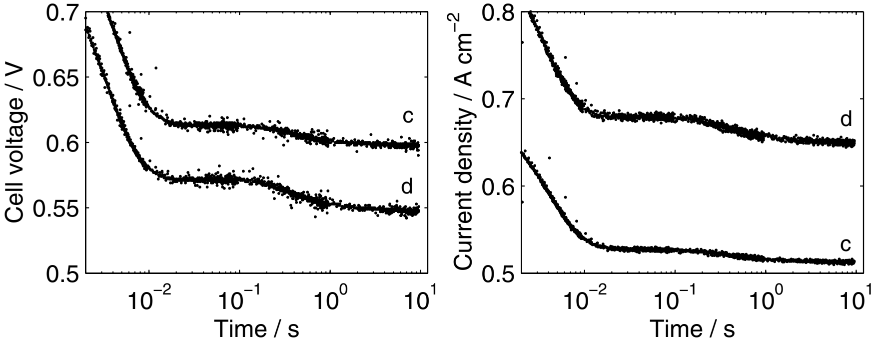

Figure 2.7: Semi-logarithmic plot of steps c and d of Figure 2.6 in a time interval between 2 ms and 10 s, showing the appearance of a second transient at appr. 0.1 s.

neither caused by insufficient supply of reactant gases, which was verified by repeating the experiment with various reactant gas flow rates.

The second transient levelled out, reaching steady state within appr. 2 s for both steps c and d. Thus, the response time for this transient showed no significant dependence on current density. The voltage drop during this transient was more pronounced for step d than for step c while it was not observed for steps a and b. Apparently, a higher current density gives a larger voltage drop during the second transient. This characteristic response pattern will be further discussed in Sections 2.4.3 and 2.4.4.

Additional step measurements were carried out for varying initial and final values of the external load resistance. A selection of these steps is shown in Figure 2.8. The same response pattern as described above was observed also for these steps: An immediate ohmic change in cell voltage and current followed by a slower relaxation, with a potential dependent response time. A second transient appeared for steps with final voltages below appr. 0.65 V, reaching steady state within 2 s. Also for these steps, the voltage drop during the second transient was more pronounced for steps with lower final cell voltages. For steps with initial voltages lower than 0.53 V, the temporarily stable plateau was absent (Figure 2.8f).

The ohmic resistance of the fuel cell, R_Ω, was calculated by dividing the ohmic voltage drop, $|V_2 - V_1|$, by the ohmic current step, $|I_2 - I_1|$, for all steps in Figure 2.8. This gave $R_\Omega = 0.12 \pm 0.01\ \Omega\ \mathrm{cm}^2$, which is within the uncertainty limits of the value found from EIS (see Section 2.4.3).

To show the potential dependence of the first transient, Equation 2.1 was used to calculate the corresponding response time of this part of the response curve. The response time was only calculated for the first transient; for steps where also a second transient appeared, the temporarily stable values of cell voltage and current were used as V_2 and I_2, respectively, and the further relaxation occurring after 100 ms was disregarded. For steps without temporarily stable values between the two transients, the response time was not calculated.

Figure 2.9 shows the response time of the first transient for steps a-d in Figure 2.8. Response times range from 0.38 s to 1.6 ms depending on the initial and final voltage. Steps with the same initial voltage, V_0, have a response time that decreases with lower final voltages, V_2. On the other hand, steps with the same *final* voltage have a response time that decreases with lower *initial* voltage. Thus, step size itself does not determine the response time, rather the voltage range where the fuel cell relaxes towards the new steady state.

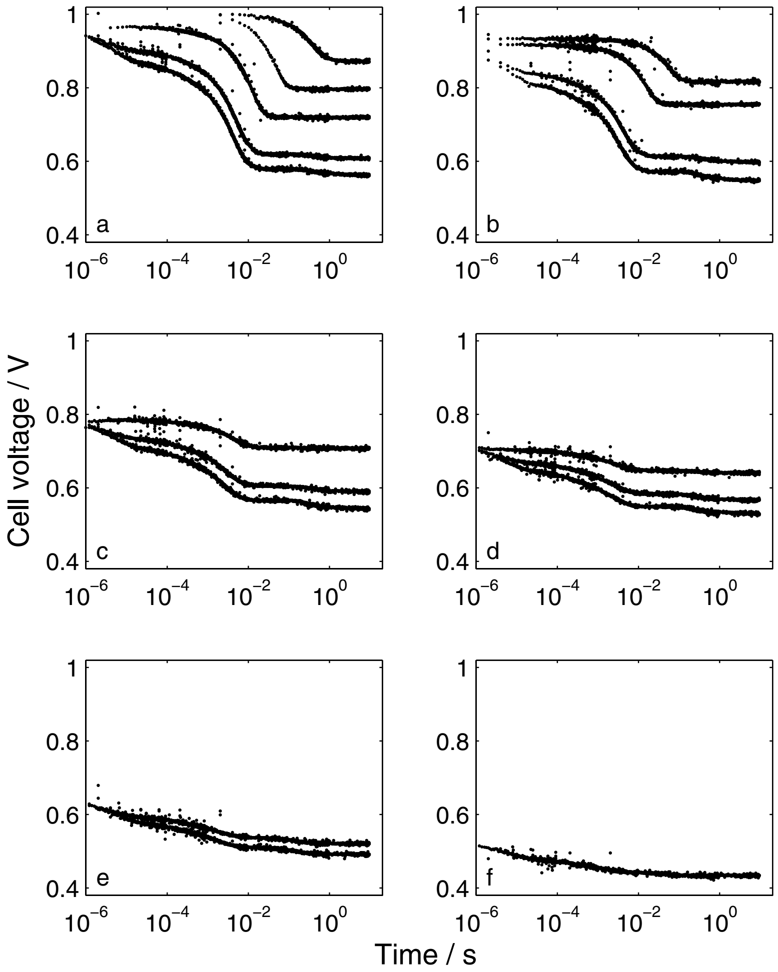

Figure 2.8: Semi-logarithmic plot of response in cell voltage to step changes in the external load resistance from a) ∞ Ω (open circuit), b) 200 Ω, c) 5.0 Ω d) 0.75 Ω e) 0.25 Ω and f) 0.10 Ω to lower resistance values.

For steps from the same initial voltage, V_0, the potential dependence of the response time was strongest for final cell voltages, V_2, above appr. 0.75 V. This corresponds to the curved activation controlled region of the polarisation curve as shown in Figure 2.10. The fact that the rate limiting process is potential dependent, suggests that it is related to charge transfer. Considering that the cathode is supplied with pure oxygen, it is not unlikely that the fuel cell response can actually be limited by charge transfer.

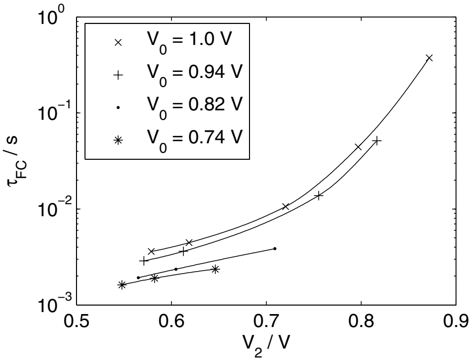

Figure 2.9: Semi-logarithmic plot of the response time of steps a-d in Figure 2.8 as a function of final voltage, V_2, for different initial voltages, V_0.

In Figure 2.10, the response curves for steps from a high external load resistance to four lower resistances are plotted in the V-i diagram, exhibiting the same pattern as predicted in Section 2.3.1 (see Figure 2.3). A deviation from the predicted straight line is observed for the first ms of the step, probably due to switching transients in the transistor and external resistances.

2.4.2 Steps from low to high external load resistance

Also the fuel cell response to a step increase in external load resistance was measured. Figure 2.11 shows the response in cell voltage when changing the external load resistance from a low value up to 200 Ω. This corresponds to the reverse steps of those shown in Figure 2.6. The response is characterised by an ohmic step in cell voltage, followed by a slower increase towards a peak value. After this peak, the cell voltage experiences a gradual decrease, probably as oxides or other surface species form on the cathode (Figure 2.11, inset). Correspondingly, the current density (not shown) exhibits an ohmic

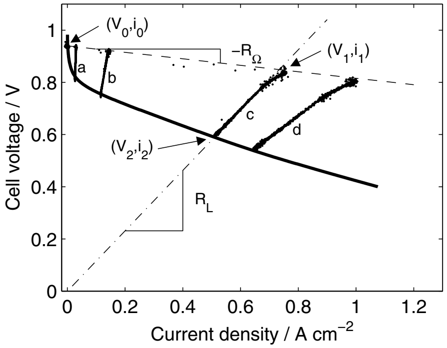

Figure 2.10: Transient response (dots) plotted in the V-i diagram for steps in the external load resistance from 200 Ω to (a) 5.0 Ω, (b) 1.0 Ω, (c) 0.19 Ω and (d) 0.14 Ω. The dashed line has a slope of $-R_\Omega$, while the dash-dotted line has a slope of R_L corresponding to step c. The steady-state polarisation curve is shown as a thick solid line.

drop, before it follows the same increase and decrease as the cell voltage, since current and voltage are related by Ohm's law. The overshoot in cell voltage is more pronounced for steps from lower cell voltages. This can be explained by removal of oxides from the electrodes at low cell voltage giving a higher cell voltage after the step. There are no significant differences in response time; all curves reach the peak value in appr. 5 s and decrease on a time scale of 100 s.

Additional steps from low to high external load resistances were studied and found to exhibit the same trend as described in the previous paragraph. The response time of these steps increased with increasing final voltage, which is in agreement with the trend for steps from high to low external load resistances, where the fuel cell was found to respond slower in regions with high cell voltages. Consequently, a step from high cell voltage to low cell voltage will take shorter time than the reverse step back to high cell voltage. For instance, the response time of a step with initial voltage 0.94 V and final voltage 0.55 V was 3 ms while the reverse step back to 0.94 V had a response time of 35 ms.

The analysis presented in this section is mainly qualitative and does not identify the processes which give rise to the observed trends. An effort to identify rate limiting processes by standard electrochemical methods is presented in the following sections.

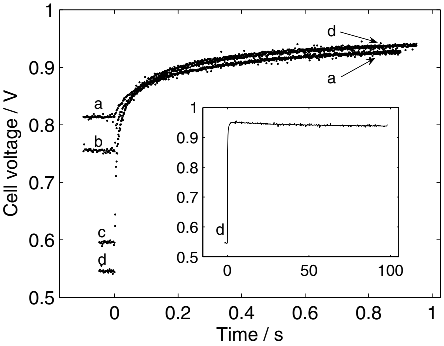

Figure 2.11: The first second of the transient response in cell voltage to a step change in the external load resistance from (a) 5 Ω, (b) 1 Ω, (c) 0.15 Ω and (d) 0.10 Ω to 200 Ω. Inset: First 100 s of response curve (d).

2.4.3 Electrochemical impedance spectroscopy

EIS was applied to separate and quantify the processes governing the fuel cell response. Measured impedance spectra at cell voltages between 0.95 and 0.80 V are shown in Figure 2.12. Two distinct arcs were observed for each spectrum: i) a small potential-independent arc at high frequencies (10 kHz - 120 Hz) and ii) a large potential-dependent arc at lower frequencies (120 Hz - 0.1 Hz). A potential-dependent arc is normally attributed to a charge transfer process [47]. The large arcs in Figure 2.12 are probably related to the charge transfer process at the cathode, since the cathode reaction in a PEMFC is known to have substantially slower kinetics than the anode reaction [48].

As the cell voltage decreased, the large arc attained the shape of a depressed semi-circle. This behaviour can be attributed to the porous structure of the electrode [45]. The inductive impedance observed at frequencies 10-100 kHz is most likely related to cables and electrical connections, and the corresponding data points were disregarded in the fitting process.

The small arc at high frequencies may be attributed to the anodic charge transfer process. The diameter of this arc is appr. 0.1 Ω cm^2 which is comparable to the anode impedance measured for a symmetric H_2/H_2 cell [49]. The arc does not change significantly with cell voltage, which is typically the case for arcs corresponding to rapid charge transfer processes.

For cell voltages 0.85 V and higher, the small high-frequency arc was almost

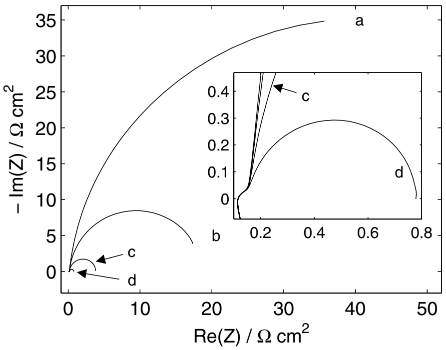

Figure 2.12: Impedance spectra at (a) 0.95 V, (b) 0.90 V, (c) 0.85 V and (d) 0.80 V (hardly visible). Inset: An expanded view of the low impedance region.

negligible compared to the large arc. This caused unprecise fitting of the parameters corresponding to the small arc. Since the shape of this arc did not change significantly for cell voltages 0.80 V and higher, fitting parameters for this arc were kept constant above 0.80 V, using the parameter values found at 0.80 V.

For cell voltages 0.70 V and lower, the large arc still decreased with decreasing cell voltage while the small high-frequency arc remained unchanged as shown in Figure 2.13. In addition, a third arc was observed, emerging at frequencies ranging from 3 Hz for curve e to 11 Hz for curve h. Since there was no clear trend in these arcs, no effort was made to include elements in the equivalent circuit to model this behaviour (ref. Figure 2.5), and the data points corresponding to these arcs were disregarded in the fitting process. However, it is not unlikely that they correspond to the second transient reported in Section 2.4.1. The onset of the second transient occured around 0.1 s, which corresponds to a frequency of 10 Hz. This is in the same range as the frequencies where the third arcs emerged. In addition, the third arc only appeared at cell voltages where also the second transient appeared.

The high-frequency crossing of the real axis decreased slightly for cell voltages decreasing from 0.70 to 0.40 V (Figure 2.13). This can be explained by an increased water production on the cathode at higher currents, giving a more humidified membrane with higher conductance.

The equivalent circuit in Figure 2.5 gave an excellent fit to the impedance data, as can be expected when using CPEs. The cathode parameters are

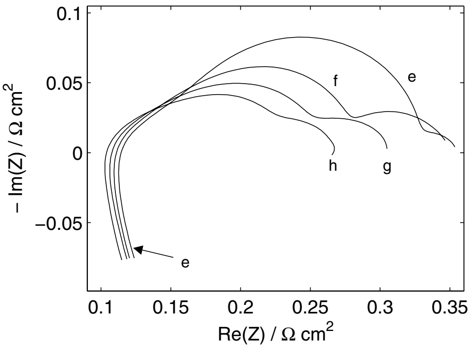

Figure 2.13: Impedance spectra at (e) 0.70 V, (f) 0.60 V, (g) 0.50 V and (h) 0.40 V.

shown in Table 2.1. The increasing cathode arc size at higher cell voltages is reflected in an increasing value for the cathode charge transfer resistance, R_c. The fitted values of ϕ_c are less than 1, which reflects the porous structure of the electrode. For cell voltages below 0.70 V, the value of ϕ_c decreases with decreasing cell voltage. This is reasonable since an increased current density will give even more inhomogeneous conditions throughout the electrode. A fitted value of R_Ω ($0.11 \pm 0.01\ \Omega\ \mathrm{cm}^2$) was in agreement with the value found from step measurements (see Section 2.3.1). The parameter values of R_Ω, R_c and C_c found here have the same order of magnitude as reported in similar studies [44, 50, 51].

The EIS-derived response time, τ_{EC} calculated from Equation 2.4 for each cell voltage is included in Table 2.1. This response time has the same potential dependence and order of magnitude as τ_{FC} calculated in Section 2.4.1. This indicates that the large arc of the impedance spectrum is the frequency domain representation of the potential dependent response observed in Section 2.4.1.

A semilogarithmic plot of IR-corrected cell voltage vs. R_c^{-1} (ref. Figure 2.5) is shown in Figure 2.14. The slope of this curve is identical to the Tafel slope found from steady state polarisation data. This confirms that R_c indeed corresponds to a charge transfer resistance [52].

In summary, results from EIS suggest that the potential dependent response observed in Section 2.4.1 is related to a charge transfer process on the cathode, and that this process limits the fuel cell response at cell voltages above 0.7 V.

Table 2.1: Cathode parameters obtained from fitting of the impedance spectra at different cell voltages.

Cell voltage / V	R_c / Ω cm^2	T_c / F cm^{-2} s$^{\phi-1}$	ϕ_c	C_c / F cm^{-2}	τ_{EC} / s
0.95	77.9	0.0218	0.928	0.0137	1.1
0.90	18.4	0.0203	0.952	0.0150	0.28
0.85	3.67	0.0195	0.970	0.0161	0.059
0.80	0.614	0.0210	0.967	0.0170	0.010
0.70	0.173	0.0266	0.939	0.0177	0.0031
0.60	0.151	0.0401	0.843	0.0132	0.0020
0.50	0.143	0.0650	0.757	0.0111	0.0016
0.40	0.128	0.0947	0.709	0.0111	0.0014

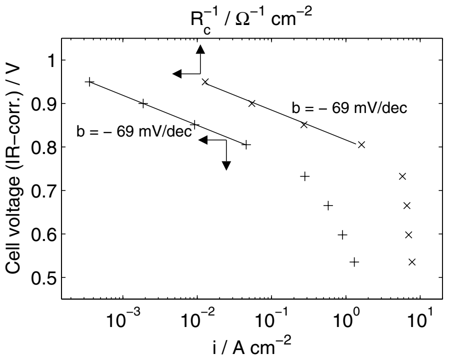

Figure 2.14: Comparison of the Tafel plot generated from the polarisation curve (+) and from R_c^{-1} (x), relating the potential dependent arc to a charge transfer process.

2.4.4 Chronoamperometry

Chronoamperometry was applied to assess the second transient (see Figure 2.7). Step changes in cell voltage from open circuit to lower cell voltages were applied. A second transient in current after a temporarily stable plateau emerged at appr. 0.1 s for steps down to 0.60 V and lower. This is the same behaviour as observed for steps in external load resistance (ref. Figure 2.7). Figure 2.15 shows a plot of current density as a function of the inverse square root of time. These curves form straight lines after appr. 0.15 s, which indicates that the transport of reactants or products occurs by diffusion [53, pg. 163]. Even though Cottrell's equation does not apply to the experimental conditions in this study, the linear relation between current density and $t^{-1/2}$ is taken as an indication that the second transient is caused by a diffusion process. However, the $i(t^{-1/2})$ lines do not extrapolate to zero, which they would for a transport process limited by diffusion only. Probably, another parallel process is contributing to the mass transport.

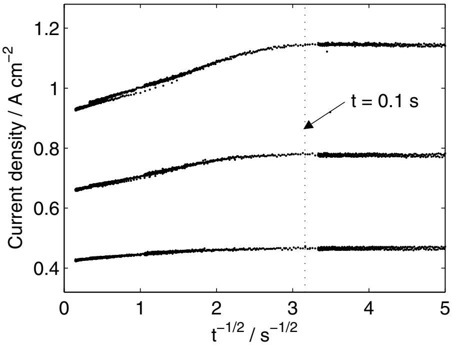

Figure 2.15: Chronoamperometric measurements for potential steps from 0.990 V (close to open circuit potential) down to 0.40 V (upper curve), 0.50 V (middle curve) and 0.60 V (bottom curve). The time window from 40 ms to 45 s is shown.

The presented results do not provide sufficient basis to identify the process giving rise to the observed plateau, but the following explanation is proposed: Oxygen travels to the reaction sites directly from the gas diffusion layer, but also through the polymer phase of the catalyst layer. The diffusion process identified in Figure 2.15 can thus stem from diffusion of oxygen through the polymer phase, while the parallel mass transport process is transport of oxygen directly from the gas diffusion layer. Sufficient oxygen is dissolved in the polymer phase to represent a reservoir which gives a temporarily stable plateau. A rough estimate shows that the amount of oxygen necessary to give the observed plateau is appr. 15% of the total amount that can be dissolved in the membrane [54].

2.5 Conclusion

The transient response of a single PEMFC supplied with pure hydrogen and oxygen was investigated by resistance step measurements assisted by EIS and chronoamperometry. The PEMFC was found to respond quickly and reproducibly to load changes and showed excellent load-following performance.

A characteristic response pattern was identified: For steps to a lower external load resistance, an ohmic drop in cell voltage (and an equivalent ohmic step in current) was followed by a slower transient related to a charge transfer process in the cathode. Since the load was purely resistive, cell voltage and current were related by Ohm's law during the slower transient. The response time of the charge transfer transient depended on cell voltage and decreased with initial and final cell voltages. Response times in the range from 0.38 s to 1.6 ms were observed, depending on the initial and final voltages. The voltage dependence was most pronounced in the activation controlled region of the polarisation curve (0.75 V and higher). For steps with final voltages below appr. 0.65 V, a second relaxation process appeared at about 0.1 s, after a temporarily stable plateau in cell voltage and current. This relaxation process had an apparently constant response time of appr. 2 s, and chronoamperometric measurements related it to a diffusion process, possibly diffusion of oxygen through the polymer phase of the catalyst layer. Transient paths from one steady state on the polarisation curve to another were shown, matching a predicted pattern. This pattern also predicted the overshoot or undershoot in cell voltage and current during the transient.

Acknowledgement

The Research Council of Norway and Aker Kværner Power & Automation Systems AS are kindly acknowledged for financial support.

References

[1] W. He, G. Lin, and T. V. Nguyen, *AIChE J.*, **49**, 3221 (2003).

[2] K. K. Bhatia and C.-Y. Wang, *Electrochim. Acta*, **49**, 2333 (2004).

[3] J. F. Moxley, S. Tulyani, and J. B. Benziger, *Chem. Eng. Science*, **58**, 4705 (2003).

[4] J. Benziger, E. Chia, J. F. Moxley, and I. G. Kevrekidis, *Chem. Eng. Science*, **60**, 1743 (2005).

[5] T. Abe, H. Shima, K. Watanabe, and Y. Ito, *J. Electrochem. Soc.*, **151**, A101 (2004).

[6] Q. Dong, J. Kull, and M. M. Mench, *J. Power Sources*, **139**, 106 (2005).

[7] S. Kim, S. Shimpalee, and J. W. Van Zee, *J. Power Sources*, **135**, 110 (2004).

[8] S. Kim, S. Shimpalee, and J. W. Van Zee, *J. Power Sources*, **137**, 43 (2004).

[9] S. Kim, S. Shimpalee, and J. W. Van Zee, *J. Electrochem. Soc.*, **152**, A1265 (2005).

[10] J. C. Amphlett, E. H. de Oliveira, R. F. Mann, P. R. Roberge, A. Rodrigues, and J. P. Salvador, *J. Power Sources*, **65**, 173 (1997).

[11] S. O. Morner and S. A. Klein, *J. Solar Energy Eng.*, **123**, 225 (2001).

[12] W. Friede, S. Raël, and B. Davat, *IEEE T. Power Electr.*, **19**, 1234 (2004).

[13] J. Hamelin, K. Agbossou, A. Laperrière, F. Laurencelle, and T. K. Bose, *Int. J. Hydrogen Energy*, **26**, 625 (2001).

[14] W. H. Zhu, R. U. Payne, D. R. Cahela, and B. J. Tatarchuk, *J. Power Sources*, **128**, 231 (2004).

[15] J. M. Corrêa, F. A. Farret, and L. N. Canha, in *The 27th Annual Conference of the IEEE Industrial Electronics Society. IECON'01*, vol. 3, pp. 141–146 (2001).

[16] S. Yerramalla, A. Davari, A. Feliachi, and T. Biswas, *J. Power Sources*, **124**, 104 (2003).

[17] L.-Y. Chiu, B. Diong, and R. S. Gemmen, *IEEE T. Ind. Appl.*, **40**, 970 (2004).

[18] R. S. Gemmen, *J. Fluids Eng.*, **125**, 576 (2003).

[19] M. Ceraolo, C. Miulli, and A. Pozio, *J. Power Sources*, **113**, 131 (2003).

[20] X. Xue, J. Tang, A. Smirnova, R. England, and N. Sammes, *J. Power Sources*, **133**, 188 (2004).

[21] P. R. Pathapati, X. Xue, and J. Tang, *Renewable Energy*, **30**, 1 (2005).

[22] S. Um, C. Wang, and K. Chen, *J. Electrochem. Soc.*, **147**, 4485 (2000).

[23] F. Chen, Y. Su, C. Soong, W. Yan, and H. Chu, *J. Electroanal. Chem.*, **566**, 85 (2004).

[24] F. Chen, H.-S. Chu, C.-Y. Soong, and W.-M. Yan, *J. Power Sources*, **140**, 243 (2004).

[25] H. P. L. H. van Bussel, F. G. H. Koene, and R. K. A. M. Mallant, *J. Power Sources*, **71**, 218 (1998).

[26] J. C. Amphlett, R. F. Mann, B. A. Peppley, P. R. Roberge, and A. Rodrigues, *J. Power Sources*, **61**, 183 (1996).

[27] Y. Wang and C.-Y. Wang, *Electrochim. Acta*, **50**, 1307 (2005).

[28] D. Natarajan and T. V. Nguyen, *J. Electrochem. Soc.*, **148**, A1324 (2001).

[29] W.-M. Yan, C.-Y. Soong, F. Chen, and H.-S. Chu, *J. Power Sources*, **143**, 48 (2005).

[30] R. Buxbaum and H. Lei, *J. Power Sources*, **123**, 43 (2003).

[31] B. Emonts, J. B. Hansen, H. Schmidt, T. Grube, B. Höhlein, R. Peters, and A. Tschauder, *J. Power Sources*, **86**, 228 (2005).

[32] M. Sommer, A. Lamm, A. Docter, and D. Agar, *J. Power Sources*, **127**, 313 (2004).

[33] M. J. Khan and M. T. Iqbal, *Renewable Energy*, **30**, 421 (2005).

[34] M. Y. El-Sharkh, A. Rahman, M. S. Alam, P. C. Byrne, A. A. Sakla, and T. Thomas, *J. Power Sources*, **138**, 199 (2004).

[35] M. Y. El-Sharkh, A. Rahman, M. S. Alam, A. A. Sakla, P. C. Byrne, and T. Thomas, *IEEE T. Power Syst.*, **19**, 2022 (2004).

[36] M. De Francesco and E. Arato, *J. Power Sources*, **108**, 41 (2002).

[37] J. T. Pukrushpan, H. Peng, and A. G. Stefanopoulou, in *Proceedings of the International Mechanical Engineering Congress & Exposition 2002, ASME*, pp. 1–12 (2002).

[38] J. T. Pukrushpan, A. G. Stefanopoulou, and H. Peng, in *Proceedings of the American Control Conference 2002*, pp. 3117–3122 (2002).

[39] S. Caux, J. Lachaize, M. Fadel, P. Shott, and L. Nicod, *J. Process Contr.*, **15**, 481 (2005).

[40] R. M. Moore, K. H. Hauer, D. Friedman, J. Cunningham, P. Badrinarayanan, S. Ramaswamy, and A. Eggert, *J. Power Sources*, **141**, 272 (2005).

[41] Y. Zhang, M. Ouyang, Q. Lu, J. Luo, and X. Li, *Appl. Therm. Eng.*, **24**, 501 (2004).

[42] H. Weydahl, S. Møller-Holst, T. Burchardt, and G. Hagen, Dynamic behaviour of an alkaline fuel cell - results from introductory experiments, Poster at 1st European Hydrogen Energy Conference (2003).

[43] F. Zenith, H. Weydahl, I. A. Lervik, T. Burchardt, S. Møller-Holst, S. Skogestad, and G. Hagen, Simulation and experimental study of the transient response of fuel cells, Poster at 9th Ulm Electrochemical Talks (2004).

[44] M. Ciureanu and R. Roberge, *J. Phys. Chem. B*, **105**, 3531 (2001).

[45] R. L. Hurt and J. R. MacDonald, *Solid State Ionics*, **20**, 111 (1986).

[46] A. Lasia, in *Modern Aspects of Electrochemistry*, B. E. Conway, J. O. M. Bockris, and R. E. White, editors, vol. 32, chap. 2, pp. 143–247, Kluwer Academic/Plenum Publishers, New York (1999).

[47] V. A. Paganin, C. L. F. Oliveira, E. A. Ticianelli, T. E. Springer, and E. R. Gonzalez, *Electrochim. Acta*, **43**, 3761 (1998).

[48] J. Larminie and A. Dicks, *Fuel cell systems explained*, John Wiley & Sons, Ltd., Hoboken (2000).

[49] M. Ciureanu and H. Wang, *J. Electrochem. Soc.*, **146**, 4031 (1999).

[50] B. Andreaus, A. J. McEvoy, and G. G. Scherer, *Electrochim. Acta*, **47**, 2223 (2002).

[51] Q. Guo, M. Cayetano, Y. Tsou, E. S. De Castro, and R. E. White, *J. Electrochem. Soc.*, **150**, A1440 (2003).

[52] A. Parthasarathy, B. Davé, S. Srinivasan, A. J. Appleby, and C. R. Martin, *J. Electrochem. Soc.*, **139**, 1634 (1992).

[53] A. J. Bard and L. R. Faulkner, *Electrochemical methods: fundamentals and applications*, John Wiley & Sons, Inc., Hoboken, 2nd ed. (2001).

[54] A. T. Haug and R. E. White, *J. Electrochem. Soc.*, **147**, 980 (2000).

Chapter 3

Effect of gas composition and gas utilisation on the dynamic response of a proton exchange membrane fuel cell

H. Weydahl[a], S. Møller-Holst[b], and B. Børresen[a,c]

[a]Department of Materials Science and Engineering, NTNU, NO-7491 Trondheim, Norway
[b]SINTEF Materials and Chemistry, NO-7465 Trondheim, Norway
[c]Current affiliation: Statoil ASA, NO-7005 Trondheim, Norway

Abstract: The transient response of a proton exchange membrane fuel cell (PEMFC) was measured for various cathode gas compositions and gas utilisations (fraction of supplied reactant gas which is consumed in the fuel cell reaction). For a PEMFC operated on pure hydrogen and oxygen, the cell voltage response to current steps was fast, with response times in the range 0.01-1 s, depending on the applied current. For a PEMFC supplied with air as cathode gas, an additional relaxation process related to oxygen transport caused a slower response (appr. 0.1-2 s depending on the applied current). Response curves up to appr. 0.01 s were apparently unaffected by gas composition and utilisation and were most likely dominated by capacitive discharge of the double layer and reaction with surplus oxygen residing in the cathode. The utilisation of hydrogen had only a minor effect on the response curves, while the utilisation of air severely influenced the transient PEMFC response. Results suggested that air flow rates should be high to obtain rapid PEMFC response.

3.1 Introduction

Fuel cells are electrochemical devices that convert chemical energy directly into electrical energy [1]. The potential of this technology lies within the transportation sector where fuel cells operated on hydrogen and air may replace the conventional internal combustion engine, thus eliminating CO_2 emissions from vehicles and increasing energy efficiency. For successful implementation in the transportation sector, the fuel cell must be able to supply a power demand that varies rapidly with time [2]. The proton exchange membrane fuel cell (PEMFC) is promising for such applications, due to its low operating temperature, high power density and system simplicity.

The power output of the fuel cell can be controlled by a well-designed power conditioning system. Instabilities in fuel cell power due to slow processes such as cell heating and membrane humidification can be controlled by adjusting the current output of the cell. In contrast, faster processes, occurring in the sub-second time range are more difficult to compensate for. Upon rapid changes in power demand, these processes may cause power over- or undershoots which can be harmful to electronic components or cause unfavourable transient behaviour. A thorough understanding of transient processes in the sub-second time range is therefore necessary to establish design criteria for a suitable power conditioning system.

According to published literature on dynamic PEMFC behaviour, gas transport is one of the faster processes that occur in a PEMFC, beside ohmic drop and capacitive discharge. Brett et al. [3] investigated the propagation of oxygen into the gas diffusion layer (GDL) of a PEMFC and reported a response time for this process of appr. 2 s. Dong et al. [4] measured real-time gas composition in the cathode gas channel upon steps in cell voltage. The time resolution of these measurements was, however, too low to reveal the relaxation in detail, but a response time of less than one minute was estimated. Several model studies of mass transport in the PEMFC cathode have been carried out [5–9], reporting response times ranging from 0.1 s to a few seconds.

In a previous study from our group, we assessed the dynamic response of a PEMFC supplied with excess amounts of pure oxygen and hydrogen [10]. PEMFC response under minimal mass transport limitations was limited by a cathodic charge transfer process with a potential dependent response time [10]. In real fuel cell applications, however, air rather than oxygen is most commonly used as cathode gas, and the utilisation of reactant gases (fraction of supplied reactant gas which is consumed in the fuel cell reaction) should be high to keep parasitic power losses low. Kim et al. [11–13] assessed the effects of fuel utilisation on transient PEMFC response with special focus on starved fuel conditions (high utilisation). At stoichiometries 1.0 and 1.2 for hydrogen and air, respectively, the increased current following from a step decrease in cell voltage could only be sustained for a certain amount of time before it decreased to a lower value due to insufficient supply of reactant gases. In real applications, a step increase in power demand must be accompanied by a corresponding step increase in fuel cell power, so gas utilisations in the range near 100% must be avoided. Kim et al. [11] also measured PEMFC response at low utilisation, showing that PEMFC response under these conditions was at least as fast as the electronic load used to control cell voltage during the step. This illustrates the importance of using a fast load and high resolution measurements when studying PEMFC response.

If reactant gases are supplied in excess (low utilisation), gas composition in the gas channels will be fairly uniform. In contrast, at high utilisation of reactant gases, most of the supplied gas is consumed in the fuel cell reaction, giving a highly non-uniform composition along the gas channel and starved conditions near the channel outlet. With this in mind, gas utilisation should be low to ensure stable fuel cell operation and optimal dynamic performance, but this entails a corresponding increase in parasitic power losses. Also, gas flow rates affect the delicate heat and water balance in the fuel cell. These considerations stress the importance of a careful selection of gas flow rates to obtain both high system efficiency and optimal dynamic performance. A detailed characterisation of PEMFC reponse at varying gas utilisations provides criteria for a careful selection of gas flow rates.

The purpose of this paper is to investigate how the oxygen content in the cathode gas and the utilisation of reactant gases affect the transient PEMFC response. This is done by measuring the PEMFC response to current steps at different oxygen contents in the cathode gas and varying utilisations of hydrogen and oxygen. Contrary to Kim et al. [11–13], we focuse on fast transient processes, appearing in a sub-second time range. We therefore apply current steps with low switching times. We also focus on gas utilisations that give sustainable increases in power since this is essential in real applications. Three effects on the transient response are assessed: The effect of current step size at varying cathode gas compositions, the effect of cathode gas composition and the effect of oxygen and hydrogen utilisation. Such measurements provide valuable background data for an optimal selection of gas flow rates as well as design criteria for auxiliary system components and power conditioning units.

3.2 Experimental

3.2.1 Hardware and operating conditions

A membrane electrode assembly (MEA) from W. L. Gore & Associates (PRIMEA® MEA, Cleo Series 58, 18 μm nominal membrane thickness, 0.4 mg cm^{-2} Pt loading on both anode and cathode) was sandwiched between two GDLs from E-TEK (ELAT® carbon only). The geometric electrode area was 6.25 cm^2. The MEA and GDLs were mounted in a fuel cell housing from ElectroChem (EFC05-01SP-REF) with triple serpentine flow fields. Two MEAs from the same batch were used in this study, showing only minor differences in dynamic behaviour.

The cathode was supplied with either pure oxygen (99.5% purity) or prepared mixtures of oxygen and nitrogen (99.999% purity). The oxygen content of the prepared mixtures was 60 and 21% (synthetic air). The anode was supplied with hydrogen (99.999% purity). Flow rates were set by calibrated mass flow controllers from Flow-Teknikk. Flow rates for the anode and cathode gases were chosen according to the wanted experimental conditions. Details are given in the next section.

Anode and cathode gases were humidified in separate sparge bottles. To ensure an equal and even temperature, both the PEMFC and sparge bottles were put in a heating cabinet from Termaks (TS8136). There was a substantial heat generation at high currents, so in order to keep the temperature as stable as possible, the heating cabinet was set to 40 °C unless otherwise stated. The temperature of the cathode hardware was monitored by a thermocouple from Omega®, and the operating temperature was 41.5 ± 1.5 °C during the experiments (46 ± 1 °C for measurements presented in Figure 3.1). We do not expect these temperature variations to affect our results significantly.

3.2.2 Current steps

All measurements were performed on a two-electrode setup (full cell) using an IM6e electrochemical workstation and PP200 add-on module from ZAHNER® elektrik. Current steps from zero to larger currents were programmed using the potentiostat software. Current step measurements on ohmic resistors showed that the potentiostat had a rise time of less than 0.1 ms. To obtain similar initial conditions before each step, the PEMFC was operated at 0.8 A cm^{-2} for at least 1 minute, then the current was turned off and the step routine was started when the open circuit voltage had reached a certain value. The step routine consisted of 30 s at zero current followed by a step to a higher current which was held for another 100 s.

3.3 Results and discussion

3.3.1 Effect of current step size for different catode gas compositions

The effect of current step size on the PEMFC response was studied with both synthetic air and pure oxygen as cathode gases. Current steps from zero to higher currents were applied, and the corresponding response in cell voltage was monitored as shown in Figure 3.1. The ohmic resistance estimated from the ohmic drops (not included in the figure) corresponded to the ohmic resistance of the PEMFC measured by electrochemical impedance spectroscopy. For the PEMFC supplied with oxygen (Figure 3.1, left), cell voltage first decreased quickly, reached a minimum, then increased slightly for a few seconds and then decreased again, very slowly for the remaining duration of the measurement. The final slow decrease could be due to various slow responding processes, such as cathode flooding, and is not assessed further here. Two main trends for increasing final current (increasing step size) was identified for the response curves with pure oxygen: i) The undershoot in cell voltage increased, and ii) the response time decreased. For a step to 0.011 A cm^{-2}, the undershoot was 3 mV, while for a step to 1.5 A cm^{-2} it was 12.5 mV. Measuring response time as the time it takes to reach the minimum cell voltage, the steps to 0.011 and 1.5 A cm^{-2} had response times of 0.8 and 0.016 s, respectively. The potential dependence of the response time for a PEMFC supplied with pure oxygen was addressed previously by our group [10] and found to be related to a charge transfer process on the cathode. We do not have a satisfying explanation for the increase in cell voltage following the initial decrease at this time, but it could be related to fast improvements in local conditions, i.e. increased temperature or humidity near the active sites in the cathode. Net changes in temperature and membrane humidification may take several minutes, but we find it likely that local changes can appear in less than a second. Furthermore, the results of Wilson and Gottesfeld [14] suggest that the active region narrows as current density increases. Thus, for steps to higher current densities, a larger amount of heat and water is released in a smaller volume of the cathode. This may explain why the increase in cell voltage following the initial decrease becomes more pronounced with increasing step size.

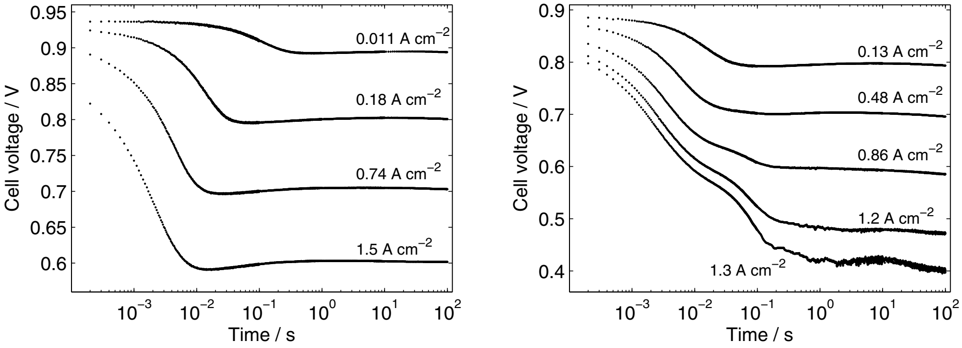

Figure 3.1: Comparison of response to current steps using oxygen (left) and air (right) as cathode gas. Cathode gas flow rate was 150 (left) and 476 Nml/min (right). Anode flow rate was 300 (left) and 200 Nml/min (right). The corresponding utilisation of hydrogen and oxygen was thus less than 25% (left) and 32% (right).

When the cathode was supplied with air (Figure 3.1, right), the response curves are similar in both shape and response time for the initial 0.01-0.1 s. This suggests that the initial response is related to capacitive discharge and reaction with oxygen residing near the active sites. At 0.13 A cm^{-2}, mass transport was not a significant limitation, and the response curves for oxygen and air were similar. For steps to 0.48 A cm^{-2} and higher, mass transport limitations were seen as the onset of a second relaxation process around 0.03 s, causing a further decrease in cell voltage. The exact time where the second relaxation appeared could not be precisely determined from this plot, but a linear plot of cell voltage vs. time (not shown) suggested that the second relaxation appeared earlier for higher current densities. This is reasonable since surplus oxygen is consumed faster and the double layer is discharged faster at higher current densities. Between appr. 0.03 and 0.09 s the cell voltage decreased linearly with time for the three highest current densities. This can be seen as a "shoulder" in the logarithmic plot around 0.05 s (Figure 3.1, right).

The slope of this linear region increased linearly with current density. We are not yet aware of processes that should yield such a linear dependence and can not give a theoretically based explanation for this behaviour at this time.

The linear voltage-time behaviour levelled out and reached a preliminary stable value after appr. 0.2 s for the step to 0.86 A cm^{-2}. For the steps to 1.2 and 1.3 A cm^{-2} this stable value seemed to disappear in a further, more uneven decrease in cell voltage. This could be related to cathode flooding and formation/removal of water droplets from the cathode gas channel. Erratic fluctutations at 1.3 A cm^{-2} indicate severely flooded cathode conditions, and a stable cell voltage at this current density could not be obtained.

In summary, increasing the current step size for a PEMFC supplied with pure oxygen gives a shorter response time due to faster charge transfer at lower cell voltages [10]. For a PEMFC supplied with air, the increased mass transport limitation imposed by nitrogen causes a further decrease in cell voltage and an increased response time.

3.3.2 Effect of cathode gas composition

The response curves with air and oxygen from the previous section can not be directly compared since current values and utilisation rates were not identical for the two data sets. Therefore, another experiment was carried out to study the effect of diluting the oxygen for a chosen current step. The cathode was supplied with O_2/N_2 mixtures with 21, 60 and 100% oxygen, and a current step from 0 to 1.22 A cm^{-2} was carried out for all three cathode gas compositions. To avoid oxygen starvation and large variations in cathode gas composition along the gas channel length, we chose to carry out this experiment at low gas utilisation (29%). In order to keep a constant oxygen utilisation for all compositions, the total flow rate was 476, 167 and 100 Nml/min for 21, 60 and 100% oxygen, respectively. Higher flow rates causes a slightly higher pressure in the gas channel, and this pressure variation may affect our results. However, we expect that this effect is negligible compared to the effect of changing the gas composition.

Figure 3.2 presents the cell voltage response to an identical current step at three cathode gas compositions. Reducing the oxygen partial pressure had a severe impact on the PEMFC response. During the initial response (up to appr. 7 ms) a lower partial pressure of oxygen caused a lower cell voltage value, but otherwise this part of the curve was almost equally shaped for all compositions. This supports our assumption that the initial response is related to discharging of the double layer capacitance and reaction with oxygen already residing in the catalytic layer of the cathode. Effects of mass transport limitiations appeared at appr. 0.04 s for the 60% curve (Figure 3.2, right) and at appr. 0.01 s for the 21% curve. We assume that this time difference is a result of different amounts of oxygen residing in the catalytic layer.

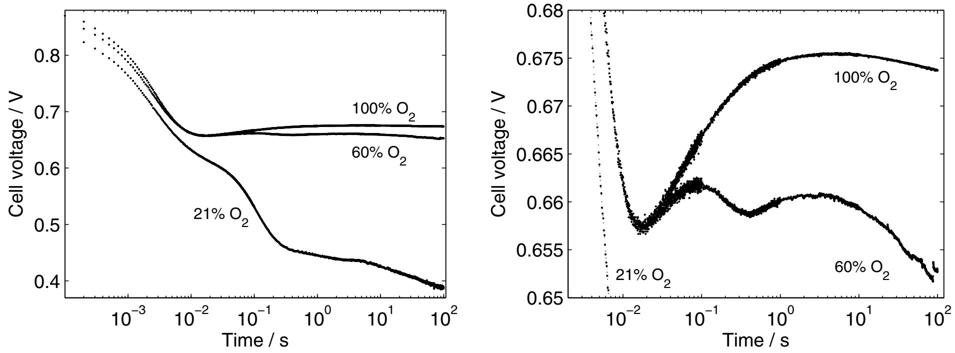

Figure 3.2: Left: Response in cell voltage to a current step from 0 to 1.22 A cm^{-2} for three levels of oxygen content in the cathode gas. Right: Expanded view of response curves for 60 and 100% oxygen. Gas flow rates were adjusted so that the supply rate of oxygen was 100 Nml/min (29% utilisation) for all gas compositions. The flow rate of hydrogen was 200 Nml/min for all compositions.

After reaching a minimum at appr. 0.02 s, the response curve for 100% oxygen increased to a maximum at appr. 4 s. This effect, which could be due to local heat or water production, was commented in the previous section. The oscillations in the response curve for 60% oxygen (Figure 3.2, right) are not yet interpreted nor verified from repeated measurements. The 21% curve decreased linearly with time between appr. 0.02 and 0.1 s, similar to the response curves in Figure 3.1, right. A linear plot (not shown) of the response curve for 21% oxygen showed that cell voltage levelled out at a preliminary stable value at appr. 3 s.

For all compositions, a slow decrease in cell voltage was observed from appr. 10 s. This decrease was more pronounced for lower oxygen concentrations and could be related to cathode flooding. A sudden jump in cell voltage for the 60% curve (Figure 3.2, right) at appr. 90 s indicates that a water plug was removed from the cathode gas channel, exposing a larger electrode area.

In summary, decreasing the amount of oxygen in the cathode gas causes an additional transient to appear at appr. 0.01 s. This transient is probably related to relaxation of oxygen partial pressure in the catalyst and GDL of the cathode and levels out in a few seconds.

3.3.3 Effect of gas utilisation

The third variable studied in this paper is the gas utilisation for both hydrogen and oxygen. The same current step as in the previous section (0 to 1.22 A cm^{-2}) was applied for various flow rates of oxygen or air, giving utilisation rates varying from 30 to 90%.

Figure 3.3 shows the effect on cell voltage response of changing the oxygen utilisation for a fuel cell supplied with pure oxygen. The initial response (up to appr. 10 ms) was independent of utilisation, another indication that discharging of the double layer and reaction with surplus oxygen are dominating the PEMFC response in this time range. From appr. 0.01 s, an increased utilisation caused a shift in cell voltage towards lower values. This can be related to increasingly starved conditions along the cathode gas channel. At 90% utilisation, the voltage response started fluctuating after appr. 1 s, indicating a non-uniform distribution of oxygen along the cathode gas channel.

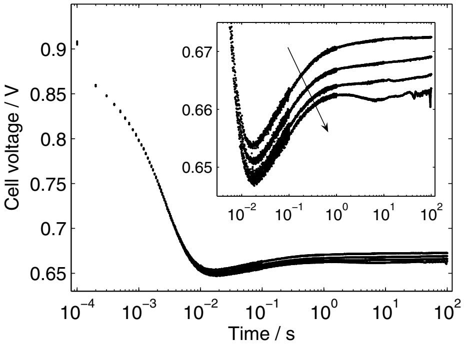

Figure 3.3: Response in cell voltage to a current step from 0 to 1.22 A cm^{-2} for 30, 50, 70 and 90% cathode gas utilisation for a PEMFC supplied with pure oxygen. Inset shows an expanded view of the undershoot. The arrow shows the direction of increasing oxygen utilisation. The flow rate of hydrogen was 200 Nml/min.

The effect of utilisation was also measured for a PEMFC supplied with air instead of oxygen. A smaller current step (0 to 0.80 A cm^{-2}) was imposed for these measurements since 30% utilisation at 1.22 A cm^{-2} required a higher gas flow rate than the mass flow controller could provide. Response curves for different utilisations are shown in Figure 3.4. Increasing the utilisation had a substantial effect on the cell voltage response. Up to appr. 0.06 s the response curves were overlapping as the initial response was dominated by double layer discharge and reaction with surplus oxygen. Effects of utilisation appeared at appr. 0.06 s. A linear plot showed that cell voltage decreased linearly with time from appr. 0.03 s for all utilisations, similar to the response curves in Figures 3.1 and 3.2. An increasing utilisation caused the linear decrease to appear in a wider time range: up to appr. 0.06 s for the 30% curve, 0.1 s for the 50% curve and 0.2 s for the 70% curve. These trends should be further assessed in future studies.

After the linear decrease, the response curves levelled out at appr. 0.3 and 1 s for the 30 and 50% curve, respectively. Thus, an increasing utilisation gave a longer response time. The 70% curve did not reach a stable cell voltage, but decreased for the remaining time of the measurement. This could be due to cathode flooding, since the flow rate and hence also the water removal rate at 70% utilisation were low. The oscillations in cell voltage (Figure 3.4, inset) could be due to the dynamic behaviour of liquid water in the cathode channel. Small oscillations appear when water droplets are formed while the larger voltage dips appear when the droplets coalesce into water plugs which are removed from the cathode gas channel.

Finally, the effect of hydrogen utilisation was investigated. Cell voltage response to identical current steps at varying hydrogen utilisation is shown in Figure 3.5. Measurements were carried out with both pure oxygen and air as cathode gas. Increasing the hydrogen utilisation mainly decreased the cell voltage by a few millivolts, similarly to the effect of an increasing utilisation of pure oxygen (ref. Figure 3.3). The shape of the response curves was otherwise not significantly affected. Compared to the effect of increasing the oxygen utilisation in a PEMFC supplied with air, the effect of hydrogen utilisation was minor. This is an encouraging result, since hydrogen utilisation should be high to obtain high fuel efficiency and low parasitic power losses.

In summary, for a PEMFC supplied with pure gases, an increasing gas utilisation shifts the dynamic cell voltage response to lower values after appr. 0.01 s. For a PEMFC supplied with air, the same effect is seen for an increasing

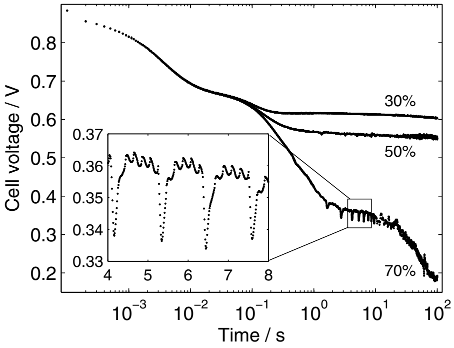

Figure 3.4: Response in cell voltage to a current step from 0 to 0.80 A cm^{-2} for 30, 50 and 70% oxygen utilisation for a PEMFC supplied with synthetic air. Inset shows an expanded view of the voltage dips and oscillations at 70% oxygen utilisation. The flow rate of hydrogen was 200 Nml/min.

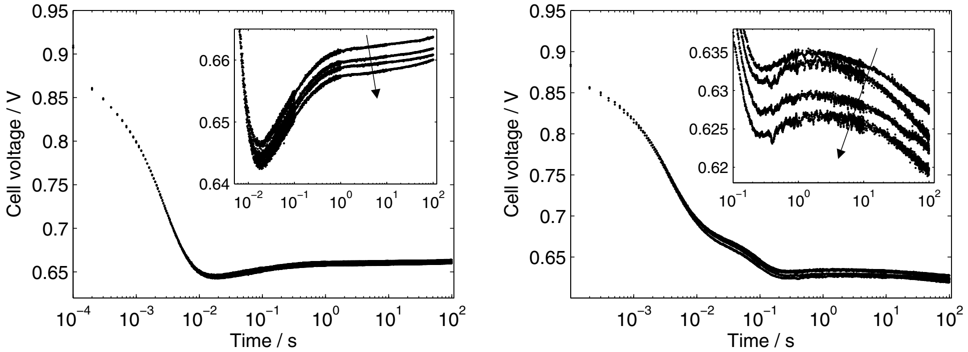

Figure 3.5: Response in cell voltage to a current step for 30, 50, 70 and 90% utilisation of hydrogen. Arrows show the direction of increasing utilisation. Left: PEMFC supplied with 100 Nml/min pure oxygen, current step from 0 to 1.22 A cm^{-2}. Right: PEMFC supplied with 476 Nml/min air, current step from 0 to 0.80 A cm^{-2}. Insets show an expanded view of the response.

hydrogen utilisation, while an increasing oxygen utilisation causes a further decrease in cell voltage and a longer response time.

3.4 Conclusion

We investigated the effect of gas composition and gas utilisation on the dynamic behaviour of a single PEMFC. The transient response in cell voltage to current steps was measured for various cathode gas compositions and utilisations. Results showed that the PEMFC response up to appr. 0.01 s was unaffected by cathode gas composition and utilisation. This suggests that the initial response is determined by capacitive discharge of the charge double layer and reaction with surplus oxygen residing in the cathode. When pure oxygen was used as cathode gas, response curves exhibited a potential dependent response time and undershooting behaviour before reaching a preliminary steady state. When using air as cathode gas instead of pure oxygen, a second relaxation process appeared after the initial response. This process was characterised by a linearly decreasing cell voltage and caused a slower response compared to the PEMFC response with pure oxygen as cathode gas.

Increasing the oxygen utilisation for the PEMFC supplied with air had a major impact on the transient PEMFC response. This showed that oxygen utilisation should be kept low to obtain homogeneous conditions along the cathode channel and a fast response to current steps, but this consideration must be balanced against the increased parasitic power loss at high flow rates. Increasing hydrogen utilisation did not affect the characteristic shape of the response curves and only resulted in a shift in cell voltage towards slightly lower values. The same effect was observed for an increasing oxygen utilisation when the PEMFC was supplied with pure oxygen.

Acknowledgement

The Research Council of Norway and Aker Kværner Power & Automation Systems AS are kindly acknowledged for financial support.

References

[1] J. Larminie and A. Dicks, *Fuel cell systems explained*, John Wiley & Sons, Ltd., Hoboken (2000).

[2] R. K. Ahluwalia and X. Wang, *J. Power Sources*, **139**, 152 (2005).

[3] D. J. L. Brett, S. Atkins, N. P. Brandon, V. Vesovic, N. Vasileiadis, and A. R. Kucernak, *Electrochem. Comm.*, **3**, 628 (2001).

[4] Q. Dong, J. Kull, and M. M. Mench, *J. Power Sources*, **139**, 106 (2005).

[5] W.-M. Yan, C.-Y. Soong, F. Chen, and H.-S. Chu, *J. Power Sources*, **143**, 48 (2005).

[6] Y. Wang and C.-Y. Wang, *Electrochim. Acta*, **50**, 1307 (2005).

[7] Y. Shan and S.-Y. Choe, *J. Power Sources*, **145**, 30 (2005).

[8] D. Natarajan and T. V. Nguyen, *J. Electrochem. Soc.*, **148**, A1324 (2001).

[9] J. M. Stockie, K. Promislow, and B. R. Wetton, *Int. J. Numer. Meth. Fluids*, **41**, 577 (2003).

[10] H. Weydahl, S. Møller-Holst, G. Hagen, and B. Børresen, *J. Electrochem. Soc.*, submitted December 2005.

[11] S. Kim, S. Shimpalee, and J. W. Van Zee, *J. Power Sources*, **135**, 110 (2004).

[12] S. Kim, S. Shimpalee, and J. W. Van Zee, *J. Power Sources*, **137**, 43 (2004).

[13] S. Kim, S. Shimpalee, and J. W. Van Zee, *J. Electrochem. Soc.*, **152**, A1265 (2005).

[14] M. S. Wilson and S. Gottesfeld, *J. Appl. Electrochem.*, **22**, 1 (1992).

Chapter 4

Response of a proton exchange membrane fuel cell to a sinusoidal current load

H. Weydahl[a], S. Møller-Holst[b], and B. Børresen[a,c]

[a]Department of Materials Science and Engineering, NTNU, NO-7491 Trondheim, Norway
[b]SINTEF Materials and Chemistry, NO-7465 Trondheim, Norway
[c]Current affiliation: Statoil ASA, NO-7005 Trondheim, Norway

Abstract: The load-following capability of a single proton exchange membrane fuel cell (PEMFC) was studied by measuring the cell voltage response to a sinusoidal current load with large amplitudes. Effects on the cell voltage response when varying the DC value, amplitude and frequency of the current load were recorded. The load-following capability of the PEMFC was excellent in the operating range where changes in cell voltage were dominated by ohmic losses. No hysteresis in the cell voltage response was observed in this range for frequencies up to 1-10 Hz. In the operating range where changes in cell voltage were dominated by activation losses, hysteresis appeared at lower frequencies (>0.1 Hz) due to sluggish response in the voltage range near open circuit voltage. The increased mass transport limitation imposed when supplying the PEMFC with air caused hysteresis to appear at lower frequencies than for oxygen (above 0.1 Hz, compared to 1-10 Hz for oxygen).

4.1 Introduction

Among the various fuel cell technologies, the proton exchange membrane fuel cell (PEMFC) is considered the most promising replacement of conventional combustion engines [1]. For commercial success in automotive vehicles and other applications with rapidly varying power demands, the load-following capability of the PEMFC is essential [2]. In fuel cell systems for dynamic power demands, energy buffers such as batteries and capacitors are often added to avoid deviations between required and supplied power. However, if the PEMFC is sufficiently fast to follow also a time-varying load, such components may become redundant, giving a cheaper and more compact energy system.

The ability of a PEMFC to follow a varying power demand is determined by how fast each process in the PEMFC responds to a load change. The initial response is determined by the ohmic drop, which is instantaneous, and capacitive discharge of the double layer. An increased power output also causes a higher consumption rate of reactant gases in the catalyst layer. This causes a redistribution of reactant gases in the catalyst layers, gas diffusion layers (GDLs) and gas channels of the PEMFC, taking place on a time scale of a few seconds [3–6]. A higher power output also gives a higher production rate of water in the cathode. Gaseous water represents a diffusion barrier for oxygen, and liquid water may cover active sites in the catalyst layer and block gas transport [3, 7]. Liquid water also affects the water balance of the membrane, giving variations in membrane conductivity on a time scale of seconds to several minutes [6, 8–12]. Changes in cell temperature take place on a time scale of minutes [13–15], but rapid local temperature increases may occur. Dynamic changes on a time scale of seconds and slower can be handled by a well-designed PEMFC controller ensuring stable power output even though cell performance varies. Faster changes in the power output, such as those due to ohmic drop, capacitive discharge and redistribution of reactant gases, can not be controlled in the same manner. These processes must therefore be characterised so that design criteria for a suitable buffer system can be determined.

The load-following capability of PEMFCs has been addressed in a few papers. Jones et al. [16] and Hottinen et al. [17] evaluated the ability of a PEMFC to sustain current pulses appearing in portable electronics, but did not report high-resolution measurements of the rapid cell voltage response. Ziegler et al. modelled the response in PEMFC current to slow voltage sweeps at constant sweep rate [18]. Hysteresis in current was attributed to water accumulation in the cathode GDL. Hamelin et al. [19] and Amphlett et al. [20] measured the cell voltage response of PEMFC stacks to a step in current. These studies demonstrated the initial rapid response of PEMFCs. However, thorough experimental investigations of the ability of PEMFCs to follow a given load profile have to our best knowledge not been reported.

According to Fourier series theory, any periodic function can be represented by a sum of sine and cosine functions with different frequencies and amplitudes. The ability of fuel cells to follow any periodic load profile can therefore be tested by measuring the fuel cell response to a sinusoidal load with varying DC value, frequency and amplitude. Measured fuel cell response to the various sinusoidal loads can then be combined by Fourier analysis to construct the fuel cell response to a given load profile. This method has to our best knowledge not yet been applied to study dynamic fuel cell behaviour. It is different from the well-known electrochemical impedance spectroscopy (EIS) technique where a sinusoidal perturbation with *small* amplitude is applied [21]. By using a small amplitude, linear theory can be applied to analyse response data. This way, the EIS technique separates and quantifies processes with different response times at the chosen steady-state operating point. However, it does not capture how these processes change during the transition from one steady-state operating point to another. By using a *large* amplitude perturbation, the fuel cell response to finite load changes is captured, but linear theory can no longer be applied to analyse response data. Still, this technique can provide qualitative information on the load-following capability of the fuel cell.

In this study, we apply a large-amplitude sinusoidal current load to a single PEMFC and measure the cell voltage response for varying DC values, amplitudes and frequencies of the input current. This way, the load-following capability in the full operating range of the PEMFC is mapped. Current was chosen as the controlled variable since a forced rapid increase in cell voltage may lead to reversal of the current [22]. The intention of this study is to determine how fast changes the PEMFC can follow, at which frequency transient and steady-state response deviate, the characteristic shape of the deviation and its relation to physical processes. In order to address the effect of mass transport on the transient response, measurements were carried out using both oxygen and air as cathode gases. EIS was also applied to measure the transient response around steady-state operating points, providing qualitative data for interpretation of large-amplitude measurements.

4.2 Experimental

4.2.1 Hardware and operating conditions

A membrane electrode assembly (MEA) from W. L. Gore & Associates (PRIMEA® MEA, Cleo Series 58, membrane thickness 18 μm, 0.4 mg cm^{-2} Pt on both anode and cathode) was sandwiched between two GDLs from E-TEK (ELAT® carbon only). The geometric electrode area was 6.25 cm^2. The MEA and GDLs were mounted in a fuel cell housing from ElectroChem (EFC05-01SP-REF) with triple serpentine flow channels.

The anode was supplied with a constant gas flow of hydrogen (99.999% purity) and the cathode with oxygen (99.5% purity) or synthetic air (99.999% purity). To avoid any effects of fuel starvation, both gases were supplied in excess so that consumption never exceeded 20%. The gases were humidified in separate sparge bottles. To ensure an equal and even temperature, both the PEMFC and sparge bottles were placed in a heating cabinet from Termaks (TS8136) with temperature 45 °C. The temperature of the cathode hardware was monitored by a thermocouple from Omega®, and the operating temperature was 46 ± 3 °C during oxygen sinus experiments, 44 ± 1 °C during air sinus experiments, 47 ± 5 °C during EIS with oxygen and 50 ± 5 °C during EIS with air. These temperature variations were assumed not to affect our results significantly.

4.2.2 Sinusoidal current load

A sinusoidal current load was realised using a Wenking STP 84 Standard Potentiostat from Bank Elektronik. This potentiostat is designed for potentiostatic operation only, but by controlling the voltage across a shunt resistor, galvanostatic operation was obtained. A 0.47 Ω, 50 W power resistor from ARCOL (HS200 R47) was used as shunt resistor. It was verified that the resistance of the power resistor was constant throughout the measured current range.

The circuit diagram of the experimental set-up is shown in Figure 4.1. A 15 MHz synthesised function generator from Yokogawa (FG300) produced the sinusoidal control signal for the potentiostat. Separate tests verified that the potentiostat was able to produce sinusoidal currents in the applied range. The technical capacity of the potentiostat limited the peak value and frequency of the applied current to 5.5 A and 1 kHz, respectively.

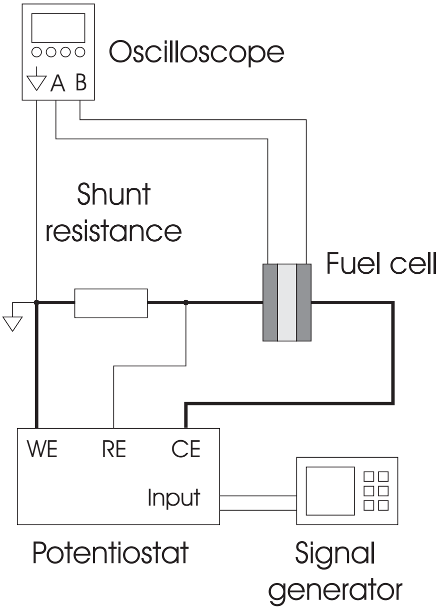

Figure 4.1: Circuit diagram for the sinus measurements.

A digital oscilloscope from Pico® Technology Ltd. (ADC-212) monitored the fuel cell voltage and the voltage across the shunt resistor. The relation between shunt resistor voltage and current was found by comparing oscilloscope data with current readouts from the potentiostat. The shunt resistor was connected directly to the fuel cell cathode end plate using a thick bronze connector, ensuring minimal resistance between shunt resistor and fuel cell cathode.

The PEMFC was allowed to settle for at least two time periods at each frequency before the voltage response was measured, ensuring that the "steady-state" periodic response was established.

4.2.3 Electrochemical measurements

EIS was performed on a two-electrode setup (full cell) using an IM6e electrochemical workstation and PP200 add-on module from ZAHNER® elektrik. An AC signal with amplitude 5 mV and a frequency range from 100 kHz to 100 mHz was applied. The impedance was measured at various steady-state cell voltages to see how the impedance response changed with cell voltage.

The cell voltage was allowed to settle for at least one minute at each potential before the impedance spectrum was recorded. Polarisation curves were obtained with the ZAHNER® equipment using a sweep rate of 1 mV/s.

4.3 Theory and data analysis

A sinusoidal current load has three independent variables: DC value, amplitude and frequency. The effect of changing these variables can be traced in the DC value, amplitude, shape and phase shift of the cell voltage response. As a background for the analysis of our results, we derive the response of a simple equivalent circuit subject to a sinusoidal current load. The equivalent circuit consists of an ohmic resistance, R_{Ω}, in series with a parallel combination of a capacitance, C_{dl}, and a resistance, R_{ct}. The purpose of introducing this circuit is not to reproduce the sinus response of a real PEMFC, but to illustrate the effects of two basic features of a PEMFC cathode: The ohmic resistance of the membrane and fuel cell hardware and a one-step charge transfer reaction without diffusion or adsorption. The impedance response of this circuit is well known and gives a semi-circle in the Nyquist diagram [23, pg. 386].

The analytical expression for the response of this circuit to a sinusoidal current load with a non-zero DC component is straightforward to derive. Simple circuit analysis shows that for a sinusoidal current load

$$I = I_{DC} + I_{AC}\sin(\omega t) \tag{4.1}$$

where I_{DC}, I_{AC} and ω are the DC offset, half amplitude and angular frequency of the sinusoidal current load, respectively, the response of the voltage across the circuit is

$$V_{EC} = (R_{\Omega} + R_{ct})I_{DC} + \frac{I_{AC}R_{ct}\omega\tau}{\sin\gamma(1+(\omega\tau)^2)}\ \sin(\omega t - \gamma) \tag{4.2}$$

where $\tau = R_{ct}C_{dl}$ and

$$\gamma = \arctan\left(\frac{R_{ct}\omega\tau}{R_{ct} + R_{\Omega}(1+(\omega\tau)^2)}\right) \tag{4.3}$$

The voltage response also contains an exponential component which is significant during a specified time interval after the current load is applied. This component has been neglected here, since the measured voltage response was recorded after this part had died out.

As ω increases from 0 towards ∞, the amplitude of V_{EC} decreases from $2I_{AC}(R_{ct}+R_{\omega})$ to $2I_{AC}R_{\Omega}$ since the capacitor acts as a short circuit at high frequencies. The phase shift approaches 0 for $\omega \rightarrow \infty$ and $\omega \rightarrow 0$ and has a maximum at the frequency

$$\omega_{\gamma_{max}} = (1/\tau)\sqrt{(R_{ct}+R_{\Omega})/R_{\Omega}} \tag{4.4}$$

with value

$$\gamma_{max} = \arctan(R_{ct}/(2\sqrt{R_{\Omega}(R_{ct}+R_{\Omega})})) \tag{4.5}$$

In a real fuel cell, the charge transfer resistance and possibly also the double layer capacitance change with cell voltage. Figure 4.2 shows the influence of R_{ct} on the phase shift for chosen values of R_{Ω} and C_{dl}. The phase shift increases with increasing values of R_{ct}, but this difference becomes insignificant at high frequencies.

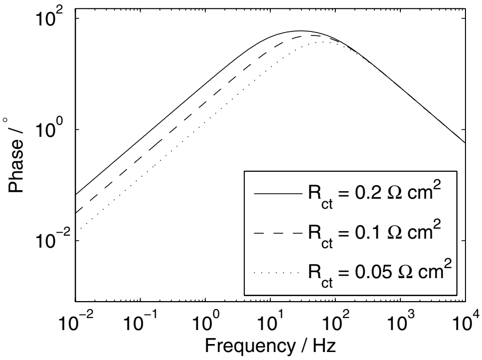

Figure 4.2: The phase shift of the voltage across an R_{Ω}-$R_{ct}||C_{dl}$ equivalent circuit (Equation (4.2)) for different values of R_{ct}. The values of R_{Ω} and C_{dl} for these calculations were 0.1 Ω cm^2 and 0.1 F cm^{-2}, respectively.

From experimental data the phase shift of the PEMFC response was found by measuring the time difference between the occurrence of a current maximum/minimum and cell voltage minimum/maximum. The phase shift at current maximum and minimum will be different since PEMFC properties vary with cell voltage.

4.4 Results and discussion

4.4.1 Electrochemical measurements

Steady-state polarisation curves were obtained shortly before and/or after measurements with sinusoidal current. Minor variation in performance was observed, corresponding to ± appr. 5% of the total ohmic resistance of the PEMFC. There was, however, no clear trend in these variations, so they could just as well be related to variations in membrane water content or degree of flooding as to the fluctuating load. Further experiments should be carried out to assess the long-term effects of a fluctuating load on PEMFC performance.

EIS was applied to obtain indications on which processes dominated the cell response at varying cell voltages and oxygen content of the cathode reactant gas. Impedance spectra for the PEMFC supplied with oxygen and air are shown in Figure 4.3. The potential dependent arc size of the oxygen spectra is believed to reflect the potential dependent cathode charge transfer reaction. This dependence was most pronounced near open circuit voltage, as expected for a charge transfer reaction. We conclude that capacitive discharge and electrochemical reaction dominate the fuel cell response when the cathode is supplied with oxygen.

The impedance spectra showed a different trend when the PEMFC was supplied with synthetic air instead of oxygen (Figure 4.3, right). The spectrum at 0.8 V resembled that of oxygen, but at 0.7 V, a second arc emerged at low frequency. The size of this arc increased with decreasing cell voltage, completely dominating the impedance spectra for cell voltages lower than 0.7 V. Since the same PEMFC was used for both oxygen and air measurements, we believe this second arc to stem from the increased mass transport limitation imposed by using air as cathode gas instead of pure oxygen. This limitation became more and more pronounced with increasing current (decreasing cell voltage). At 0.5 and 0.4 V, the current response to the AC perturbation was unstable and not shaped like a sinus curve, so the theoretical basis for impedance calculations was no longer valid. We conclude that mass transport limitations dominated the PEMFC response from appr. 0.5 V and lower for operation with air.

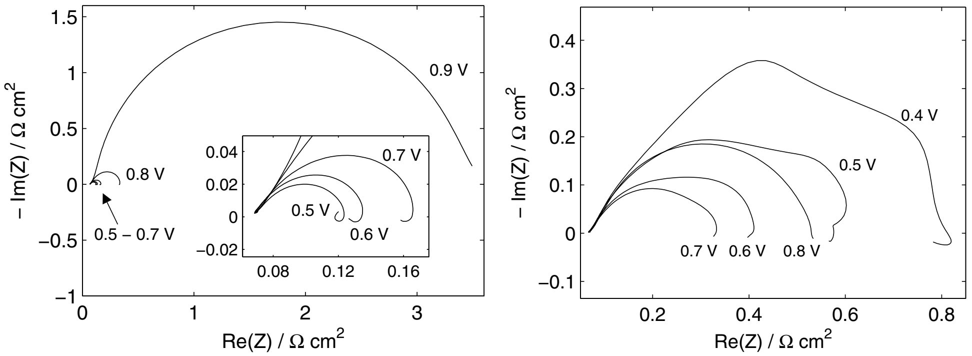

Figure 4.3: Impedance response at various cell voltages for the same PEMFC supplied with oxygen (left) and synthetic air (right). Inset in left figure shows an expanded view of the arcs at low cell voltages.

4.4.2 Response of PEMFC supplied with oxygen

A sinusoidal current load was applied to a PEMFC supplied with pure oxygen and hydrogen. Figure 4.4 shows the cell voltage response to a sinusoidal current with constant DC value and amplitude and varying frequency. Three effects of increasing the frequency can be seen: i) the amplitude of the cell voltage response decreased, ii) the shape of the response curve changed and iii) the phase shift first increased and then decreased. These effects illustrate different aspects of the load-following capabilities of the PEMFC and are discussed in closer detail below.

i) *Effect of frequency on cell voltage amplitude.* As the frequency increased, the amplitude of the cell voltage response decreased. In Figure 4.5, the maximum and minimum values of the voltage response are plotted as a function of frequency. This plot shows that the maximum voltage continuosly decreased with increasing frequency. This behaviour is related to the slow response of the PEMFC at higher cell voltages, an effect which was reported previously by our group [22]. At high cell voltages, in the non-linear region of the polarisation curve, changes in cell voltage with current density is mainly caused by activation losses [24]. These losses stem from the resistance towards electrochemical reaction and also from changes on the electrode surfaces (i.e., oxide coverage). After a change in current, these processes re-establish a new steady-state cell voltage in a certain amount of time. At a certain frequency these processes can

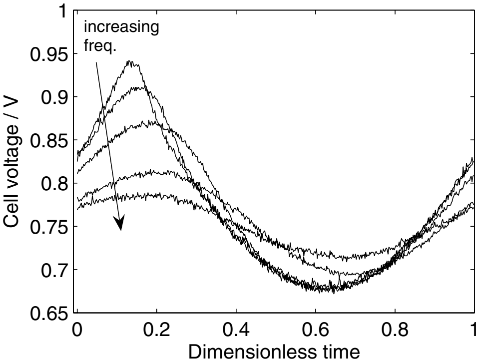

Figure 4.4: Comparison of cell voltage response to a sinusoidal current load (DC value 0.41 A cm^{-2}, amplitude 0.81 A cm^{-2}) with frequencies 0.1 Hz - 1 kHz for a PEMFC operated on pure hydrogen and oxygen. One wave length of the response is shown on a dimensionless time scale, t/T, where T is the time period of the current load ($T = 1/f = 2\pi/\omega$).

no longer keep up with the changes in current, and the maximum cell voltage decreases. As seen in Figure 4.5, this frequency was between 0.1 and 1 Hz, which corresponds to a relaxation time of 1-10 s. This is in agreement with our previous experience with PEMFC response times at high cell voltages [22].

At low cell voltages, where the polarisation curve is nearly linear, changes in cell voltage with current density are mainly due to ohmic losses within the PEMFC [24]. Ohmic losses respond instantaneously to changes in current, so the minimum cell voltage remained unaffected by frequency up to 10 Hz (Figure 4.5). However, for frequencies larger than 10 Hz, the double layer capacitance of the PEMFC caused a decreasing impedance with frequency, thus decreasing the ohmic losses in the PEMFC as an increasing part of the AC current was consumed by the double layer capacitance. A frequency of 10-100 Hz corresponds to a relaxation time of 10-100 ms, which is in agreement with reported PEMFC response times in this voltage range [22].

ii) *Effect of frequency on shape of response curve.* As seen in Figure 4.4, not only the amplitude, but also the shape of the voltage response changed with frequency. For low frequencies the voltage response had a sharp peak, while at high frequencies, it was shaped like a regular sine wave. The sharp peak

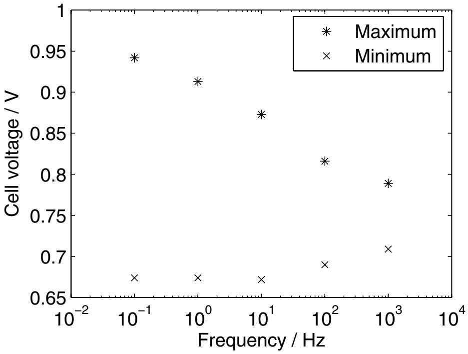

Figure 4.5: Frequency dependence of maximum and minimum values of the cell voltage response in Figure 4.4 (PEMFC operated on pure hydrogen and oxygen, sinusoidal current load with DC value of 0.41 A cm^{-2} and amplitude 0.81 A cm^{-2}).

at low frequencies is a result of the non-linear relation between cell voltage and current density for cell voltages higher than appr. 0.85 V. As frequency increased, the sharp peak changed into a regular sine wave since cell voltage could not keep up with the changes in current, giving a nearly linear relation between cell voltage and current density. The trough of the voltage response was shaped like a regular sine wave for all frequencies (see Figure 4.4) due to the nearly linear relation between cell voltage and current density for cell voltages lower than appr. 0.75 V.

iii) *Effect of frequency on cell voltage phase shift.* Frequency also affected the phase shift of the cell voltage response. Due to the large amplitude of the current load, phase shift was different at the maxima and minima of the cell voltage response. Phase shifts were calculated as described in the Theory section and plotted in Figure 4.6. The phase shift at both maxima and minima increased with frequency and reached a maximum between 10 and 1000 Hz. This behaviour is due to the capacitance of the fuel cell electrodes. As seen in Figure 4.2, the phase shift of an R-R||C circuit exhibits the same trend, even though this circuit is too simple to reproduce the PEMFC response to acceptable precision. Equation (4.3) indicates that the phase shift increases with increasing charge transfer resistance, R_{ct}, but that this effect is less pronounced at high frequencies (ref. Figure 4.2). This trend is the same as seen in Figure 4.6. Since charge transfer resistance was higher at higher cell voltages, the phase shift value at the cell voltage maximum was larger than that at cell voltage minimum. On logarithmic axes, the difference between the two is less pronounced at high frequencies, similar to the theoretical phase shifts in Figure 4.2. At 1 Hz, the calculated phase shift of the cell voltage minima was negative. This shows that there is a substantial uncertainty in the phase shift calculations.

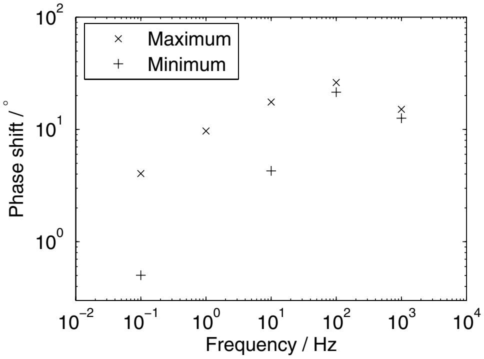

Figure 4.6: Phase shift at maximum and minimum values of the cell voltage response in Figure 4.4 (PEMFC operated on pure hydrogen and oxygen, sinusoidal current load with DC value of 0.41 A cm^{-2} and amplitude 0.81 A cm^{-2}).

The effect of frequency on the amplitude, shape and phase shift of the voltage response can be further visualised by plotting voltage response in the V-i diagram along with the steady-state polarisation curve. Figure 4.7 shows the steady-state and sinusoidal response at various frequencies for the PEMFC operated on pure oxygen. At 0.1 Hz, the sinusoidal response resembled the steady-state performance at current densities less than appr. 0.2 A cm^{-2}, but was somewhat lower than the polarisation curve at higher current densities. This is a rather surprising result since we would rather expect oxygen partial pressure and hence also cell voltage to be higher when the current increases fast than at steady state. We have not yet found a proper explanation for this offset, but it may be a result of experimental artifacts since different measuring equipment was used to record steady-state polarisation curves and sinus response (see Experimental). However, this small deviation did not influence the observed trend and corresponding conclusion.

Cell voltage hysteresis appeared at frequencies above 0.1 Hz at low current densities (< 0.2 A cm^{-2}) and at frequencies above 10 Hz at 0.8 A cm^{-2}. This shows that the load-following capability of the PEMFC is better in an operating range where ohmic losses dominate the changes in cell voltage. At 1 kHz, hysteresis was less pronounced and the response approached the shape of a straight line with a smaller slope than the linear region of the steady-state polarisation curve. This can be related to the capacitive behaviour of the PEMFC (ref. Theory and data analysis). At high frequency, most of the imposed current is absorbed (supplied) by the charge double layer of the PEMFC electrodes, reducing voltage losses related to mass transport and electrochemical reaction. The slope of the straight line at high frequency is therefore determined by the ohmic resistance of the PEMFC. At 1 kHz, this slope was 0.087 ± 0.002 Ω cm^{-2}.

Measurements were repeated with different DC values and amplitudes of the sinusoidal current. Changing the DC value and amplitude of the current load mainly changed the range of the cell voltage response. Otherwise, the same trends as discussed above were observed.

4.4.3 Response of PEMFC supplied with air

Measurements were repeated using synthetic air as cathode gas instead of pure oxygen. Replacing oxygen with air reduced the open circuit voltage due to a lower partial pressure of oxygen and increased the slope of the linear region of the steady-state polarisation curve. Since the same current load was used, cell voltage scanned a wider range when air was used as cathode gas.

Figure 4.8 shows the cell voltage response in the V-i diagram along with the steady-state polarisation curve. The main difference from the cell response with oxygen is that cell voltage hysteresis at high current densities appeared at lower frequencies. For the PEMFC supplied with air, hysteresis appeared at frequencies above 0.1 Hz, vs. 10 Hz for the PEMFC supplied with pure oxygen. In light of the impedance response (ref. Figure 4.3, right) we assume that this difference is caused by an increased mass transport limitation in the cathode. As shown in Figure 4.2, an increased resistance towards reaction causes phase shift to appear at lower frequencies. Phase shift in the frequency domain appears as hysteresis in the V-i diagram. Thus, the increased resistance towards reaction in a PEMFC supplied with air instead of oxygen causes hysteresis to appear at lower frequencies.

At 1 kHz, the voltage response approached the shape of a straight line with

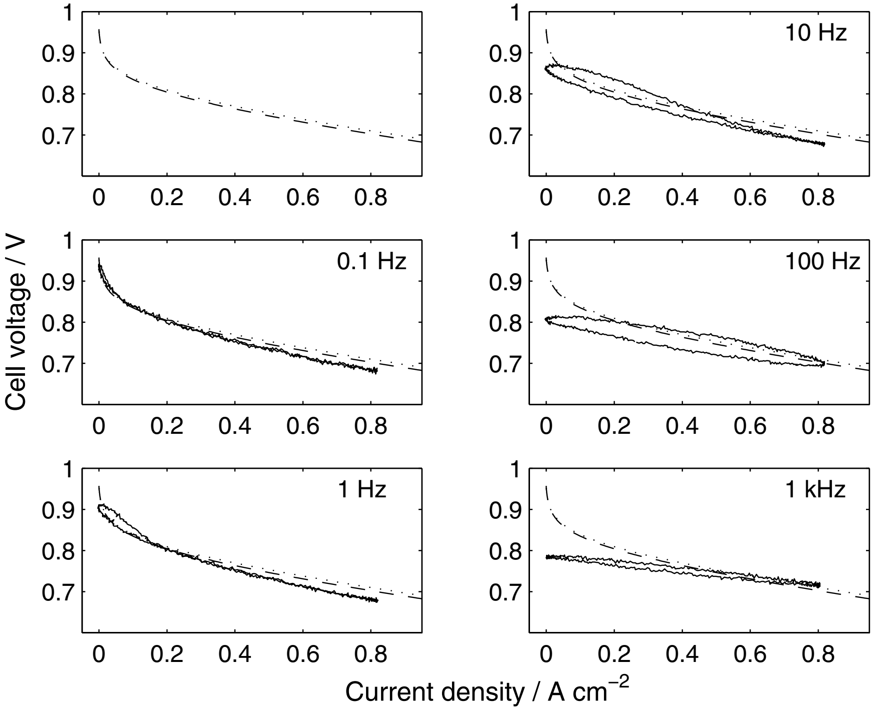

Figure 4.7: The cell voltage response of Figure 4.4 (PEMFC operated on pure hydrogen and oxygen, sinusoidal current load with DC value of 0.41 A cm^{-2} and amplitude 0.81 A cm^{-2}) plotted in the V-i diagram along with the steady-state polarisation curve. Upper left figure shows only the polarisation curves obtained at a sweep rate of 1 mV/s before (dotted line) and after (dashed line) the sinus load measurements. Time increases clockwise around the cell voltage loops.

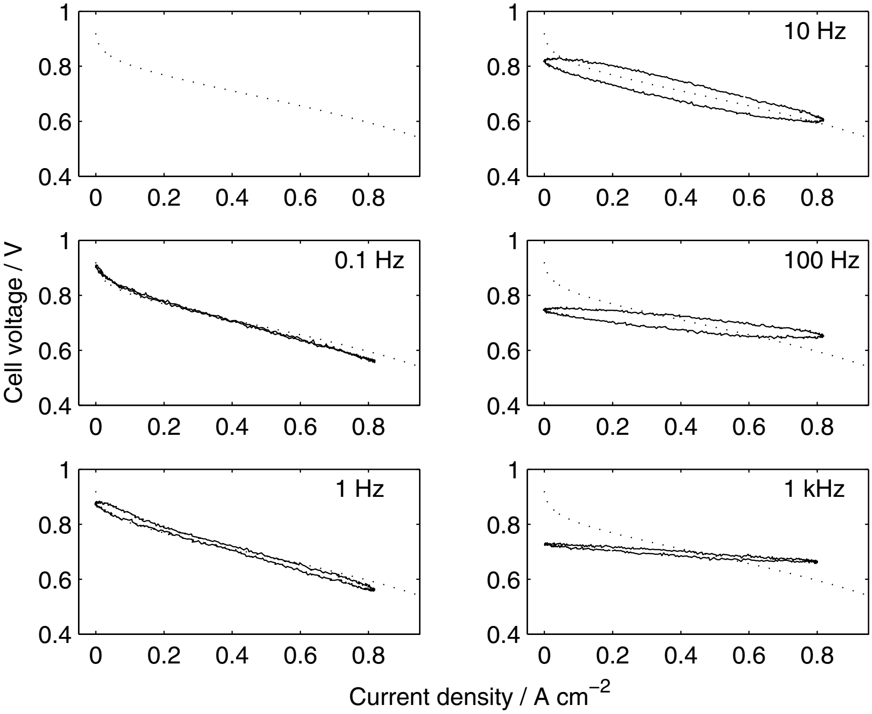

Figure 4.8: The cell voltage response to a sinusoidal current (DC value 0.41 A cm^{-2}, amplitude 0.81 A cm^{-2}) for a PEMFC operated on pure hydrogen and synthetic air plotted in the V-i diagram along with the steady-state polarisation curve (dashed line). Upper left figure shows only the polarisation curve obtained at a sweep rate of 1 mV/s before the sinus load measurements. Time increases clockwise around the cell voltage loops.

a slope corresponding to an ohmic resistance of $0.079 \pm 0.002\ \Omega\ \mathrm{cm}^2$. This is somewhat smaller than the resistance obtained for measurements with oxygen ($0.087 \pm 0.002\ \Omega\ \mathrm{cm}^2$). We expect that this difference is caused by improved humidification and higher membrane conductivity during measurements with air.

4.5 Conclusion

The load-following capability of a single PEMFC was studied by measuring the cell voltage response to a sinusoidal current load with large amplitude. By varying the frequency, DC value and amplitude of the current load and recording the resulting cell voltage response, qualitative information on the response to any periodic load profile can be extracted. The PEMFC was supplied with both oxygen and synthetic air to assess the effect of an increased oxygen transport limitation on the load-following capability.

For the PEMFC supplied with pure oxygen, the cell voltage response followed the steady-state polarisation curve for frequencies below 0.1 Hz. At higher frequencies, hysteresis in the cell voltage appeared, meaning, cell voltage was higher at increasing current than at decreasing current. Hysteresis appeared at 0.1 Hz in the activation region of the polarisation curve and at 10-100 Hz in the ohmic region of the polarisation curve. Thus, the load-following capability of the PEMFC was significantly better at low cell voltages than at cell voltages near open circuit. This difference can be explained by the higher resistance to charge transfer at high cell voltages, giving a more sluggish response. At frequencies above 100 Hz, the AC component of the current was absorbed by the charge double layer. Thus, the relation between cell voltage and current was linear at high frequencies, determined by the ohmic resistance of the fuel cell. This behaviour gave an overshoot in cell voltage compared to steady state for currents larger than the DC component of the sinusoidal current.

For the PEMFC supplied with air, the increased oxygen transport limitation caused hysteresis at low cell voltages to appear at lower frequencies than for the PEMFC supplied with oxygen. Otherwise, the features of the response were similar to those observed for a PEMFC operated on pure hydrogen and oxygen.

This study showed that the load-following capability of PEMFCs is promising. The long-term effects of a fluctuating load on the overall PEMFC performance should be further investigated.

Acknowledgement

The Research Council of Norway and Aker Kværner Power & Automation Systems AS are kindly acknowledged for financial support.

References

[1] J. T. Pukrushpan, H. Peng, and A. G. Stefanopoulou, *J. Dyn. Syst. - T. ASME*, **126**, 14 (2004).

[2] R. K. Ahluwalia and X. Wang, *J. Power Sources*, **139**, 152 (2005).

[3] D. Natarajan and T. V. Nguyen, *J. Electrochem. Soc.*, **148**, A1324 (2001).

[4] D. J. L. Brett, S. Atkins, N. P. Brandon, V. Vesovic, N. Vasileiadis, and A. R. Kucernak, *Electrochem. Comm.*, **3**, 628 (2001).

[5] J. M. Stockie, K. Promislow, and B. R. Wetton, *Int. J. Numer. Meth. Fluids*, **41**, 577 (2003).

[6] Y. Wang and C.-Y. Wang, *Electrochim. Acta*, **50**, 1307 (2005).

[7] W. He, G. Lin, and T. V. Nguyen, *AIChE J.*, **49**, 3221 (2003).

[8] T. Okada, G. Xie, and Y. Tanabe, *J. Electroanal. Chem.*, **413**, 49 (1996).

[9] W. Friede, S. Raël, and B. Davat, *IEEE T. Power Electr.*, **19**, 1234 (2004).

[10] E.-S. J. Chia, J. B. Benziger, and I. G. Kevrekidis, *AIChE J.*, **50**, 2320 (2004).

[11] F. Chen, Y. Su, C. Soong, W. Yan, and H. Chu, *J. Electroanal. Chem.*, **566**, 85 (2004).

[12] F. Chen, H.-S. Chu, C.-Y. Soong, and W.-M. Yan, *J. Power Sources*, **140**, 243 (2004).

[13] J. C. Amphlett, R. F. Mann, B. A. Peppley, P. R. Roberge, and A. Rodrigues, *J. Power Sources*, **61**, 183 (1996).

[14] Y. Shan and S.-Y. Choe, *J. Power Sources*, **145**, 30 (2005).

[15] P. R. Pathapati, X. Xue, and J. Tang, *Renewable Energy*, **30**, 1 (2005).

[16] P. B. Jones, J. B. Lakeman, G. O. Mepsted, and J. M. Moore, *J. Power Sources*, **80**, 242 (1999).

[17] T. Hottinen, M. Mikkola, and P. Lund, *J. Power Sources*, **129**, 68 (2004).

[18] C. Ziegler, H. M. Yu, and J. O. Sundmacher, *J. Electrochem. Soc.*, **152**, A1555 (2005).

[19] J. Hamelin, K. Agbossou, A. Laperrière, F. Laurencelle, and T. K. Bose, *Int. J. Hydrogen Energy*, **26**, 625 (2001).

[20] J. C. Amphlett, E. H. de Oliveira, R. F. Mann, P. R. Roberge, A. Rodrigues, and J. P. Salvador, *J. Power Sources*, **65**, 173 (1997).

[21] A. Lasia, in *Modern Aspects of Electrochemistry*, B. E. Conway, J. O. M. Bockris, and R. E. White, editors, vol. 32, chap. 2, pp. 143–247, Kluwer Academic/Plenum Publishers, New York (1999).

[22] H. Weydahl, S. Møller-Holst, G. Hagen, and B. Børresen, *J. Electrochem. Soc.*, submitted December 2005.

[23] A. J. Bard and L. R. Faulkner, *Electrochemical methods: fundamentals and applications*, John Wiley & Sons, Inc., Hoboken, 2nd ed. (2001).

[24] J. Larminie and A. Dicks, *Fuel cell systems explained*, John Wiley & Sons, Ltd., Hoboken (2000).

Chapter 5

Fundamental studies of the transient response of an alkaline fuel cell

H. Weydahl[a], I. A. Lervik[a], A. M. Svensson[b], T. Burchardt[b,c],
S. Møller-Holst[b], G. Hagen[a†], and B. Børresen[a,d]

[a]Department of Materials Science and Engineering, NTNU, NO-7491 Trondheim, Norway
[b]SINTEF Materials and Chemistry, NO-7465 Trondheim, Norway
[c]Current affiliation: Revolt Technology AS, NO-7034 Trondheim, Norway
[d]Current affiliation: Statoil ASA, NO-7005 Trondheim, Norway

Abstract: The dynamic behaviour of an alkaline fuel cell (AFC) supplied with pure oxygen and hydrogen was investigated by load step measurements assisted by electrochemical impedance spectroscopy (EIS). Load step measurements were carried out using an in-house designed resistance board which gave step changes in a purely resistive load. Resistive load steps between various operating points along the polarisation curve were carried out and the corresponding transient response in cell voltage and current was measured. The transient cell response consisted of an initial ohmic drop followed by a relaxation towards the new steady state. The observed response was slower at higher cell voltages. Measured response times varied on a time scale of appr. 10 ms to 10 s, depending on the initial and final voltages. Results from EIS

[†] This paper is dedicated to the late Prof. Georg Hagen who contributed significantly to this work before his passing October 2004.

measurements suggested that the potential dependent response time stemmed from the charge transfer reaction at the cathode. Transient response curves were plotted in the V-i diagram and shown to follow a pattern determined by the load resistance and ohmic resistance of the AFC. Results showed that when supplied with pure oxygen and hydrogen, the AFC responded sufficiently fast for automotive applications.

5.1 Introduction

Fuel cell technology is expected to be implemented in a broad range of applications. For real market penetration, fuel cells will have to comply with the load requirements of these applications. For applications where the load changes rapidly, the dynamic behaviour of the fuel cell is critical. Knowledge of the load variation requirements as well as the response time of the cell at load change is essential for identifying the need for and design of a buffer system.

Alkaline fuel cells (AFCs) are considered a promising fuel cell technology due to low-cost catalysts, high reliability and low activation overvoltage [1]. In the 1960s and 70s, AFCs were chosen as power generators for the Apollo program and the Orbiter space shuttles [2] and have also been proved feasible for automotive applications [3–5]. AFC technology was recently reviewed by Gouerec et al. [6] and McLean et al. [1] who pointed out the advantages and potential of this technology.

Previous studies of AFCs have focused on reaction mechanisms [7], electrocatalysis [8,9], electrode wetting mechanisms [9–11], degradation [12–15], CO_2 tolerance [16] and electrode preparation and performance optimisation [17–20]. Different aspects of dynamic fuel cell behaviour have been studied for most types of fuel cells (see e.g., [21–24]), but to our best knowledge, no such studies have been reported for the AFC technology. Transient measurement techniques have been applied to AFC electrodes, mainly to measure steady-state parameters such as diffusion constants and kinetic parameters. Gultekin et al. [25] applied an exponential decay current method to measure the capacitance and exchange current density of porous gas-diffusion electrodes, but did not report the transient response in electrode potential. Another transient technique, electrochemical impedance spectroscopy (EIS), has been applied successfully to investigate the oxygen reduction reaction on porous electrodes in an alkaline environment [26–28]. These studies show that oxygen diffusion and charge transfer processes with two- or four-electron pathways dominate the impedance response.

In this paper, we investigate the dynamic behaviour of an AFC, addressing how fast the AFC reaches a new steady state after a load change, the characteristic shape of the response curves and the physical origin of the transient response. Our motivation is to determine if AFCs are feasible for applications with a rapidly varying power demand. For instance, in automotive applications a response time less than 1 s is necessary [29]. If the AFC is not sufficiently fast to provide sufficient power in due time, buffer components such as capacitors and batteries are necessary to cover the power deficiency. A characterisation of dynamic AFC behaviour is of relevance for the development of control strategies and provides design criteria for the buffer system and power conditioning system. Our group recently carried out a similar study of a proton exchange membrane fuel cell (PEMFC) [30]. For this study, a passive load with short switching time was developed to measure the autonomous response of the PEMFC. A passive load was preferred since external control loops in an active load might influence the initial fuel cell response. In order to observe how fast the PEMFC was able to respond to load changes, reactant gases were supplied in excess and pure oxygen was used as cathode gas instead of air. This way, transient effects due to gas shortage were reduced, showing the PEMFC response under minor mass transport limitations. Under these conditions, the PEMFC response was limited by the cathode charge transfer reaction, which gave a potential dependent response time ranging from milliseconds to seconds [30]. In this paper, we use a similar approach to investigate the transient response of an AFC under minor mass transport limitations, recording cell voltage and current upon step changes in the load. In addition, EIS is applied to identify physical processes giving rise to the observed response. Since measurements were carried out under minimal mass transport limitations, reported results indicate the fastest response that can be obtained for an AFC.

5.2 Experimental

5.2.1 Hardware and operating conditions

The investigated AFC consisted of two 20 cm^2 porous gas diffusion electrodes (prepared by SINTEF) separated by an 8 mm thick electrolyte layer of 6.0 M KOH contained in a Plexi glass fuel cell housing, sketched in Figure 5.1. The electrode catalyst was platinum on carbon which was mixed with Teflon and rolled onto a nickel mesh. The electrodes were supplied with a constant gas flow of 150 Nml/min hydrogen (99.999%) and 75 Nml/min oxygen (99.5%). Reactant gases were supplied into separate gas compartments without flow fields, as shown in Figure 5.1. The electrolyte temperature was kept constant at 26 ± 1 °C by circulating electrolyte from a reservoir at room temperature.

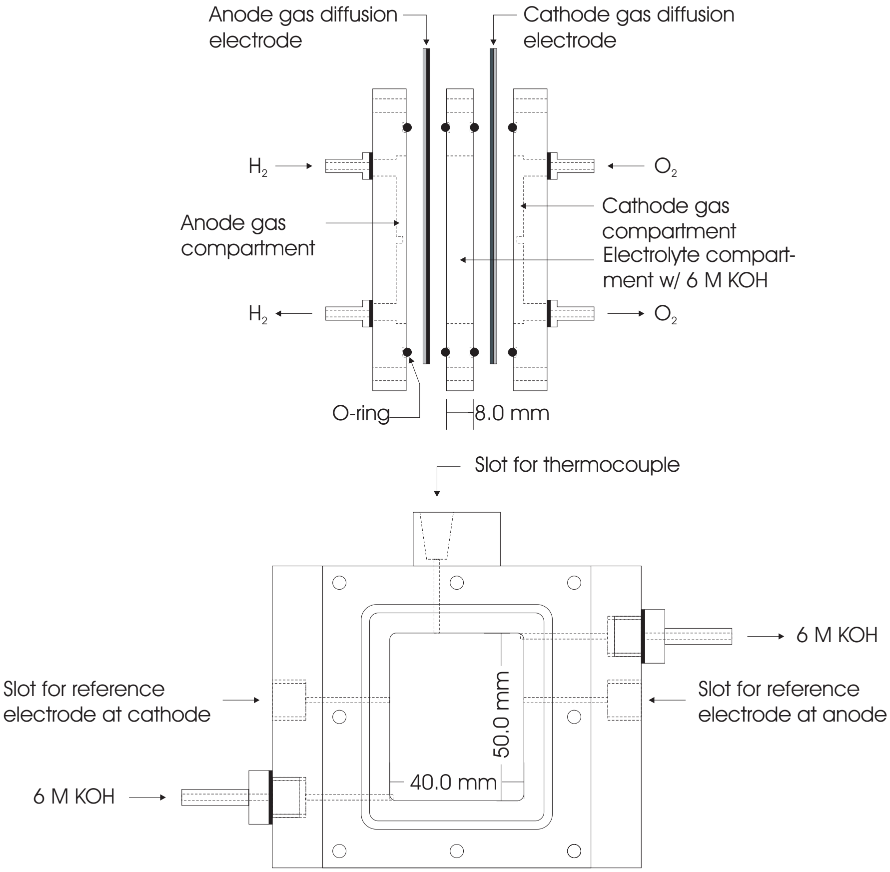

Figure 5.1: Plexi glass fuel cell housing, exploded profile (top) and front view (bottom). Electrical contacts were directly connected to the electrode material.

In-house built reference electrodes (Hg/HgO references in 6.0 M KOH) were used to monitor the electrode potentials. Two reference electrodes, one for each electrode, were mounted to the fuel cell housing via separate salt bridges symmetrically situated 1 mm from their respective electrodes (ref.

Figure 5.1). The stability of the reference electrodes was verified by measuring the potential difference between the two references when no current was running through the AFC. A constant potential difference of 1.7 mV indicated that stable reference potentials were obtained for both reference electrodes.

5.2.2 Step changes in the external load resistance

A circuit diagram of the experimental set-up is shown in Figure 5.2. The AFC was connected to an in-house designed resistance board consisting of two metal film resistors, R_1 and R_2, in parallel, where the branch containing R_2 was connected or disconnected using an IRF1404 MOSFET. This set-up is equivalent to that described in Ref. [30]. R_1 and R_2 constitute the external load resistance, R_L. When R_2 is disconnected, $R_L = R_1$, and when R_2 is connected, $R_L = R_1R_2/(R_1+R_2)$. The transistor was switched on or off within 30 μs, giving a step change in the external load resistance. The resistances of R_1 and R_2 were selected with a switch knob so that various external load resistances could be realised.

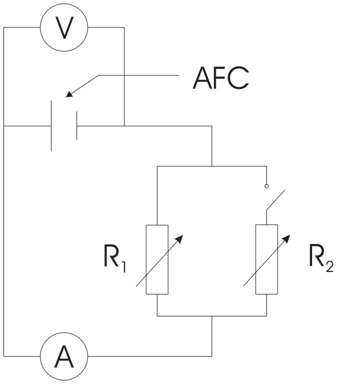

Figure 5.2: Circuit diagram for the resistance step measurements. Resistors R_1 and R_2 constitute the total external load resistance, R_L. The switch in the R_2 branch is an IRF1404 MOSFET.

Cell voltage and current during the load step were measured with an ADC-212 oscilloscope from Pico Technology Ltd. The current was measured with a Tektronix A6302 current probe connected to the oscilloscope via a Tektronix TM502A current probe amplifier.

5.2.3 Electrochemical measurements

The cathode impedance was measured by EIS carried out on a half cell set-up (using the anode as counter electrode) over a frequency range from 100 kHz to 100 mHz using an IM6e electrochemical workstation and PP200 add-on module from ZAHNER® elektrik. The cathode impedance was measured at four cathode potentials, corresponding to cell voltages of 0.9, 0.8, 0.7 and 0.6 V. A complex non-linear least-squares fitting program, LEVM version 7.0, was used to fit the parameters of an equivalent circuit to the measured impedance.

EIS was also applied to measure the ohmic resistance of the electrodes. The ohmic resistance of the electrodes was found where the electrode impedance spectrum crossed the real axis in the Nyquist diagram at high frequencies.The corresponding reference electrode on each side of the cell was used for these measurements. The total ohmic resistance of the cell was measured on a two-electrode set-up, using the cathode as working electrode and the anode as reference and counter electrode. Thus, the ohmic resistance of the electrolyte layer could be calculated by subtracting the anode and cathode resistance from the total cell resistance.

Polarisation curves for the AFC were obtained using the ZAHNER® equipment on a two-electrode set-up. Cell voltage and current was measured during voltage sweeps from open circuit voltage to 0.1 V with a sweep rate of 1 mV/s. This sweep rate was not low enough to represent a true steady-state, but gave an indication of quasi steady-state performance.

5.3 Theory and analysis methods

The same theoretical treatment as in Ref. [30] was applied in this study. Definitions and necessary notation are repeated here.

A typical response pattern for cell voltage and current upon a step decrease in the external load resistance is sketched in Figure 5.3. An initial ohmic drop in cell voltage from the initial voltage, V_0, to V_1 is followed by a slower decay towards the new steady state cell voltage, V_2. Correspondingly, the current jumps from an initial value, I_0, to I_1 and settles at a final current, I_2. The size of the ohmic drop is determined by the ohmic resistance of the AFC, thus $|V_0 - V_1|/|I_0 - I_1|$ is constant for all steps when the cell resistance is constant. During the slower decay, cell voltage and current are related by Ohm's law, since the external load, R_L, is purely resistive. Thus $V(t)/I(t) = R_L$ holds during the slower decay.

The response time of the fuel cell was measured in terms of τ_{FC}, defined implicitly by

$$\frac{V_\tau - V_2}{V_1 - V_2} = \frac{1}{e}, \tag{5.1}$$

where $V_\tau = V(t = \tau_{FC})$ and e is Euler's number. We use the fraction $1/e$ when determining τ_{FC}, so that τ_{FC} corresponds to the time constant of exponential decay, even though the measured response was not purely exponential.

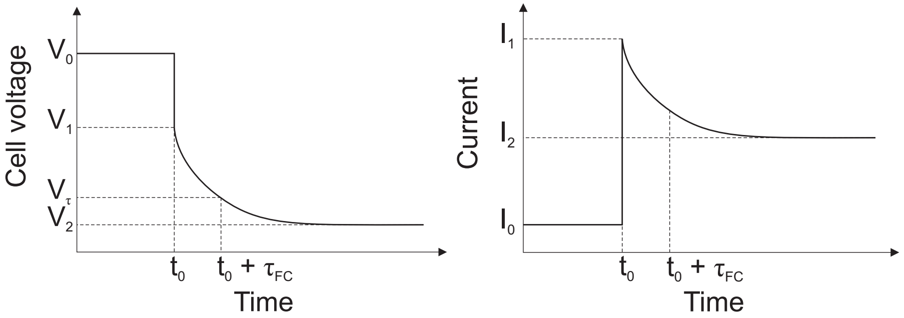

Figure 5.3: A sketch of the transient response curves in cell voltage and current upon a step change from high to low external load resistance.

The cathode impedance spectra were analysed using the equivalent circuit shown in Figure 5.4, previously reported by i.e., Ciureanu et al. [31]. R_Ω models the uncompensated ohmic resistance between the reference and the working electrode, while the parallel combination of R_c and CPE$_c$ models the cathode charge transfer process. A constant phase element (CPE) is used instead of a capacitance to reflect frequency dispersion due to the porous structure of the electrode [32].

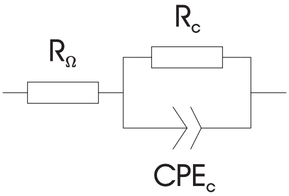

Figure 5.4: Equivalent circuit for the cathode [31]. R_Ω is the uncompensated resistance between the reference and the working electrode. R_c and CPE$_c$ are the cathode charge transfer resistance and CPE, respectively.

The impedance and equivalent capacitance of a constant phase element (CPE) are given as [33]

$$Z_{\mathrm{CPE}} = \frac{1}{T(i\omega)^{\phi}}, \tag{5.2}$$

and

$$C_{\mathrm{CPE}} = \left[T(R_{\Omega}^{-1} + R_c^{-1})^{\phi-1}\right]^{1/\phi}, \tag{5.3}$$

respectively, where T and ϕ are the CPE parameters. As a measure of the response time of the equivalent circuit, we use $\tau_{EC} = R_c C_{\mathrm{CPE}}$, which is the theoretical time constant of a parallel combination of a resistance and capacitance.

5.4 Results and discussion

5.4.1 Steady-state performance

Prior to load step measurements, the steady-state performance of the AFC was measured. Figure 5.5 shows the steady-state polarisation curve of the AFC, exhibiting a limited performance. At 0.3 V the cell only produced 0.1 A cm^{-2}. In comparison, Gouerec et al. [6] report 0.8 V at 0.1 A cm^{-2} for a cathode supplied with air at 70 °C. Impedance measurements revealed a total ohmic cell resistance of $3.42 \pm 0.05\ \Omega\ \mathrm{cm}^2$, where 41% was attributed to the cathode, 48% to the anode and 11% to the electrolyte. The high ohmic resistance was thus not mainly caused by the electrolyte layer between the electrodes, but rather by high contact resistance within the electrodes. This may indicate that the Teflon content of the catalyst layers was too high. However, the IR-corrected cell voltage was only 0.6 V at 0.15 A cm^{-2} (Figure 5.5), showing that also the electrochemical activity of the electrodes was rather low. This may also be related to a high content of Teflon, covering catalyst particles and reducing the active surface area. At the present state, we do not have sufficient experimental basis to determine what caused the low steady state performance. Since the focus of this study is the *dynamic* performance of AFCs, this issue will not be further addressed here. Even though the steady state performance is low, we expect that the trends in dynamic response are representative for AFCs in general.

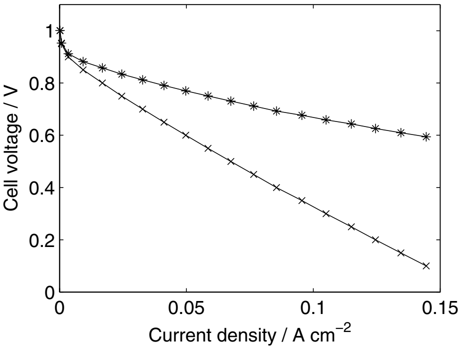

Figure 5.5: Steady-state polarisation curve of the AFC; total cell voltage measured between cathode and anode (x) and IR-corrected cell voltage (*).

5.4.2 Load step measurements

Load step measurements were carried out to measure the response time of the AFC and also reveal the characteristic shape of the response curves. Figure 5.6 shows the response in cell voltage and current density to step decreases in the external load resistance, from 470 Ω to lower values. A step decrease in load resistance gives an increase in the power output of the cell. The corresponding initial cell voltage for these steps was 1.03 V, appr. 0.04 V below the open circuit voltage. The observed cell voltage response exhibited an instantaneous ohmic drop followed by a relaxation towards a new steady state. The relaxation showed a simple overshoot behaviour and was clearly potential dependent: The AFC reached steady-state within appr. 50 s for the smallest step (final voltage 0.97 V) and within appr. 30 ms for the largest step (final voltage 0.35 V). Similar potential dependence was observed by our group for a PEMFC [30], but the PEMFC response was faster than observed here for an AFC. This can be related to the fact that the PEMFC produced higher current densities than the AFC at equivalent cell voltages, giving faster changes in local conditions in the active layer. However, since the AFC and PEMFC systems are significantly different in composition and structure, results from each system can not be directly compared.

Figure 5.6 demonstrated the effect of decreasing the final cell voltage, V_2, while keeping the initial cell voltage, V_0, constant. Additional steps were carried out, starting out from lower initial cell voltages, V_0. The characteristics

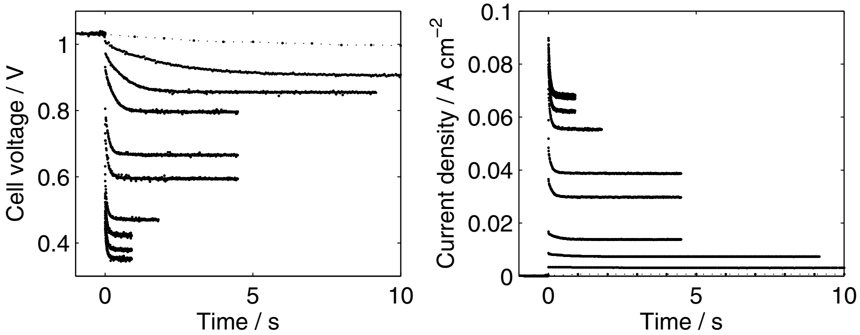

Figure 5.6: Transient response in cell voltage (left) and current density (right) to a change in the external load resistance, R_L, from 470 Ω to lower resistance values. High cell voltage corresponds to high load resistance while high cell current corresponds to low load resistance. The fastest response curves were only measured up to 1 s.

of the response curves were the same, exhibiting an ohmic drop in cell voltage followed by a relaxation towards a new steady state. Figure 5.7 shows the response time calculated from Equation 5.1 for various steps from high to low external load resistance and illustrates the potential dependence of the response time. Two trends were observed: i) The response time of the AFC decreased with decreasing final cell voltage, V_2, for steps with the same initial cell voltage, V_0. ii) For steps to the same final voltage, V_2, the response time decreased with decreasing initial voltage V_0. Since the AFC response was faster at lower cell voltages, the response time was primarily determined by the final cell voltage and secondarily by the size of the step. These are the same trends as previously reported by our group for a PEMFC [30]. We note that in the voltage range typical for practical applications (0.5-0.8 V), the AFC response time was less than 1 s, which is sufficient for automotive applications [29]. However, when the AFC is supplied with air instead of pure oxygen, a slower response due to mass transport limitations can be expected.

As shown previously by our group [34], response curves can be plotted in the V-i diagram together with the polarisation curve to show the overshoot in current density and cell voltage upon a step decrease in the external load resistance. Figure 5.8 shows this plot for the steps in Figure 5.6. The ohmic

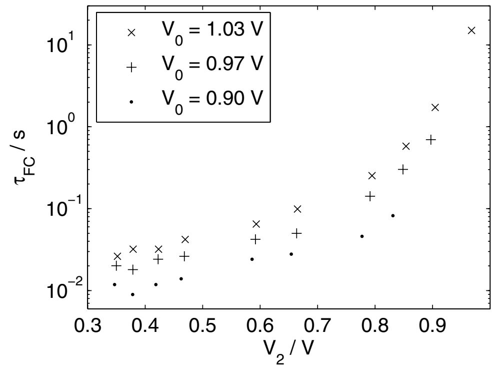

Figure 5.7: Semi-logarithmic plot of the response time of various load steps as a function of final cell voltage, V_2, for different initial voltages V_0.

and non-ohmic part of the steps can be clearly distinguished in this plot. As interpreted by Zenith et al. [35], the immediate ohmic step follows a straight line from the initial state (V_0, i_0) to (V_1, i_1) (Figure 5.8, left). The slope of this line is $-R_\Omega$ since $(V_1 - V_0)/(I_1 - I_0) = -R_\Omega$. From (V_1, i_1) to (V_2, i_2) the transient response follows a straight line with slope R_L since cell voltage and current are related by Ohm's law. Thus, the overshoot in cell voltage and current is determined by the values of R_Ω and R_L after the step. Note that the external load resistance seems to increase slightly for the first 0.5 ms (seen by a deviation between the transient response curve and the R_L-line). The reason for this behaviour has not been identified, but can probably be related to switching transients in the transistor or instability in the resistors used in the resistance board.

To investigate the response to a step *increase* in the external load resistance, the reverse steps (back to a high value of R_L) were measured. Figure 5.9 shows the reverse steps of those presented in Figure 5.6. These steps exhibited an initial ohmic step in cell voltage (and a corresponding step decrease in current) followed by a slow increase towards steady-state. Since the AFC responds slower at higher cell voltages, the response time was now dependent on the final voltage only. Thus, no significant difference in response time could be seen for the steps in Figure 5.9. However, comparing steps up to different final voltages (not shown) the response time increased significantly with increasing final voltage. For instance, steady state was reached within appr. 200 s for steps up to 1.03 V but only in appr. 0.15 s for steps up to 0.48 V.

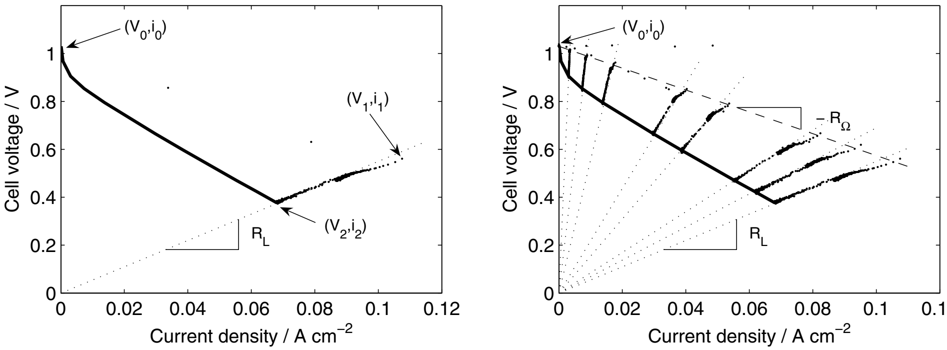

Figure 5.8: Left: Transient response (dots) plotted in the V-i diagram for a step in the external load resistance, R_L, from 470 to 0.27 Ω. The steady-state polarisation curve is shown as a thick solid line. Right: Same plot as to the left for all steps in R_L from 470 Ω to lower values. The slope of the dashed line is R_Ω, the ohmic resistance of the cell. Dotted curves have slopes equal to the different values of R_L after the step.

Another consequence of the sluggish response at high cell voltages is that a step from high to low cell voltage has shorter response time than the reverse step back to high cell voltage. For instance the response time of a step with initial voltage 1.0 V and final voltage 0.47 V was 42 ms while the reverse step back to 1.0 V had a response time of 0.60 s.

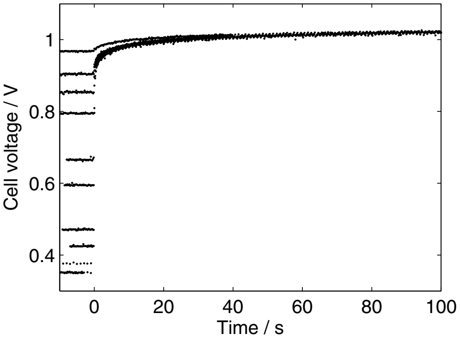

Figure 5.9: Transient response in cell voltage to a change in the external load resistance from low values to 470 Ω (opposite steps as in Figure 5.6).

5.4.3 Electrochemical impedance spectroscopy

The analysis of the previous section did not suggest which process(es) gave rise to the observed response. EIS was thus applied to relate the observed response to physical processes in the AFC. Due to the large ohmic resistance of the anode, EIS was applied to a half-cell set-up. However, the anode reaction is known to have substantially faster kinetics than the cathode reaction [2], so the anode could still be used as counter electrode.

A Nyquist diagram of the cathode impedance at different cathode potentials is shown in Figure 5.10. The impedance spectra were shaped like depressed semicircles with a potential dependent radius offset from the origin by a constant real impedance. The constant real impedance of 2.02 Ω cm^2 reflects the uncompensated ohmic resistance between the cathode potential probe and the reference electrode. Potential dependent semicircles can be attributed to a charge transfer reaction [36], thus we take this as an indication that the measured impedance response reflects the cathode charge transfer reaction. Note also that the potential dependence of the semicircle radius is more pronounced at high cell voltages. This can be expected for charge transfer related impedance spectra since there is an exponential relationship between the potential and current density for processes controlled by charge transfer. Similar potential dependence was seen in Figure 5.7 for the AFC response time.

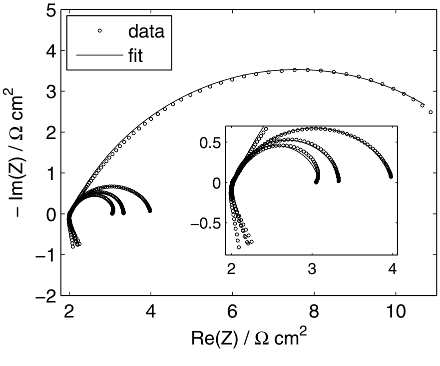

Figure 5.10: Nyquist diagram of the cathode impedance (o) and fit (-) at electrode potentials corresponding to cell voltages 0.9 V (largest arc), 0.8 V, 0.7 V and 0.6 V (smallest arc). Inset shows an expanded high frequency region. The equivalent circuit is shown in Figure 5.4.

Table 5.1: Fitted parameters of the spectra showed in Figure 5.10. C_{CPE} and τ_{EC} are calculated from expressions given in Section 5.3.

Cell voltage / V	R_c / $\Omega\ \mathrm{cm}^2$	T / $\mathrm{mF\ cm^{-2}\ s^{\phi-1}}$	ϕ	C_{CPE} / $\mathrm{mF\ cm^{-2}}$	τ_{CPE} / s
0.90	11.1	188	0.721	121	1.34
0.80	2.02	146	0.750	76.9	0.155
0.70	1.34	97.6	0.848	61.9	0.083
0.60	1.07	15.6	0.898	9.3	0.010

Depressed semicircles most likely reflect the porous structure of the electrode [32]. At high polarisation, the impedance exhibits an inductive behaviour at low frequencies (Figure 5.10, inset). According to Bultel et al. [37], this behaviour can be related to intermediate adsorbed species in a three-step oxygen reduction mechanism.

As shown in Figure 5.10, the equivalent circuit in Figure 5.4 gave an excellent fit of the measured impedance spectra, which can be expected when using CPEs. Numerically extracted parameters are shown in Table 5.1. The potential dependent semicircle radius is reflected in the potential dependent values of R_c. Fitted values of ϕ are less than 1 due to the depressed shape of the semicircles. Calculated values of the equivalent capacitance, C_{CPE}, decrease with decreasing cell voltage. This trend is difficult to explain, especially since the physical interpretation of CPEs is controversial, but may be partly related to a reduced electrode area available for reaction at decreasing cell voltages. However, the response time of the equivalent circuit, τ_{EC}, shows the same potential dependence and has the same order of magnitude as τ_{FC}, the response time for the fuel cell upon load steps (see Figure 5.7). This supports our interpretation that the potential dependence of τ_{FC} stems from the cathode charge transfer reaction.

In summary, results from EIS indicate that the cathode charge transfer reaction is causing the potential dependent response of the AFC. This process is slower at higher cell voltages where the resistance to charge transfer is higher and the driving force of the reaction is smaller.

5.5 Conclusion

We have studied the dynamic behaviour of a single AFC using load step measurements assisted by EIS. The purpose of this paper was to address how fast the AFC reached steady state after a load step, the characteristic shape of the response curves and the physical origin of the transient response. The AFC was supplied with pure hydrogen and oxygen in excess, so that mass transport limitations were reduced. Reported results thus indicated the lower limit for AFC response times. Load steps were realised connecting the AFC to an in-house designed resistance board where the total external load resistance could be changed within 30 μs. The response time for steps between various steady-state operating points was measured and found to depend on the initial and final voltage. EIS indicated that the charge transfer reaction at the cathode is limiting the response, giving a potential dependent response time varying on a time scale of appr. 10 ms to 10 s depending on the initial and final cell voltages. In the operating range typical for practical applications, response times less than 1 s were obtained. This is sufficient for automotive applications, but a slower response can be expected when the AFC is supplied with air instead of pure oxygen. For steps in the range near open circuit, response times of several seconds were obtained, which may require special control strategies. Transient response curves were plotted in the V-i diagram and were shown to follow a pattern determined by the load resistance and ohmic resistance of the AFC.

Acknowledgement

The Research Council of Norway and Aker Kværner Power & Automation Systems AS are kindly acknowledged for financial support.

References

[1] G. F. McLean, T. Niet, S. Prince-Richard, and N. Djilali, *Int. J. Hydrogen Energy*, **27**, 507 (2002).

[2] J. Larminie and A. Dicks, *Fuel cell systems explained*, John Wiley & Sons, Ltd., Hoboken (2000).

[3] E. De Geeter, M. Mangan, S. Spaepen, W. Stinissen, and G. Vennekens, *J. Power Sources*, **80**, 207 (1999).

[4] K. Kordesch, J. Gsellmann, M. Cifrain, S. Voss, V. Hacker, R. R. Aronson, C. Fabjan, T. Hejze, and J. Daniel-Ivad, *J. Power Sources*, **80**, 190 (1999).

[5] K. Kordesch, V. Hacker, J. Gsellmann, M. Cifrain, G. Faleschini, P. Enzinger, R. Fankhauser, M. Ortner, M. Muhr, and R. R. Aronson, *J. Power Sources*, **86**, 162 (2000).

[6] P. Gouérec, L. Poletto, J. Denizot, E. Sanchez-Cortezon, and J. H. Miners, *J. Power Sources*, **129**, 193 (2004).

[7] A. Damjanovic, M. A. Genshaw, and J. O. Bockris, *J. Electrochem. Soc.*, **114**, 466 (1967).

[8] E. Yeager, *Electrochim. Acta*, **29**, 1527 (1984).

[9] K. A. Striebel, F. R. McLarnon, and E. J. Cairns, *J. Electrochem. Soc.*, **137**, 3360 (1990).

[10] A. Lundblad and P. Björnbom, *J. Electrochem. Soc.*, **139**, 1337 (1992).

[11] A. Lundblad and P. Björnbom, *J. Electrochem. Soc.*, **141**, 1503 (1994).

[12] K. Tomantschger, R. Findlay, M. Hanson, K. Kordesch, and S. Srinivasan, *J. Power Sources*, **39**, 21 (1992).

[13] E. Gülzow, M. Schulze, and G. Steinhilber, *J. Power Sources*, **106**, 126 (2002).

[14] M. Schulze and E. Gülzow, *J. Power Sources*, **127**, 252 (2004).

[15] N. Wagner, M. Schulze, and E. Gülzow, *J. Power Sources*, **127**, 264 (2004).

[16] E. Gülzow and M. Schulze, *J. Power Sources*, **127**, 243 (2004).

[17] M. T. Ergül, L. Türker, and I. Eroğlu, *Int. J. Hydrogen Energy*, **22**, 1039 (1997).

[18] E. Han, I. Eroğlu, and L. Türker, *Int. J. Hydrogen Energy*, **25**, 157 (2000).

[19] A. O. Yazaydin, I. Eroğlu, and E. Han, *Chem. Eng. Comm.*, **190**, 976 (2003).

[20] V. I. Matryonin, A. T. Ovchinikov, and A. P. Tzedilkin, *Int. J. Hydrogen Energy*, **22**, 1047 (1997).

[21] S. Kim, S. Shimpalee, and J. W. Van Zee, *J. Electrochem. Soc.*, **152**, A1265 (2005).

[22] J. Kallo, J. Kamara, W. Lehnert, and R. von Helmholt, *J. Power Sources*, **127**, 181 (2004).

[23] C. Haynes, *J. Power Sources*, **109**, 365 (2002).

[24] W. He and Q. Chen, *J. Power Sources*, **73**, 182 (1998).

[25] S. Gultekin, M. A. Al-Saleh, A. S. Al-Zakri, and A. I. Inamah, *Arab. J. Sci. Eng.*, **17**, 465 (1992).

[26] P. W. Brennecke, H. H. Ewe, E. W. Justi, and H.-J. Selbach, *Energ. Convers. Manage.*, **25**, 469 (1985).

[27] D. B. Zhou and H. Vander Poorten, *Electrochim. Acta*, **40**, 1819 (1995).

[28] L. Genies, Y. Bultel, R. Faure, and R. Durand, *Electrochim. Acta*, **48**, 3879 (2003).

[29] R. K. Ahluwalia and X. Wang, *J. Power Sources*, **139**, 152 (2005).

[30] H. Weydahl, S. Møller-Holst, G. Hagen, and B. Børresen, *J. Electrochem. Soc.*, submitted December 2005.

[31] M. Ciureanu and R. Roberge, *J. Phys. Chem. B*, **105**, 3531 (2001).

[32] R. L. Hurt and J. R. MacDonald, *Solid State Ionics*, **20**, 111 (1986).

[33] A. Lasia, in *Modern Aspects of Electrochemistry*, B. E. Conway, J. O. M. Bockris, and R. E. White, editors, vol. 32, chap. 2, pp. 143–247, Kluwer Academic/Plenum Publishers, New York (1999).

[34] H. Weydahl, S. Møller-Holst, T. Burchardt, and G. Hagen, Dynamic behaviour of an alkaline fuel cell - results from introductory experiments, Poster at 1st European Hydrogen Energy Conference (2003).

[35] F. Zenith, H. Weydahl, I. A. Lervik, T. Burchardt, S. Møller-Holst, S. Skogestad, and G. Hagen, Simulation and experimental study of the transient response of fuel cells, Poster at 9th Ulm Electrochemical Talks (2004).

[36] Southampton Electrochemistry Group, *Instrumental methods in electrochemistry*, Chemical Science Series, Horwood Publishing Limited (2001).

[37] Y. Bultel, L. Genies, O. Antoine, P. Ozil, and R. Durand, *J. Electroanal. Chem.*, **527**, 143 (2002).

Chapter 6

Transient model of an alkaline fuel cell cathode

H. Weydahl[a], A. M. Svensson[b], and S. Sunde[a]

[a]Department of Materials Science and Engineering, NTNU, NO-7491 Trondheim, Norway
[b]SINTEF Materials and Chemistry, NO-7465 Trondheim, Norway

Abstract: An iso-thermal, one-dimensional, transient model of an alkaline fuel cell (AFC) cathode was developed, based on mass balances for oxygen and ionic species and flooded-agglomerate theory. Model results show the coupled effects of oxygen diffusion, ion transport and propagation of local electrode potential on the response in current density to a cathodic step in electrode potential. For a set of base case parameters, oxygen diffusion and potential propagation, with characteristic time constants of 0.30 and 0.11 ms, respectively, dominated the current response up to appr. 1 ms, while the slower ion diffusion with time constant 5.0 s controlled the final relaxation towards steady state at appr. 60 s. A smaller agglomerate radius and electrode thickness and a smaller double layer capacitance gave faster electrode response. For a cathodic step in electrode potential, an overshoot in faradaic current appeared around 0.5 ms. This overshoot was related to an initially higher oxygen concentration in the agglomerates, but was masked by capacitive current for base case parameters. Simulated response in oxygen concentration profiles suggested that the potential dependent response time found in previous studies can be related to consumption of surplus oxygen in the catalyst layer.

6.1 Introduction

Fuel cells are considered as promising candidates for replacing the conventional internal combustion engine, eliminating CO_2 emissions from the transportation sector and reducing the dependence on oil. The alkaline fuel cell (AFC) is a cheap, robust and reliable alternative to the more popular proton exchange membrane fuel cell (PEMFC) [1], but has received less attention over the recent years. It is considered less viable than PEMFC technology since CO_2 from air may form carbonates in the electrolyte, reducing AFC performance. However, Gülzow and Schulze claim that these problems may be overcome using a circulating electrolyte [2].

For fuel cells to succeed as power generators in applications with varying power demands, such as vehicles, their dynamic capability is of great importance. The dynamic behaviour of PEMFCs has been studied to some extent (see e.g. [3–8]), but corresponding studies of the AFC technology are missing in the open literature.

Transient phenomena in fuel cells are not easily accessible for measurements. Local changes in potential and reactant concentration within the fine structure of the electrode are difficult, if not impossible, to measure. Also, fast transient phenomena can only be captured by high resolution measurements which are often disturbed by noise. A mathematical model can be a powerful tool to illustrate local changes in key variables and how these combine to give the total transient response of the fuel cell to a load step. Model results can hence facilitate interpretation of experimental data and help to distinguish the effects of various coupled phenomena.

A key challenge in fuel cell modelling is the geometric structure of the catalyst layer. The highly porous, multi-phase structure can not be modelled in geometric detail without causing inadequate model complexity and high computation time. One approach to meet this challenge is the flooded-agglomerate model [9]. This approach couples a microscopic model of the porous catalyst particles with a macroscopic model of the catalyst layer, treating the electrode as a continuum. This way, transport processes on a microscopic scale near the active catalyst sites are coupled to transport processes on a macroscopic scale in the electrode. Perry et al. [10] applied this approach to develop a stationary model of the cathode of a liquid-electrolyte fuel cell (including AFC). In their model, the coupled effects of reactant transport, electrode potential and faradaic reaction were accounted for.

In the transient state, changes in reactant concentration and electrode potential must be accounted for, so both faradaic and capacitive effects must be included in the source terms. A transient model provides valuable insight into the interactions between dynamic processes in the electrode, showing how local transient processes on the microscopic level affect measurable quantities.

In this work, we develop a transient model of an AFC cathode. The purpose of this study is to identify parameters improving the dynamic behaviour of the electrode and determine how oxygen diffusion, ion transport and potential propagation affect the current response. Model results also reveal local effects that can not be observed experimentally. We first describe the physical model of the electrode, state the governing equations and derive a dimensionless formulation of the equation set. We then present the solution method and identify a base case parameter set. Model results are presented for a cathodic step in electrode potential and effects of oxygen diffusion, ion transport and potential propagation on the transient response are discussed.

6.2 Physical model

Consider the cathode of an AFC with 6 M potassium hydroxide (KOH) as electrolyte. We assume constant temperature and consider the response in electrolyte concentration, electrode potential and oxygen concentration throughout the electrode when the electrode potential is changed by an external potentiostat. The cathode geometry is modelled according to Perry et al. [10] as a cluster of spherical, porous carbon agglomerates mixed with platinum (Pt) as shown in Fig. 6.1. The open space between the agglomerates is hydrophobic and filled with pure oxygen which is supplied to the electrode from the cathode gas channel. The pores inside the porous agglomerates are hydrophilic and filled with liquid electrolyte which is kept stagnant by capillary forces. The electrode thus consists of three phases: i) a solid phase (carbon and Pt in the porous agglomerates), ii) a liquid phase (electrolyte-filled pores in agglomerates) and iii) a gaseous phase (pure oxygen in open space between agglomerates). Assuming that all agglomerate pores are completely filled with electrolyte, the volume fractions of the three phases are related according to

$$\epsilon_g + \epsilon_s + \epsilon_l = 1 \tag{6.1}$$

where ϵ_g, ϵ_s and ϵ_l are the volumes of gas, solid and liquid phase per unit electrode volume, respectively.

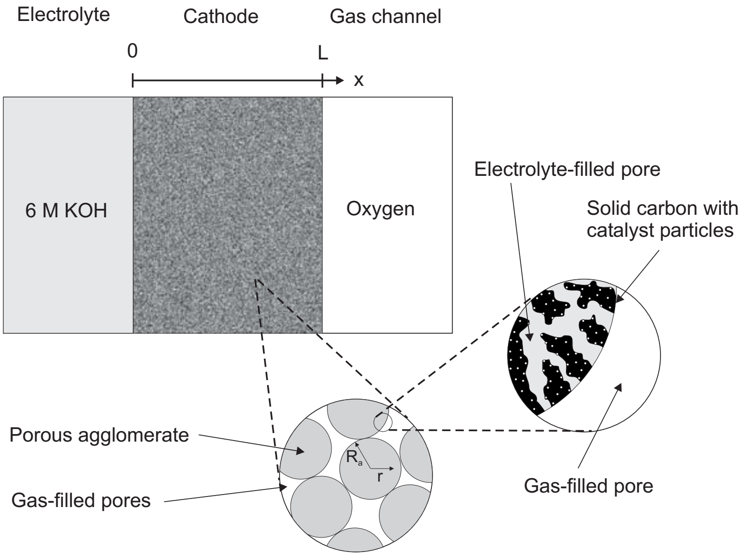

Figure 6.1: Schematic diagram of the electrode according to Perry et al. [10].

Gaseous oxygen dissolves in the electrolyte flooding the agglomerate pores and diffuses to the active sites in the agglomerate. The electrochemical reaction takes place on Pt particles which are in contact with the ion conducting electrolyte and the electronically conducting carbon. As assumed by Kimble and White [11] and Perry et al. [10] the electrochemical reaction occurs as a one-step transfer of four electrons

$$2\mathrm{H_2O} + \mathrm{O_2} + 4\mathrm{e}^- \rightarrow 4\mathrm{OH}^- \tag{6.2}$$

Electrons are supplied to the active sites from the solid phase of the agglomerate. The solid phase forms a continuum where electrons are free to move between neighbouring agglomerates. Likewise, the liquid phase forms a continuum where ions are free to move between pores in neighbouring agglomerates.

A charge double layer forms on the pore walls in the agglomerate, not only on active sites, but on the total surface area of carbon and Pt in contact with electrolyte. Water molecules and K^+ and OH^- ions are all incorporated in this layer. A change in the total charge in the solid phase forces an equal and opposite change in the total charge of K^+ and OH^- ions in the double layer. A positive increase of charge in the double layer is facilitated by absorbing K^+ ions and rejecting OH^- ions.

The radius of the porous agglomerates, R_a, is assumed to be the same for all agglomerates. Transport of dissolved oxygen in the porous agglomerates is assumed spherically symmetric, and is therefore represented one-dimensionally along the radial coordinate, r (Fig. 6.1). Moreover, R_a is assumed to be much smaller than the electrode thickness, L, so the electrode potential and electrolyte concentration are assumed constant within each agglomerate, leaving oxygen concentration as the only variable changing along the radial dimension. Electrode potential and electrolyte concentration vary one-dimensionally along the electrode coordinate, x. This means that the oxygen concentration profile along r is the same in all agglomerates situated at the same position x in the electrode.

Our model thus consists of a microscopic agglomerate model along r and a macroscopic electrode model along x. The electrode potential affects the electrochemical reaction rate in the agglomerates, coupling the macroscopic model to the microscopic model. Production of ions in the faradaic reaction and removal/addition of ions by the double layer affect the electrolyte concentration, coupling the microscopic model to the macroscopic model.

6.3 Mathematical formulation

6.3.1 Basic assumptions

In addition to the assumptions made when setting up the physical model, the following are assumed to hold:

1. Temperature is constant throughout the electrode.
2. There is no ohmic resistance in the solid phase of the electrode.
3. The oxygen pressure in the gas-filled pores is constant throughout the electrode.
4. Gaseous oxygen is in equilibrium with dissolved oxygen at the agglomerate surface.
5. Oxygen flux in the agglomerate is spherically symmetric.
6. Transport of dissolved oxygen to active sites occurs by diffusion.
7. Oxygen adsorbed on the active sites immediately reacts to form OH^- ions.

8. Ion transport obeys the dilute solution approximation and occurs by diffusion and migration only (as assumed by Perry et al. [10]).
9. Electrolyte convection is negligible.
10. Changes in electrolyte concentration due to water production are negligible compared to changes caused by ion production.
11. The electrochemical reaction is first-order in oxygen concentration.
12. There is no flux of electrolyte and no ionic current density into the oxygen gas channel

6.3.2 Governing equations

We first consider the transport of dissolved oxygen in an agglomerate. Based on assumptions 5 and 6, the mass balance of dissolved oxygen in the electrolyte-filled pores of an agglomerate gives

$$\frac{\partial \epsilon_a c_O}{\partial t} = -\frac{1}{r^2}\frac{\partial}{\partial r} r^2 N_O + S_O \tag{6.3}$$

where c_O is the concentration of dissolved oxygen, N_O is the flux of oxygen through a spherical surface with radius r, and S_O is the production of oxygen per unit time and agglomerate volume. ϵ_a is the volume of electrolyte-filled pores per unit agglomerate volume, thus $\epsilon_a c_O$ is the number of moles of oxygen per unit agglomerate volume.

The flux of dissolved oxygen is given by Fick's law

$$N_O = -\frac{\epsilon_a}{\tau_a} D_O \frac{\partial c_O}{\partial r} \tag{6.4}$$

where the free stream diffusivity of oxygen, D_O, is corrected for the porous structure of the agglomerate by multiplying with ϵ_a/τ_a, where τ_a is the tortuosity of the pores in the agglomerate.

Oxygen is consumed in the electrochemical reaction, so

$$S_O = -\frac{a_a s_O}{nF} i_{n,\text{far}} \tag{6.5}$$

where a_a is the active area per unit agglomerate volume, s_O and n are the stoichiometric coefficients of oxygen and electrons, respectively, F is Faraday's constant and $i_{n,\mathrm{far}}$ is the faradaic current per unit active area. Since the faradaic current is cathodic and oxygen is reduced, s_O and $i_{n,\mathrm{far}}$ are negative by convention. This gives a negative source term, S_O.

Next, we consider the transport of ions in the liquid phase. The mass balance for species i, where i stands for + (K^+ ions) or − (OH^- ions), gives

$$\frac{\partial \epsilon_l c_i}{\partial t} = -\frac{\partial}{\partial x} N_i + S_i \tag{6.6}$$

where c_i is the concentration of species i, N_i is the flux of species i through a plane perpendicular to the x-axis and S_i is the production of species i per unit time and electrode volume. Since ϵ_l is the volume of electrolyte-filled pores per unit electrode volume, $\epsilon_l c_i$ is the number of moles of species i per unit electrode volume.

The flux of species i in the electrolyte is given by the Nernst-Planck equation

$$N_i = -z_i \frac{\epsilon_l}{\tau_l}\, u_i F c_i \frac{\partial \Phi_2}{\partial x} - \frac{\epsilon_l}{\tau_l}\, D_i \frac{\partial c_i}{\partial x} \tag{6.7}$$

where z_i is the charge number of species i, Φ_2 is the electric potential of the electrolyte and u_i and D_i are the mobility and free stream diffusivity of species i, respectively. Mobilities and diffusivities are corrected for the porosity and tortuosity of the electrode by multiplying with ϵ_l/τ_l, where τ_l is the tortuosity of the pores in the electrode. Note that this tortuosity is larger than τ_a, since clustering of the agglomerates adds to the tortuosity of the pores in each agglomerate.

Since K^+ ions are not involved in the electrochemical reaction, the source term for K^+ ions contains a capacitive contribution only. For a cathodic change in electrode potential, the electric surface charge of the solid phase in the electrode decreases. This brings along a corresponding increase in the ionic charge of the double layer by absorbing K^+ ions into the double layer and releasing OH^- ions. For an incremental change in surface charge of the solid phase, dq, the incremental change in ionic double layer charge due to K^+ ions, dq_+, and OH^- ions, dq_-, are related by

$$-dq = dq_+ + dq_- \tag{6.8}$$

Based on the treatment of Verbrugge and Liu [12]

$$S_+ = -\frac{a_{dl} C_{dl} (1 - \epsilon_g)}{z_+ F} \frac{dq_+}{dq} \frac{\partial(\Phi_1 - \Phi_2)}{\partial t} \tag{6.9}$$

where a_{dl} is the surface area of carbon and Pt in the electrolyte-filled agglomerate pores per unit agglomerate volume, C_{dl} is the double layer capacitance per unit surface area of carbon and Pt and Φ_1 is the electric potential of the solid phase. For a cathodic change in potential, $\partial(\Phi_1 - \Phi_2)/\partial t$ is negative, giving a negative S_+. This is correct, since K$^+$ ions are removed from the electrolyte and absorbed by the double layer during a cathodic change in potential. The factor $(1 - \epsilon_g)$ gives the agglomerate volume (both solid and liquid phase) per unit electrode volume, so S_+ gives the production of K$^+$ ions per unit time and electrode volume.

OH$^-$ ions are produced in the electrochemical reaction and are released to the electrolyte from the double layer during a cathodic change in potential. The sum of faradaic and capacitive contributions gives

$$S_- = -\frac{s_-}{nF}\rho_a I_a - \frac{a_{dl} C_{dl}(1 - \epsilon_g)}{z_- F}\frac{dq_-}{dq}\frac{\partial(\Phi_1 - \Phi_2)}{\partial t} \tag{6.10}$$

where s_- is the stoichiometric coefficient of OH$^-$ ions, ρ_a is the number of agglomerates per unit electrode volume and I_a is the faradaic current produced per agglomerate. Since the faradaic current is cathodic and OH$^-$ ions are produced in the oxygen reduction reaction, I_a is negative and s_- is positive, giving a positive faradaic source term. The capacitive source term for OH$^-$ during a cathodic change in potential is positive since OH$^-$ ions are released to the electrolyte from the double layer.

For a more compact notation, we introduce the effective diffusivity of oxygen, K$^+$ ions and OH$^-$ ions according to

$$\tilde{D}_O = \frac{\epsilon_a}{\tau_a} D_O \tag{6.11}$$

$$\tilde{D}_+ = \frac{\epsilon_l}{\tau_l} D_+ \tag{6.12}$$

$$\tilde{D}_- = \frac{\epsilon_l}{\tau_l} D_- \tag{6.13}$$

respectively, and the effective mobility of K$^+$ ions and OH$^-$ according to

$$\tilde{u}_+ = \frac{\epsilon_l}{\tau_l} u_+ \tag{6.14}$$

$$\tilde{u}_- = \frac{\epsilon_l}{\tau_l} u_- \tag{6.15}$$

respectively.

A common electrolyte concentration is defined as

$$c_e = \frac{c_+}{\nu_+} = \frac{c_-}{\nu_-} \tag{6.16}$$

where ν_+ and ν_- are the number of K^+ and OH^- ions, respectively, that each KOH molecule dissociates into.

The electrode potential is manipulated using an external potentiostat connected to the solid phase of the electrode and a suitable reference electrode. We define the electrode potential, V, as $V = \Phi_1 - \Phi_1^{\text{ref}}$, where Φ_1^{ref} is the solid phase potential of the standard hydrogen electrode. A cathodic change in electrode potential corresponds to a decrease in V. The electrode potential at a position x corresponds to the potential measured if the reference electrode was positioned at the same x. In real experiments, only $V(x = 0)$ can be measured, corresponding to a case where the reference electrode is positioned in the bulk electrolyte just outside the electrode. $V(x = 0)$ corresponds to the electrode potential measured by Sepa et al. [13] who provide the experimental basis for the kinetic expression used in our model. Imposing a step in electrode potential with a potentiostat corresponds to setting the value of $V(x = 0)$.

Assuming that the solid and liquid phase potentials in the reference electrode are equal and that there is no liquid-junction potential difference in the salt bridge connection between the reference and the liquid phase of the electrode, we can set $\Phi_1^{\text{ref}} = \Phi_2$, thus

$$V = \Phi_1 - \Phi_2 \tag{6.17}$$

Since there is no ohmic resistance in the solid phase of the electrode, $\partial\Phi_1/\partial x = 0$, and

$$\partial\Phi_2/\partial x = -\partial V/\partial x \tag{6.18}$$

The faradaic current per unit active area is given by [10, 13]

$$i_{n,\text{far}} = -nFkc_O \exp(-\ln(10)V/b) \tag{6.19}$$

where

$$b = -\frac{\partial V}{\partial \log(i_{n,\text{far}})} \tag{6.20}$$

The faradaic current is negative by convention since we consider a cathodic reaction. The kinetic expression is formulated in terms of electrode potential, V, instead of overpotential, as suggested by Sepa et al. [13] who provide the experimental basis for the kinetic expression. This expression is valid for a Pt electrode in alkaline environment at electrode potentials less than 0.2 V vs. SHE.

The total faradaic current produced in one agglomerate, I_a, is found by integrating the faradaic current over the agglomerate volume

$$I_a = 4\pi \int_0^{R_a} a_a i_{n,\mathrm{far}} r^2 dr \tag{6.21}$$

This equation couples the source term in the mass balance for dissolved oxygen (ref. Eq. (6.5)) to the source term in the mass balance for OH^- ions (ref. Eq. (6.10)).

The total current density is found by integrating the local faradaic and capacitive current production over the electrode thickness

$$i_{\mathrm{tot}} = \int_0^L \rho_a I_a dx + \int_0^L a_{dl} C_{dl} (1 - \epsilon_g) \partial V / \partial t \ dx \tag{6.22}$$

Here, the first term on the right hand side is the total faradaic current density and the second term is the total capacitive current density. Since V is a function of x only, the capacitive current production is the same for all r at a given position x, so the local capacitive current production is $a_{dl} C_{dl}$ $(1 - \epsilon_g) \partial V / \partial t$.

6.4 Analysis

Inserting Eqs. (6.4), (6.5), (6.11), and (6.19) into Eq. (6.3) we obtain

$$\frac{\partial \epsilon_a c_O}{\partial t} = \tilde{D}_O \frac{1}{r^2} \frac{\partial}{\partial r} r^2 \frac{\partial c_O}{\partial r} + a_a s_O k c_O \exp(-\ln(10) V / b) \tag{6.23}$$

Inserting flux equations (Eq. (6.7)) and source terms (Eqs. (6.9) and (6.10)) into their respective mass balances (Eq. (6.6)), using Eqs. (6.16), (6.12-6.15) and (6.17-6.18), we obtain

$$\epsilon_l \frac{\partial c_e}{\partial t} = -z_+ \tilde{u}_+ F \frac{\partial}{\partial x} \left(c_e \frac{\partial V}{\partial x} \right) + \tilde{D}_+ \frac{\partial^2 c_e}{\partial x^2} - \frac{a_{dl} C_{dl} (1 - \epsilon_g)}{z_+ \nu_+ F} \frac{dq_+}{dq} \frac{\partial V}{\partial t} \tag{6.24}$$

$$\epsilon_l \frac{\partial c_e}{\partial t} = -z_- \tilde{u}_- F \frac{\partial}{\partial x} \left(c_e \frac{\partial V}{\partial x} \right) + \tilde{D}_- \frac{\partial^2 c_e}{\partial x^2} - \frac{a_{dl} C_{dl} (1 - \epsilon_g)}{z_- \nu_- F} \frac{dq_-}{dq} \frac{\partial V}{\partial t} - \frac{s_-}{\nu_- n F} \rho_a I_a \tag{6.25}$$

By subtracting Eq. (6.24) from Eq. (6.25) we obtain a partial differential equation (PDE) for the electrode potential

$$\frac{a_{dl}C_{dl}(1-\epsilon_g)}{F}\left(\frac{1}{z_-\nu_-}\frac{dq_-}{dq}-\frac{1}{z_+\nu_+}\frac{dq_+}{dq}\right)\frac{\partial V}{\partial t}=$$

$$F\left(z_+\tilde{u}_+-z_-\tilde{u}_-\right)\frac{\partial}{\partial x}\left(c_e\frac{\partial V}{\partial x}\right)-\left(\tilde{D}_+-\tilde{D}_-\right)\frac{\partial^2 c_e}{\partial x^2}-\frac{s_-}{\nu_- nF}\rho_a I_a \qquad (6.26)$$

By using Eq. (6.26), we eliminate the time derivate of V from Eq. (6.24) and obtain a PDE for c_e

$$\epsilon_l\left(\frac{1}{z_-\nu_-}\frac{dq_-}{dq}-\frac{1}{z_+\nu_+}\frac{dq_+}{dq}\right)\frac{\partial c_e}{\partial t}=$$

$$-F\left(z_+\tilde{u}_+\frac{1}{z_-\nu_-}\frac{dq_-}{dq}-z_-\tilde{u}_-\frac{1}{z_+\nu_+}\frac{dq_+}{dq}\right)\frac{\partial}{\partial x}\left(c_e\frac{\partial V}{\partial x}\right)$$

$$+\left(\tilde{D}_+\frac{1}{z_-\nu_-}\frac{dq_-}{dq}-\tilde{D}_-\frac{1}{z_+\nu_+}\frac{dq_+}{dq}\right)\frac{\partial^2 c_e}{\partial x^2}+\frac{1}{z_+\nu_+}\frac{dq_+}{dq}\frac{s_-}{\nu_- nF}\rho_a I_a \qquad (6.27)$$

6.4.1 Boundary and initial conditions

Eqs. (6.23), (6.26) and (6.27) require two boundary conditions and one initial condition each. According to assumptions 3-5 in Section 6.3.1, the boundary conditions for the oxygen mass balance are

$$c_O(r=R_a,\ t)=c_O^s, \qquad (6.28)$$

$$\frac{\partial c_O}{\partial r}(r=0,\ t)=0 \qquad (6.29)$$

for all x, where c_O^s is the concentration of dissolved oxygen at the agglomerate surface, given by the equilibrium concentration of dissolved oxygen in the electrolyte at the given conditions.

For an imposed step in electrode potential from V_0 to V_1 the boundary conditions of Eq. (6.26) are (ref. Eq. (6.79) of Appendix A)

$$V(x=0,\ t)=\ V_0+(V_1-V_0)H(t), \qquad (6.30)$$

$$\frac{\partial V}{\partial x}(x=L,\ t)=0, \qquad (6.31)$$

where $H(t)$ is the Heaviside step function. To avoid numerical difficulties, we applied a smooth step function (`flc1hs` [14]), changing from 0 to 1 within 1 μs.

According to assumption 12 in Section 6.3.1 and Eq. (6.76) of Appendix A, the boundary conditions of Eq. (6.27) are

$$c_e(x = 0,\ t) = c_e^b, \tag{6.32}$$

$$\frac{\partial c_e}{\partial x}(x = L,\ t) = 0 \tag{6.33}$$

where c_e^b is the bulk electrolyte concentration.

Initial conditions are obtained from the steady-state solution of Eqs. (6.23), (6.26) and (6.27) for $V(x = 0) = V_0$.

6.4.2 Dimensionless formulation

A dimensionless formulation is obtained by defining the following dimensionless variables

$$x^* = x/L \tag{6.34}$$

$$r^* = r/R_a \tag{6.35}$$

$$c_e^* = c_e/c_e^b \tag{6.36}$$

$$c_O^* = c_O/c_O^s \tag{6.37}$$

$$t^* = t/t_{sc} \tag{6.38}$$

$$V^* = V/V_{sc} \tag{6.39}$$

where

$$t_{sc} = R_a^2/\tilde{D}_O \tag{6.40}$$

and

$$V_{sc} = b/\ln(10) \tag{6.41}$$

are chosen scaling factors for time and electrode potential, respectively.

Substitution of dimensionless variables into Eqs. (6.23), (6.26) and (6.27) gives

$$\epsilon_a \frac{\partial c_O^*}{\partial t^*} = \frac{1}{r^{*2}} \frac{\partial}{\partial r^*} r^{*2} \frac{\partial c_O^*}{\partial r^*} + \xi_1\ c_O^* \exp(-V^*) \tag{6.42}$$

$$\xi_2\ \frac{\partial V^*}{\partial t^*} = \xi_3\ \frac{\partial}{\partial x^*}\left(c_e^* \frac{\partial V^*}{\partial x^*}\right) - \xi_4\ \frac{\partial^2 c_e^*}{\partial x^{*2}} - \xi_5 \tag{6.43}$$

$$\xi_6\ \frac{\partial c_e^*}{\partial t^*} = -\xi_7\ \frac{\partial}{\partial x^*}\left(c_e^* \frac{\partial V^*}{\partial x^*}\right) + \xi_8\ \frac{\partial^2 c_e^*}{\partial x^{*2}} + \xi_9 \tag{6.44}$$

respectively, with boundary conditions

$$\frac{\partial c_O^*}{\partial r^*}(r^* = 0,\ t) = 0, \qquad c_O^*(r^* = 1,\ t) = 1 \tag{6.45}$$

$$V^*(x^* = 0,\ t) = [V_0 + (V_1 - V_0)H(t)]/V_{sc}, \qquad \frac{\partial V^*}{\partial x^*}(x^* = 1,\ t) = 0 \tag{6.46}$$

$$c_e^*(x^* = 0,\ t) = 1, \qquad \frac{\partial c_e^*}{\partial x^*}(x^* = 1,\ t) = 0 \tag{6.47}$$

respectively, where

$$\xi_1 = \frac{a_a s_O k R_a^2}{\tilde{D}_O} \tag{6.48}$$

$$\xi_2 = \frac{a_{dl} C_{dl}(1 - \epsilon_g)}{F} \left(\frac{1}{z_- \nu_-} \frac{dq_-}{dq} - \frac{1}{z_+ \nu_+} \frac{dq_+}{dq} \right) \frac{V_{sc}}{c_e^b} \tag{6.49}$$

$$\xi_3 = F\left(z_+ \tilde{u}_+ - z_- \tilde{u}_-\right) \frac{V_{sc} t_{sc}}{L^2} \tag{6.50}$$

$$\xi_4 = \left(\tilde{D}_+ - \tilde{D}_-\right) \frac{t_{sc}}{L^2} \tag{6.51}$$

$$\xi_5 = \frac{t_{sc}}{c_e^b} \frac{s_-}{\nu_- n F} \rho_a I_a \tag{6.52}$$

$$\xi_6 = \epsilon_l \left(\frac{1}{z_- \nu_-} \frac{dq_-}{dq} - \frac{1}{z_+ \nu_+} \frac{dq_+}{dq} \right) \tag{6.53}$$

$$\xi_7 = F\left(z_+ \tilde{u}_+ \frac{1}{z_- \nu_-} \frac{dq_-}{dq} - z_- \tilde{u}_- \frac{1}{z_+ \nu_+} \frac{dq_+}{dq} \right) \frac{V_{sc} t_{sc}}{L^2} \tag{6.54}$$

$$\xi_8 = \left(\tilde{D}_+ \frac{1}{z_- \nu_-} \frac{dq_-}{dq} - \tilde{D}_- \frac{1}{z_+ \nu_+} \frac{dq_+}{dq} \right) \frac{t_{sc}}{L^2} \tag{6.55}$$

$$\xi_9 = \frac{1}{z_+ \nu_+} \frac{dq_+}{dq}\ \xi_5 \tag{6.56}$$

are dimensionless variables. Note that the parenthesis in Eq. (6.49) and (6.53) is equal to one for a binary electrolyte, regardless of the value of dq_+/dq and dq_-/dq.

6.5 Method of solution

The model was implemented in COMSOL Multiphysics™ version 3.2a [14]. This program uses the finite element method (FEM) to solve systems of coupled PDEs. The FEM discretisation of the time-dependent PDE problem is obtained with the method of lines giving a differential-algebraic equation (DAE) system. To solve the DAE system, COMSOL Multiphysics™ uses a version of the DAE solver DASPK [15, 16]. Thus, the solver is an implicit time-stepping scheme, solving a non-linear system of equations at each time step. The non-linear system is solved using a Newton iteration, and the resulting system is solved with the UMFPACK linear system solver. For further details, refer to Ref. [14].

Initial conditions were obtained by solving the model for a stationary state at the initial electrode potential. Stationary solution profiles were stored and used as initial values for the time dependent solution. The model was solved on a personal computer with 2 GHz processor and 480 Mbyte RAM. Typical computation time for a simulation was 2.5 hours.

6.6 Estimation of constant parameters

By choosing values of ϵ_g and ϵ_a, the volume fractions of liquid and solid phase in the electrode are

$$\epsilon_l = \epsilon_a(1 - \epsilon_g) \tag{6.57}$$

and

$$\epsilon_s = (1 - \epsilon_a)(1 - \epsilon_g) \tag{6.58}$$

respectively, which follow from the definition of ϵ_a and Eq. (6.1). We expect that agglomerate pores occupy a larger part of the agglomerate volume than gas pores in the electrode so that $\epsilon_a > \epsilon_g$.

The number of agglomerates per unit electrode volume is obtained by dividing the agglomerate volume (both solid and liquid phase) per unit electrode volume by the volume of one agglomerate, giving [10]

$$\rho_a = \frac{3(1 - \epsilon_g)}{4\pi R_a^3} \tag{6.59}$$

The active area per unit agglomerate volume, a_a, is assumed to be the same as the surface area of Pt per unit agglomerate volume, a_{Pt}. Technical specifications of Vulcan® XC-72 provide the surface area of Pt per unit mass catalyst, A_{Pt}, and the weight percent of Pt in the catalyst, $\mathrm{wt\%}_{\mathrm{Pt}}$ [17]. For a given Pt loading of the electrode, m_{Pt}, the surface area of Pt per unit agglomerate volume is (ref. Appendix B)

$$a_a = a_{\mathrm{Pt}} = \zeta \frac{A_{\mathrm{Pt}} m_{\mathrm{Pt}}}{\mathrm{wt\%}_{\mathrm{Pt}} L (1 - \epsilon_g)} \tag{6.60}$$

where ζ is a factor correcting for unavailable surface area. In the base case parameter set, ζ was set to 0.01 to obtain comparable current densities to those reported by Gouerec et al. [18].

Technical specifications of Vulcan® XC-72 also provide the surface area of carbon per unit mass catalyst, A_{C}. Assuming that the catalyst consists of carbon and Pt only, the weight percent of carbon in the catalyst is $\mathrm{wt\%_C} = 1 - \mathrm{wt\%_{Pt}}$. The surface area of carbon per unit agglomerate volume is therefore (ref. Appendix B)

$$a_{\mathrm{C}} = \zeta(1-\epsilon_a)\rho_{\mathrm{C}} A_{\mathrm{C}} \mathrm{wt\%_C} \tag{6.61}$$

where we have applied the same correction factor as for a_a.

Since the double layer forms on both carbon and Pt surface area, the total capacitance per unit agglomerate volume is

$$a_{dl} C_{dl} = a_{\mathrm{C}} C_{\mathrm{C}} + a_{\mathrm{Pt}} C_{\mathrm{Pt}} \tag{6.62}$$

where C_{C} and C_{Pt} are the capacitance per unit surface area of carbon and Pt, respectively.

For a chosen set of L, R_a, ϵ_a and ϵ_g, the geometry of the electrode is specified. The electrode active area and double layer area are specified by the chosen set of Pt loading, weight percent of Pt in the catalyst and surface area of Pt and carbon in the catalyst. Electrode and agglomerate tortuosities affect the effective mobilities and diffusivities, but do not influence geometric parameters.

As suggested by Verbrugge and Liu [12], we assume that K^+ and OH^- ions contribute equally to changes in ionic charge in the double layer. With this assumption, Eq. (6.8) gives

$$\frac{dq_+}{dq} = \frac{dq_-}{dq} = -0.5 \tag{6.63}$$

This means that the same number of K^+ and OH^- ions enters/leaves the double layer to accommodate a change in double layer charge.

The mobility of species i is given by [19, pg. 284]

$$u_i = \frac{\lambda_i}{|z_i| F^2} \tag{6.64}$$

where λ_i is the equivalent conductivity of species i. This quantity is given by [11]

$$\lambda_i = \Lambda \frac{\lambda_i^0}{\lambda_+^0 + \lambda_-^0} \tag{6.65}$$

Here, Λ is the equivalent conductivity of the electrolyte, calculated from an empirical expression in Ref. [11] for $c_e = c_e^b$ and $T = 298.15$ K. The ionic equivalent conductivity of species i at infinite dilution, λ_i^0, is given by Ref. [20] for both OH^- and K^+ ions.

The free stream diffusivity of species i is calculated from the equivalent conductivity [19, Eq. 11.46]

$$D_i = \frac{RT\lambda_i}{|z_i|F^2} \tag{6.66}$$

which follows from Eq. (6.64) and the Nernst-Einstein relation.

Stoichiometric coefficients of the modelled reaction (Eq. (6.2)) are defined according to [19, Eq. 2.6]

$$\sum_i s_i M_i^{z_i} \rightleftharpoons ne^- \tag{6.67}$$

which gives stoichiometric coefficients of electrons, oxygen, OH^- and K^+ ions as

$$n = 4, \quad s_O = -1, \quad s_- = 4, \quad s_+ = 0 \tag{6.68}$$

respectively.

The rate constant of oxygen reduction at 1 atm in 6 M KOH was estimated from the work of Sepa et al. [13]. Values of electrode potential and current density were extracted from Fig. 4 in Ref. [13] giving

$$\frac{i}{\exp[-\ln(10)V/b]} = nFkc_O \approx 0.0065 \text{ A cm}^{-2} \tag{6.69}$$

An oxygen pressure of 1 atm corresponds to $c_O = c_O^s$, thus

$$k \approx \frac{0.0065 \text{ A cm}^{-2}}{nFc_O^s} = 0.168 \text{ cm s}^{-1} \tag{6.70}$$

Base case parameters are listed in Table 6.1.

Table 6.1: Base case parameter values for 6 M KOH at 1 atm and 25 °C.

Parameter	Value	Unit	Source
A_{C}	$250 \cdot 10^7$	$\mathrm{cm^2\ kg^{-1}}$	[17]
A_{Pt}	$141 \cdot 10^7$	$\mathrm{cm^2\ kg^{-1}}$	[17]
a_a	$4.1 \cdot 10^3$	$\mathrm{cm^{-1}}$	Eq. (6.60)
a_{C}	$4.4 \cdot 10^4$	$\mathrm{cm^{-1}}$	Eq. (6.61)
a_{Pt}	$4.1 \cdot 10^3$	$\mathrm{cm^{-1}}$	Eq. (6.60)
$a_{dl}C_{dl}$	0.30	$\mathrm{F\ cm^{-3}}$	Eq. (6.62)
b	0.120	$\mathrm{V\ dec^{-1}}$	[10, 13]
C_{C}	$3 \cdot 10^{-6}$	$\mathrm{F\ cm^{-2}}$	[21]
C_{Pt}	$40 \cdot 10^{-6}$	$\mathrm{F\ cm^{-2}}$	[21]
c_e^b	$6.0 \cdot 10^{-3}$	$\mathrm{mol\ cm^{-3}}$	Chosen value
c_O^s	$1.0 \cdot 10^{-7}$	$\mathrm{mol\ cm^{-3}}$	[22]
D_O	$0.67 \cdot 10^{-5}$	$\mathrm{cm^2\ s^{-1}}$	[22]
$\tilde{D}_O$	$0.10 \cdot 10^{-7}$	$\mathrm{cm^2\ s^{-1}}$	Eq. (6.11)
D_+	$2.52 \cdot 10^{-5}$	$\mathrm{cm^2\ s^{-1}}$	Eq. (6.66)
$\tilde{D}_+$	$0.161 \cdot 10^{-5}$	$\mathrm{cm^2\ s^{-1}}$	Eq. (6.12)
D_-	$6.77 \cdot 10^{-5}$	$\mathrm{cm^2\ s^{-1}}$	Eq. (6.66)
$\tilde{D}_-$	$0.432 \cdot 10^{-5}$	$\mathrm{cm^2\ s^{-1}}$	Eq. (6.13)
dq_+/dq	-0.5		[12]
dq_-/dq	-0.5		[12]
F	96485.309	$\mathrm{C\ mol^{-1}}$	[23]
k	0.17	$\mathrm{cm\ s^{-1}}$	Eq. (6.70) and [13]
L	120	μm	[18]
m_{Pt}	$0.3 \cdot 10^{-6}$	$\mathrm{kg\ cm^{-2}}$	[18]
n	4		Eqs. (6.67) and (6.68)
R	8.31434510	$\mathrm{J\ K^{-1}\ mol^{-1}}$	[23]
R_a	1	μm	Own assumption
s_+	0		Eqs. (6.67) and (6.68)
s_-	4		Eqs. (6.67) and (6.68)
s_O	-1		Eqs. (6.67) and (6.68)
T	298.15	K	Chosen value
t_{sc}	$10 \cdot 10^{-3}$	s	Eq. (6.40)
u_+	$1.02 \cdot 10^{-8}$	$\mathrm{mol\ cm^2\ J^{-1}\ s^{-1}}$	Eq. (6.64)

$\tilde{u}_+$	$6.48 \cdot 10^{-10}$	mol cm^2 J^{-1} s^{-1}	Eq. (6.14)
u_-	$2.73 \cdot 10^{-8}$	mol cm^2 J^{-1} s^{-1}	Eq. (6.64)
$\tilde{u}_-$	$17.4 \cdot 10^{-10}$	mol cm^2 J^{-1} s^{-1}	Eq. (6.15)
V_{sc}	0.0521	V	Eq. (6.41)
wt%$_{\mathrm{C}}$	0.90		[17]
wt%$_{\mathrm{Pt}}$	0.10		[17]
z_+	1		Known
z_-	-1		Known
ϵ_a	0.30		Own assumption
ϵ_g	0.15		Own assumption
ϵ_l	0.26		Eq. (6.57)
ϵ_s	0.60		Eq. (6.58)
ζ	0.01		Chosen value
Λ	348.8	Ω^{-1} cm^{-2} mol^{-1}	[11]
λ_+^0	73.52	Ω^{-1} cm^{-2} mol^{-1}	[20]
λ_+	94.58	Ω^{-1} cm^{-2} mol^{-1}	Eq. (6.65)
λ_-^0	197.6	Ω^{-1} cm^{-2} mol^{-1}	[20]
λ_-	254.2	Ω^{-1} cm^{-2} mol^{-1}	Eq. (6.65)
ν_+	1		Known
ν_-	1		Known
ρ_a	$2.0 \cdot 10^{11}$	cm^{-3}	Eq. (6.59)
ρ_{C}	$2.26 \cdot 10^{-3}$	kg cm^{-3}	[23]
ρ_{Pt}	$21.4 \cdot 10^{-3}$	kg cm^{-3}	[23]
τ_a	3		Own assumption
τ_l	6		Own assumption
ξ_1	-6.95		Eq. (6.48)
ξ_2	$0.228 \cdot 10^{-4}$		Eq. (6.49)
ξ_3	$8.30 \cdot 10^{-4}$		Eq. (6.50)
ξ_4	$-1.87 \cdot 10^{-4}$		Eq. (6.51)
ξ_6	0.255		Eq. (6.53)
ξ_7	$-1.90 \cdot 10^{-4}$		Eq. (6.54)
ξ_8	$2.05 \cdot 10^{-4}$		Eq. (6.55)

6.7 Results and discussion

It was verified that stationary profiles from the COMSOL application were identical to those obtained by solving the steady-state model of Perry et al. [10]. We also tested that there was no drift in the model output for a time dependent solution with zero step size. The model was also tested versus analytical expressions provided by Crank [24, Eq. 4.17 and 6.18] for three cases: i) diffusion of oxygen into an agglomerate, ii) diffusion of ions into the electrode and iii) relaxation of electrode potential after a step in $V(x = 0)$. For case i, the initial oxygen concentration was zero and parameters were chosen so that electrolyte concentration and electrode potential were almost constant. For case ii, the initial electrolyte concentration was zero, oxygen concentration and electrode potential were constant and reaction rate was zero. For case iii, the oxygen and electrolyte concentrations were constant and the reaction rate was zero. Model outputs for these simplified cases were identical to analytical results. These tests do not verify transient results from the fully coupled model, but confirm that each model component produces correct results also in the time domain.

The coupling between oxygen and electrolyte concentration through the local faradaic current production, $\rho_a I_a$, was tested using an analytical expression for I_a at steady state for a given electrode potential (ref. [10, Eq. 6]). Replacing Eq. (6.21) with this expression represents a case where the relaxation of oxygen concentration profiles occurs infinitely fast. The model was run with the steady-state expression for I_a, and results were compared to those obtained with I_a given by Eq. (6.21). For base case parameters, model results for these two cases were identical for $t >$ appr. 10^{-3} s, where oxygen concentration is controlled by changes in electrode potential (ref. discussion later in this section). This indicates that the coupling of oxygen and electrolyte equations through $\rho_a I_a$ produces correct results.

To verify that discretisation was sufficiently fine, the model was solved with a coarser discretisation than what we used as standard. No change in model output was detected. Solving the model with tolerance limits increased ten times did not influence model output, confirming that model tolerance limits were sufficiently low.

Analytical solutions of the simplified cases i through iii above, give expressions for the characteristic time constant of oxygen diffusion, potential propagation and ion diffusion. These are (ref. Appendix C):

$$\tau_O = \frac{\epsilon_a R_a^2}{\pi^2 \tilde{D}_O} \tag{6.71}$$

$$\tau_V = \frac{4(1-\epsilon_g)L^2 a_{dl} C_{dl} \left(\frac{1}{z_-\nu_-}\frac{dq_-}{dq} - \frac{1}{z_+\nu_+}\frac{dq_+}{dq}\right)}{\pi^2 F^2 c_e^b (z_+\tilde{u}_+ - z_-\tilde{u}_-)} \tag{6.72}$$

$$\tau_e = \frac{4\epsilon_l L^2 \left(\frac{1}{z_-\nu_-}\frac{dq_-}{dq} - \frac{1}{z_+\nu_+}\frac{dq_+}{dq}\right)}{\pi^2 \left(\tilde{D}_+ \frac{1}{z_-\nu_-}\frac{dq_-}{dq} - \tilde{D}_- \frac{1}{z_+\nu_+}\frac{dq_+}{dq}\right)} \tag{6.73}$$

respectively. Note that $(1/(z_-\nu_-)dq_-/dq - 1/(z_+\nu_+)dq_+/dq)$ is unity for a binary electrolyte (ref. Eq. (6.8)). These expressions indicate that the response time of each process is determined by a characteristic length, a factor compensating for the volume where the process takes place, and a factor quantifying the speed of each process. For oxygen transport, the characteristic length is R_a, while $\tilde{D}_O$ quantifies the speed of oxygen transport through the electrolyte and ϵ_a compensates for the agglomerate volume not filled with electrolyte. This indicates that a smaller agglomerate gives faster response in oxygen transport. The agglomerate porosity has no influence on τ_O since ϵ_a also appears in $\tilde{D}_O$ (ref. Eq. (6.11)).

The processes involved in electrode potential propagation are double layer discharge and ion migration. These processes are coupled by charge balance and are therefore mutually dependent. A larger double layer capacitance leads to a slower relaxation, since more charge must be removed to accommodate a change in electrode potential. Higher mobility and electrolyte concentration decrease the value of τ_V since ions are more readily transported by migration. Note that capacitive discharge takes place in both solid and liquid phases, so only the gas-filled volume is compensated for by the factor $(1-\epsilon_g)$.

The time constant for ion diffusion, τ_e, depends on the characteristic length L, and the speed of ion diffusion. Note that only the liquid phase volume is involved in τ_e since diffusion occurs in the liquid phase only. Since ϵ_l also appears in $\tilde{D}_+$ and $\tilde{D}_-$ (ref. Eqs. (6.12) and (6.13)), electrode porosity has no influence on the time constant.

Base case parameters give $\tau_V = 0.11$ ms, $\tau_O = 0.30$ ms and $\tau_e = 5.0$ s, respectively. Electrode potential propagation is thus 3 times faster than oxygen diffusion, while ion diffusion is a much slower process. The large difference in response time for c_O and c_e is mainly caused by the difference between agglomerate radius and the much larger electrode thickness. Potential propagation is significantly faster than ion diffusion since capacitive discharge and migration of charged species are much faster processes than diffusion of a neutral ion pair.

In the following, we present model results for a cathodic step in electrode potential, using base case parameters (see Table 6.1). A step in $V(x = 0)$ from 0.1 to 0 V was applied, which is within the potential range where the kinetic expression in Eq. (6.19) is valid [13].

A step in V at $x = 0$ propagates into the electrode, eventually changing electrode potential in the full depth of the electrode. Electrode potential profiles for various time instances are shown in Fig. 6.2, and the electrode potential at chosen electrode positions as a function of time is shown in Fig. 6.3. These figures show that the change in electrode potential propagates through the electrode in appr. 0.05 ms. The main part of the change in electrode potential takes place in 0.1-1 ms, which corresponds well to the calculated time constant of potential propagation. The further relaxation to steady state takes appr. 50 s, which corresponds well to the calculated time constant of ion diffusion.

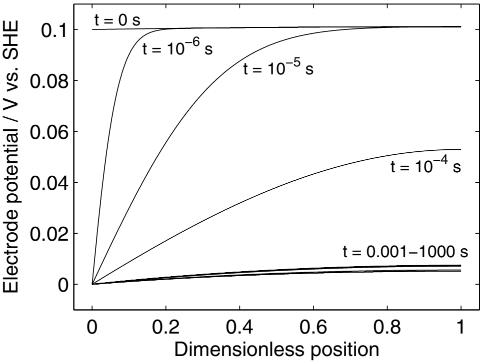

Figure 6.2: Electrode potential profiles at various time instances.

A cathodic change in electrode potentials causes an increased faradaic current production in the electrode. The local faradaic current production profiles for chosen time instances are shown in Fig. 6.4, and the local faradaic current production at chosen electrode positions as a function of time is shown in Fig. 6.5. A significant overshoot in current production is seen for $t < 1$ ms. This is due to consumption of surplus oxygen in the agglomerates. When elec-

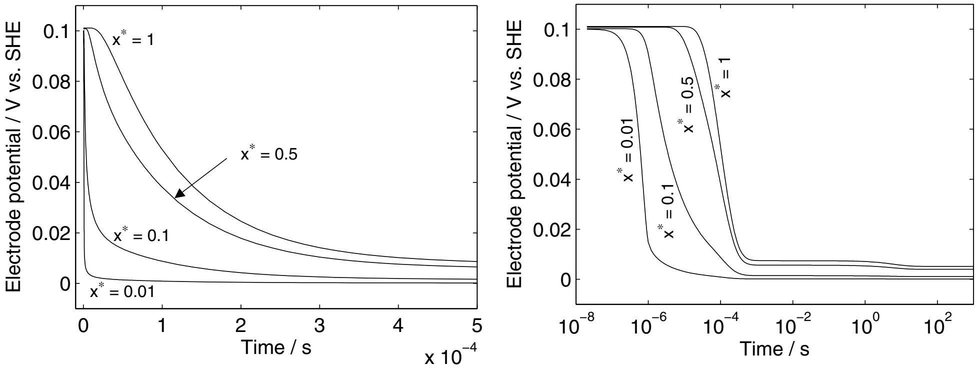

Figure 6.3: Time evolution of electrode potential at various positions in the electrode plotted on a linear (left) and logarithmic (right) time scale. Left figure shows the first 0.5 ms of the response.

trode potential changes faster than the response in oxygen diffusion, oxygen concentration is initially higher than at steady state, giving an initially high faradaic current production (ref. Eq. (6.19)). For $t > 1$ ms, electrode potential changes slower than the response in oxygen diffusion, and the overshoot disappears. For the remaining relaxation towards steady state, faradaic current production is controlled by the slow changes in electrode potential (ref. Fig. 6.3).

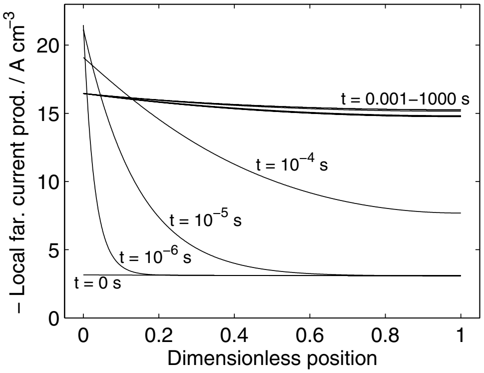

Figure 6.4: Local faradaic current production as a function of position for various time instances.

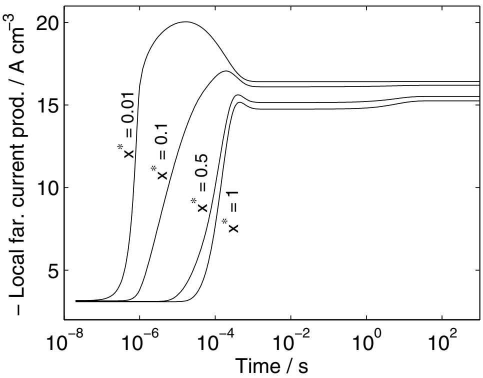

Figure 6.5: Local faradaic current production as a function of time for chosen electrode positions.

Fig. 6.6 shows how the oxygen profiles change with time at a chosen position in the electrode, and Fig. 6.7 presents the oxygen concentration at chosen positions as a function of time. Most of the change in oxygen concentration occurs before appr. 1 ms, which corresponds to the calculated time constant of oxygen diffusion. Fig. 6.7 shows that oxygen concentration starts to change later for higher values of x. This is due to the time it takes for electrode potential to propagate into the electrode. The slow relaxation towards steady state at appr. 50 s is due to the slow changes in faradaic oxygen consumption (ref. Fig. 6.5).

Fig. 6.8 shows that a cathodic step in electrode potential causes an increased gradient in electrolyte concentration in the electrode since the production and corresponding diffusion of OH^- ions increase. The final relaxation of c_e profiles to steady state occurs rather slowly and reaches steady state at appr. 60 s, corresponding well to the calculated time constant of ion diffusion.

Fig. 6.9 presents electrolyte concentration as a function of time for chosen electrode positions. In addition to the slow increase observed in Fig. 6.8, a dip in c_e appears shortly after the potential step. This dip appears at higher values of t for higher values of x^*. At $x^* = 1$, c_e reaches a minimum at appr. 0.3 ms before increasing towards steady state. In Fig. 6.10, the contributions to K^+ and OH^- concentration from each term in the mass balance at $x^* = 1$ are presented. This plot shows that a cathodic change in electrode potential for a chosen control volume causes absorption of K^+ ions in the double layer

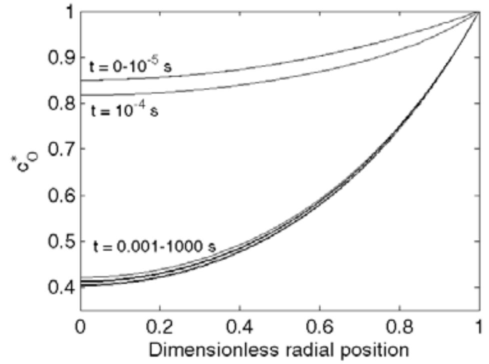

Figure 6.6: Dimensionless oxygen concentration as a function of radial position at $x^* = 0.5$.

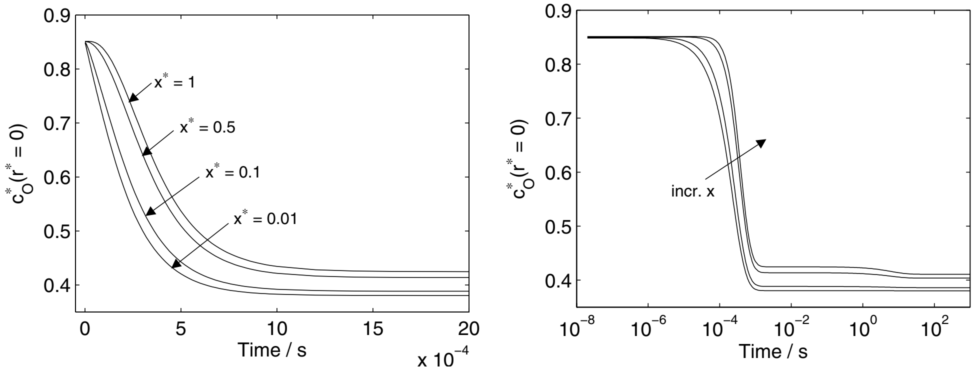

Figure 6.7: Time evolution of dimensionless oxygen concentration at the centre of an agglomerate at chosen positions in the electrode. The left figure shows the initial relaxation on a linear time scale, the right figure shows the complete relaxation on a logarithmic time scale.

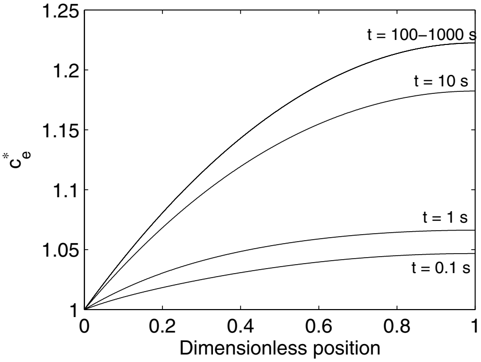

Figure 6.8: Electrolyte concentration profiles for t = 0.1-1000 s.

and desorption of OH^- ions. The corresponding decrease in charge in the electrolyte is balanced by a net flux of K^+ ions into the control volume and net flux of OH^- ions out of the control volume. Charge balance is thus obtained. Since the mobility of OH^- ions is larger than for K^+ ions, the amount of OH^- ions migrating out of the control volume is larger than the amount of K^+ ions migrating in. In sum, the concentration of K^+ and OH^- ions in the control volume decreases by equal amounts, causing a decrease in c_e. Thus, the decrease in c_e around 0.3 ms is attributed to a capacitive redistribution of ions. As this capacitive contribution dies out, faradaic production of OH^- ions becomes dominant, causing the subsequent increase in c_e.

Fig. 6.11 shows the response in total faradaic current density as a function of time. The main changes in faradaic current density take place for $t < 1$ ms where the change in electrode potential propagates through the electrode. The overshoot observed around 0.5 ms stems from consumption of surplus oxygen in the agglomerates (ref. Fig. 6.5).

Local capacitive current production is plotted for various time instances in Fig. 6.12. Due to the rapid change in electrode potential at $x = 0$ and the fact that we have not included any ohmic resistance in the solid phase of the electrode, the capacitive current is excessively large in this region. Including a finite ohmic resistance in the solid phase would give a more realistic value of the capacitive current. As the change in electrode potential propagates into the electrode, capacitive current is produced in the full depth of the electrode until the electrode potential has reached steady state.

Fig. 6.13 shows the total capacitive current of the electrode. This exhibits

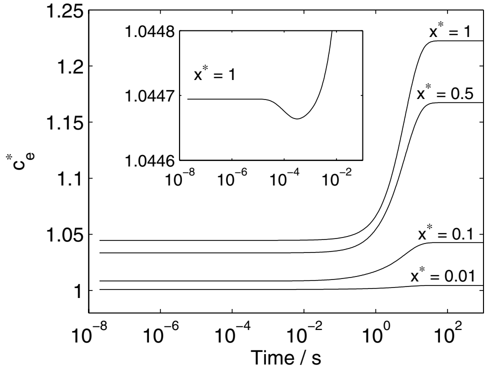

Figure 6.9: Electrolyte concentration as function of time for various positions in electrode. Inset zooms in on the curve for $x^* = 1$. Different processes dominate the time evolution in different time intervals.

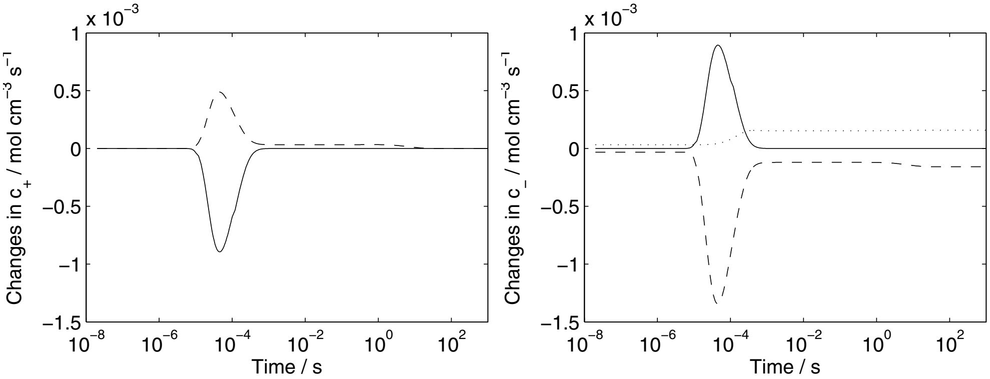

Figure 6.10: Contributions to changes in OH^- (left) and K^+ concentration (right) at $x^* = 1$. Solid line is the capacitive term, dashed line is the gradient in flux and dotted line is the faradaic term.

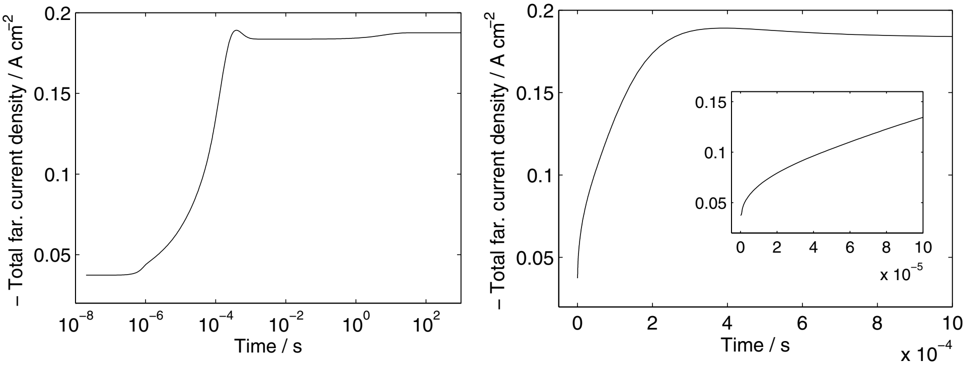

Figure 6.11: Time evolution of total faradaic current density of the electrode on a logarithmic (left) and linear (right) time scale. The linear plot shows the response up to 1 ms and the inset zooms in on the response up to 0.1 ms.

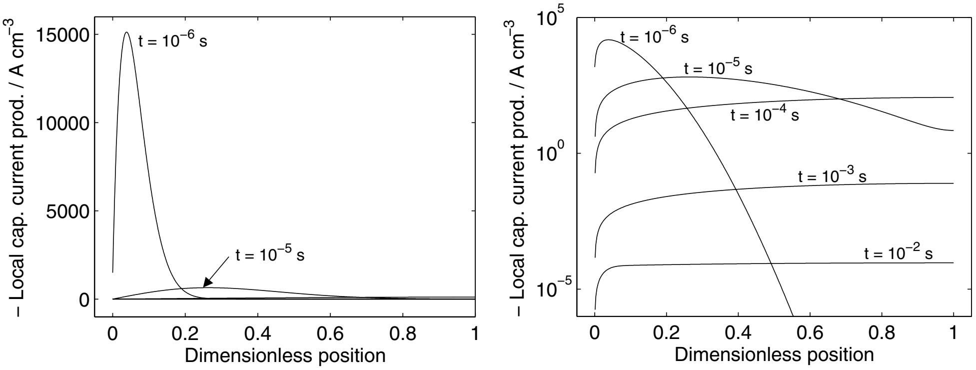

Figure 6.12: Local capacitive current production as a function of position for various time instances with linear (left) and logarithmic (right) y-axis. Peaks appear due to rapidly changing electrode potential.

an excessively large peak during the potential step (up to 1 μs) and dies out in appr. 1 ms. This corresponds well to to the time constant of potential propagation.

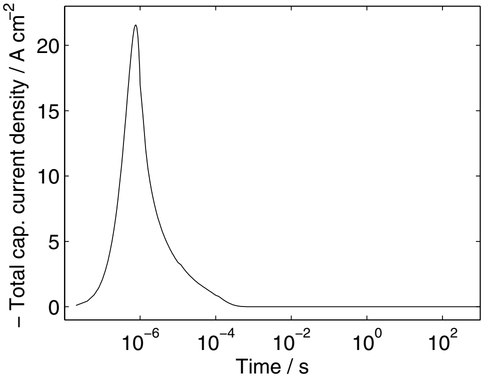

Figure 6.13: Time evolution of total capacitive current density of the electrode on a logarithmic time scale.

For the base case parameters, electrode potential propagation is a faster process than oxygen diffusion. By increasing $a_{dl}C_{dl}$ ten times, τ_V increases from 0.11 to 1.1 ms while the other time constants are unchanged. This means that we have a case where oxygen profiles reach steady state appr. four times faster than the electrode potential profiles. Increasing $a_{dl}C_{dl}$ also affects other variables than τ_V, but here we focus on the effects of a slower electrode potential response. These are most pronounced in the local faradaic current production which is plotted in Fig. 6.14. This figure also shows the response for a case with infinitely fast oxygen diffusion, obtained by using an analytical expression for I_a at steady state for a given electrode potential (ref. [10, Eq. 6]). Fig. 6.14 shows that the overshoot related to consumption of surplus oxygen becomes less pronounced when $\tau_V \approx 4\tau_O$ (ref. Fig. 6.5) and completely disappears for $\tau_O = 0$. This is reasonable since oxygen concentration is immidiately determined by the electrode potential when oxygen diffusion is infinitely fast.

The presence of an overshoot in the faradaic current thus indicates that the relaxation of oxygen concentration profiles is slower than changes in the electrode potential. For diagnostic purposes, this overshoot identifies a limitation in oxygen transport, and suggests that the transient response of the electrode can be enhanced by decreasing agglomerate size. However, as long

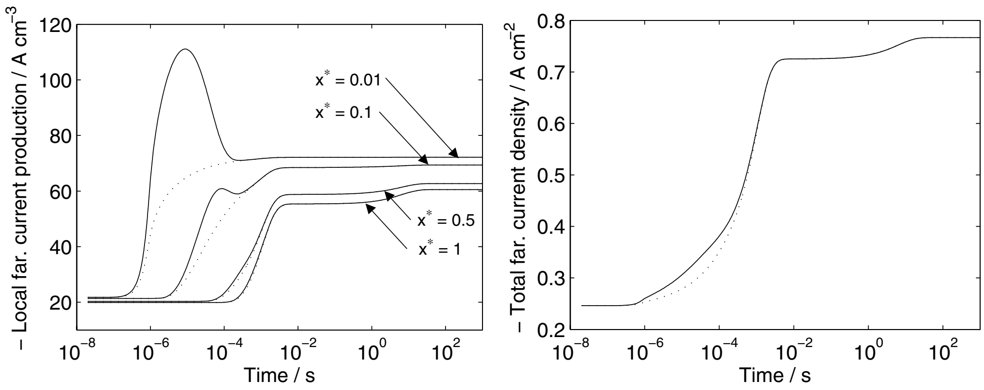

Figure 6.14: Results from a case where oxygen diffusion is a faster process than potential propagation. Left: Local faradaic current production as a function of time for chosen electrode positions. Solid line is the current response for a case where oxygen diffusion is appr. four times faster than potential propagation, and the dotted line represents current response when oxygen transport is infinitely fast. Right: Total faradaic current density.

as capacitive current dominates the total current density, faradaic current and the effects of oxygen transport can not be distinguished experimentally.

In a previous study by our group [25], we found that the response time of an AFC operated on pure oxygen and hydrogen was potential dependent. For steps to lower electrode potentials (higher current densities), response time decreased with increasing step size. This dependence was related to the potential dependence of the oxygen reduction reaction [25]. Our model reproduces a similar potential dependence for the relaxation of oxygen concentration. Fig. 6.15 presents the relaxation of oxygen concentration for steps to various electrode potentials using base case parameters. Since oxygen is consumed faster at a lower electrode potential (higher current), the response time decreases with increasing step size. This indicates that the potential dependence of the response time observed in [25] can be related to consumption of surplus oxygen in the catalyst layer. However, our model does not reproduce the same potential dependence in the response time of total faradaic current density since this is mainly controlled by the propagation of electrode potential through the electrode. Thus, the effect of a potential dependent response in oxygen concentration is masked by the slower change in electrode potential and gives only a minor overshoot in total faradaic current density (ref. Fig. 6.11).

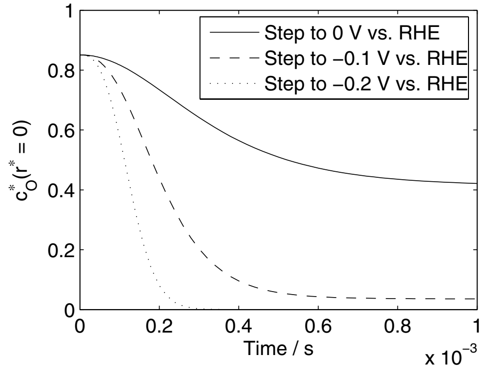

Figure 6.15: Time evolution of oxygen concentration at the center of an agglomerate at $x^* = 0.5$ for potential steps from 0.1 V to 0, -0.1 and -0.2 V vs. SHE.

6.8 Conclusion

An iso-thermal, one-dimensional, transient model of reactant concentration and electrode potential in an AFC cathode was developed based on a flooded-agglomerate description of electrode geometry. Mass balances of oxygen, K^+ and OH^- ions formed the coupled set of equations. Both faradaic and capacitive contributions to ionic source terms were included. Transport of oxygen in the microscopic, porous agglomerates was coupled to transport of ionic species and propagation of electrode potential in the macroscopic electrode structure through the faradaic current production in the agglomerate.

Model results showed that diffusion of ions was a considerably slower process than diffusion of oxygen and propagation of electrode potential. For base case parameters, time constants for oxygen diffusion, potential propagation and ion diffusion were 0.30 ms, 0.11 ms and 5.0 s, respectively. A smaller agglomerate radius gave faster response in oxygen concentration profiles, and a smaller electrode thickness gave faster response in ion diffusion and potential propagation. Also, a decreased double layer capacitance gave faster potential propagation. Structural parameters such as porosities had less pronounced influence on the time constants.

Simulation of a cathodic step in electrode potential with base case parameters showed that the response in total current density up to appr. 1 ms was controlled by the coupled effects of potential propagation and relaxation of oxygen concentration profiles. The final relaxation towards steady state at appr. 60 s was controlled by the relaxation of electrolyte concentration profiles. A dip in electrolyte concentration shortly after the potential step was related to a redistribution of ions in the double layer. An overshoot in faradaic current appeared around 0.5 ms due to an initially higher oxygen concentration in the agglomerates. For a case with infinitely fast oxygen diffusion, this overshoot did not appear. Experimental utilisation of this effect for diagnostic purposes may be difficult since the capacitive current masks the faradaic contribution up to 1 ms. Simulated response in oxygen concentration profiles suggested that the potential dependent response time found in previous studies can be related to consumption of surplus oxygen in the catalyst layer.

Acknowledgement

The Research Council of Norway and Aker Kværner Power & Automation Systems AS are kindly acknowledged for financial support.

Appendix A

Calculation of boundary conditions: The flux equations of K^+ and OH^- ions are given by Eq. (6.7). Solving the flux equation of OH^- ions with respect to $\partial\Phi_2/\partial x$, applying Eqs. (6.16) and (6.18), gives

$$\frac{\partial V}{\partial x} = \frac{N_- + \nu_- \tilde{D}_- \partial c_e/\partial x}{z_- \tilde{u}_- F \nu_- c_e} \tag{6.74}$$

This equation is used to eliminate the potential gradient in the flux equation of K^+ ions. Rearrangement gives

$$\frac{N_+}{\nu_+} - \left(\frac{z_+\tilde{u}_+}{z_-\tilde{u}_-}\right)\frac{N_-}{\nu_-} = \left(\frac{z_+\tilde{u}_+}{z_-\tilde{u}_-}\tilde{D}_- - \tilde{D}_+\right)\frac{\partial c_e}{\partial x} \tag{6.75}$$

Defining the flux of electrolyte as $N_e = N_+/\nu_+ = N_-/\nu_-$, we see from Eq. (6.75) that $N_e \propto \partial c_e/\partial x$. According to assumption 12 in Section 6.3.1, there is no flux of electrolyte into the oxygen gas channel, so

$$\left.\frac{\partial c_e}{\partial x}\right|_{x=L,\ t} = 0 \tag{6.76}$$

The ionic current density, i_2, is given by [19, Eq. 16.4]

$$i_2 = F(z_+ N_+ + z_- N_-) \tag{6.77}$$

Inserting flux equations, and applying Eqs. (6.16) and (6.18), we obtain

$$i_2 = F^2(z_+^2 \tilde{u}_+ \nu_+ + z_-^2 \tilde{u}_- \nu_-) c_e \frac{\partial V}{\partial x} - F(z_+ \nu_+ \tilde{D}_+ + z_- \nu_- \tilde{D}_-) \frac{\partial c_e}{\partial x} \tag{6.78}$$

Assumption 12 in Section 6.3.1 states that there is no ionic current density at $x = L$. Applying Eq. (6.76), we obtain

$$\left.\frac{\partial V}{\partial x}\right|_{x=L,\ t} = 0 \tag{6.79}$$

Appendix B

Technical specifications of Vulcan XC-72 provide the surface area of Pt per mass of catalyst, A_{Pt}, for a given weight percent of Pt, $\mathrm{wt\%_{Pt}}$. These quantities give the specific surface area of Pt as $A_{\mathrm{Pt}}/\mathrm{wt\%_{Pt}}$. Pt surface area per geometric electrode area is given by the product of this factor and the Pt loading of the electrode. If the geometric area of the electrode is A_{geom}, the geometric electrode area per total agglomerate volume is given by $A_{\mathrm{geom}}/(A_{\mathrm{geom}} L(1 - \epsilon_g))$. To obtain the Pt surface area per unit agglomerate volume, we assume that all Pt is located in the agglomerates. We thus obtain

$$a_{\mathrm{Pt}} = \zeta \frac{A_{\mathrm{Pt}} m_{\mathrm{Pt}}}{\mathrm{wt\%_{Pt}} L(1 - \epsilon_g)} \tag{6.80}$$

Here, the fraction ζ compensates for unavailable surface area.

Given the surface area of carbon per mass of catalyst and weight percent of carbon, the specific surface area of carbon can be calculated. Given this quantity and the mass density of carbon, ρ_{C}, we can calculate the volumetric surface area of carbon, given by $A_{\mathrm{C}} \rho_{\mathrm{C}}/\mathrm{wt\%_C}$. The total volume of carbon per agglomerate volume is $(1 - \epsilon_a)$, so the surface area of carbon per unit agglomerate volume is

$$a_{\mathrm{C}} = (1 - \epsilon_a) \rho_{\mathrm{C}} A_{\mathrm{C}} \mathrm{wt\%_C} \tag{6.81}$$

Again, we have compensated for unavailable surface area with the fraction ζ.

Appendix C

The time constant of oxygen diffusion is derived from a case where oxygen diffuses into an initially empty agglomerate without faradaic reaction. This can be expressed by Eq. (6.42) without the source term and with initial condition $c_O^*(r^*, t^* = 0) = 0$ and boundary condition $c_O^*(r^* = 1, t^*) = 1$. Crank [24, Eq. 6.18] expresses the analytical solution of this equation as an infinite sum, where each term is a product of a sinusoidal function and an exponential function. The first term of the sum has the largest time constant, which in dimensional form is

$$\tau_O = \frac{\epsilon_a t_{sc}}{\pi^2} = \frac{\epsilon_a R_a^2}{\pi^2 \tilde{D}_O} \tag{6.82}$$

In a similar manner, the time constant of electrode potential propagation is derived from Eq. (6.43) without the source term and assuming constant electrolyte concentration ($c_e^*(x^*) = 1$). Eq. 4.17 in Ref. [24] suggests the time constant

$$\tau_V = \frac{4 \cdot 1^2 \xi_2 t_{sc}}{\pi^2 \xi_3} = \frac{4(1-\epsilon_g) L^2 a_{dl} C_{dl} \left(\frac{1}{z_-\nu_-}\frac{dq_-}{dq} - \frac{1}{z_+\nu_+}\frac{dq_+}{dq} \right)}{\pi^2 F^2 c_e^b (z_+ \tilde{u}_+ - z_- \tilde{u}_-)} \tag{6.83}$$

Finally, Eq. 4.17 in Ref. [24] and Eq. (6.44) without reaction term and with constant electrode potential give the time constant of ion diffusion into an empty electrode

$$\tau_e = \frac{4 \cdot 1^2 \xi_6 t_{sc}}{\pi^2 \xi_8} = \frac{4\epsilon_l L^2 \left(\frac{1}{z_-\nu_-}\frac{dq_-}{dq} - \frac{1}{z_+\nu_+}\frac{dq_+}{dq} \right)}{\pi^2 \left(\tilde{D}_+ \frac{1}{z_-\nu_-}\frac{dq_-}{dq} - \tilde{D}_- \frac{1}{z_+\nu_+}\frac{dq_+}{dq} \right)} \tag{6.84}$$

List of symbols

A_{C}	surface area of carbon per mass catalyst material, cm^2 kg^{-1}
A_{Pt}	surface area of Pt per mass catalyst material, cm^2 kg^{-1}
a_a	active area per unit agglomerate volume, cm^{-1}
a_{C}	surface area of carbon per unit agglomerate volume, cm^{-1}
a_{Pt}	surface area of Pt per unit agglomerate volume, cm^{-1}
a_{dl}	double layer area per unit agglomerate volume, cm^{-1}
b	normal Tafel slope, V dec^{-1}

C_{C}	capacitance per surface area of carbon, F cm^{-2}
C_{Pt}	capacitance per surface area of Pt, F cm^{-2}
C_{dl}	capacitance per double layer area, F cm^{-2}
c_i	concentration of species i, mol cm^{-3}
c_e^b	bulk electrolyte concentration, mol cm^{-3}
c_O^s	surface concentration of dissolved oxygen, mol cm^{-3}
D_i	free stream diffusivity of species i, cm^2 s^{-1}
$\tilde{D}_i$	effective diffusivity of species i, cm^2 s^{-1}
dq_i/dq	change in double layer charge due to species i per unit change in solid phase charge
F	Faraday's constant, C mol^{-1}
$H(t)$	Heaviside step function
i_0	exchange current density, A cm^{-2}
I_a	current produced in one agglomerate, A
$i_{n,\ \mathrm{far}}$	faradaic current per unit active area, A cm^{-2}
i_{tot}	current per unit electrode area, A cm^{-2}
k	reaction rate constant, cm s^{-1}
L	electrode thickness, cm
m_{Pt}	Pt loading (mass Pt per unit electrode area), kg cm^{-2}
n	number of electrons transferred in electrode reaction
N_i	flux of species i, mol cm^{-2} s^{-1}
r	radial position in agglomerate, cm
R	universal gas constant, J K^{-1} mol^{-1}
R_a	agglomerate radius, cm
R_{Pt}	radius of Pt particle, cm
R_p	radius of agglomerate pore, cm
s_+	stoichiometric coefficient of species i
S_i	source term for species i, mol s^{-1} cm^{-3}
T	absolute temperature, K
t	time, s
t_{sc}	time scaling factor, s
u_i	mobility of species i, mol cm^2 J^{-1} s^{-1}
$\tilde{u}_i$	effective mobility of species i, mol cm^2 J^{-1} s^{-1}
V	electrode potential, V
V_0	electrode potential before step, V
V_1	electrode potential after step, V
V_{Pt}	volume of Pt particle, cm^3

V_{sc}	scaling factor for electrode potential, V
x	position in electrode, cm
z_+	charge number of K^+ ion
z_-	charge number of OH^- ion

Greek

ϵ_a	volume fraction of electrolyte filled pores in agglomerate
ϵ_g	volume fraction of gas phase in electrode
ϵ_l	volume fraction of liquid phase in electrode
ϵ_s	volume fraction of solid phase in electrode
ζ	correction factor compensating for unavailable surface area
Λ	equivalent conductance of electrolyte, Ω^{-1} cm^{-2} mol^{-1}
λ_+	equivalent conductance of K^+ ion, Ω^{-1} cm^{-2} mol^{-1}
λ_-	equivalent conductance of OH^- ion, Ω^{-1} cm^{-2} mol^{-1}
λ_+^0	equivalent conductance of K^+ ion at infinite dilution, Ω^{-1} cm^{-2} mol^{-1}
λ_-^0	equivalent conductance of OH^- ion at infinite dilution, Ω^{-1} cm^{-2} mol^{-1}
ν_i	number of ions i that a KOH molecule dissociates into
ρ_a	number of agglomerates per unit electrode volume, cm^{-3}
ρ_{C}	mass density of carbon (graphite), kg cm^{-3}
ρ_{Pt}	mass density of Pt, kg cm^{-3}
τ_a	agglomerate tortuosity
τ_e	time constant of ion diffusion, s
τ_l	electrode tortuosity
τ_O	time constant of oxygen diffusion, s
τ_V	time constant of electrode potential propagation, s
Φ_1	solid phase potential, V
Φ_1^{ref}	solid phase potential of the standard hydrogen electrode, V
Φ_2	liquid phase potential, V
ξ_k	dimensionless parameter number k

Subscripts

+	K^+ ion
-	OH^- ion
i	species number

e	electrolyte
O	oxygen
p	pore
Pt	platinum
C	carbon
Superscripts	
$*$	dimensionless quantity
ref	reference electrode

References

[1] G. F. McLean, T. Niet, S. Prince-Richard, and N. Djilali, *Int. J. Hydrogen Energy*, **27**, 507 (2002).

[2] E. Gülzow and M. Schulze, *J. Power Sources*, **127**, 243 (2004).

[3] C. Ziegler, H. M. Yu, and J. O. Sundmacher, *J. Electrochem. Soc.*, **152**, A1555 (2005).

[4] S. Kim, S. Shimpalee, and J. W. Van Zee, *J. Power Sources*, **135**, 110 (2004).

[5] W. Friede, S. Raël, and B. Davat, *IEEE T. Power Electr.*, **19**, 1234 (2004).

[6] D. J. L. Brett, S. Atkins, N. P. Brandon, V. Vesovic, N. Vasileiadis, and A. R. Kucernak, *Electrochem. Comm.*, **3**, 628 (2001).

[7] S. O. Morner and S. A. Klein, *J. Solar Energy Eng.*, **123**, 225 (2001).

[8] D. Natarajan and T. V. Nguyen, *J. Electrochem. Soc.*, **148**, A1324 (2001).

[9] J. Giner and C. Hunter, *J. Electrochem. Soc.*, **116**, 1124 (1969).

[10] M. L. Perry, J. Newman, and E. J. Cairns, *J. Electrochem. Soc.*, **145**, 5 (1998).

[11] M. C. Kimble and R. E. White, *J. Electrochem. Soc.*, **138**, 3370 (1991).

[12] M. W. Verbrugge and P. Liu, *J. Electrochem. Soc.*, **152**, D79 (2005).

[13] D. B. Sepa, M. V. Vojnovic, and A. Damjanovic, *Electrochim. Acta*, **25**, 1491 (1980).

[14] *COMSOL Multiphysics User's Guide*, version 3.2 (2005).

[15] P. N. Brown, A. C. Hindmarsh, and L. R. Petzold, *SIAM J. Sci. Comp.*, **15**, 1467 (1994).

[16] K. E. Brenan, S. L. Campbell, and L. R. Petzold, *Numerical solution of initial-value problems in differential-algebraic equations*, Elsevier, New York (1989).

[17] www.fuelcellstore.com, last visited April 2006.

[18] P. Gouérec, L. Poletto, J. Denizot, E. Sanchez-Cortezon, and J. H. Miners, *J. Power Sources*, **129**, 193 (2004).

[19] J. Newman and K. E. Thomas-Alyea, *Electrochemical systems*, John Wiley & Sons, Inc., Hoboken, New Jersey, 3rd ed. (2004).

[20] D. Dobos, *Electrochemical data*, Elsevier Scientific Publishing Company, Amsterdam (1975).

[21] A. J. Bard, editor, *Encyclopedia of electrochemistry of the elements*, Marcel Dekker Inc., New York and Basel (1973-1986).

[22] R. E. Davis, G. L. Horvath, and C. W. Tobias, *Electrochim. Acta*, **12**, 287 (1967).

[23] G. Aylward and T. Findlay, *SI Chemical Data*, John Wiley & Sons, 3rd ed. (1994).

[24] J. Crank, *The mathematics of diffusion*, Oxford University Press Inc., New York, 2nd ed. (1975).

[25] H. Weydahl, I. A. Lervik, A.-M. Svensson, T. Burchardt, S. Møller-Holst, B. Børresen, and G. Hagen, Fundamental studies of the dynamic behaviour of an alkaline fuel cell, Poster at 2004 Fuel Cell Seminar (2004).

Chapter 7

Conclusion

This thesis consists of five papers addressing the dynamic behaviour of AFCs and PEMFCs. The main conclusions are extracted below. For details, the reader is referred to the conclusions of each paper.

For successful implementation of fuel cells in applications with a rapidly varying power demand, it is important to characterise the dynamic behaviour of the fuel cell and specify how fast response that can be obtained. To address this issue, load steps with a short switching time were carried out supplying the fuel cell with excess amounts of reactant gases, using pure oxygen as cathode gas. These measurements were carried out on both a single AFC and PEMFC. Measurements showed that the response time for both technologies varied from milliseconds to seconds, depending primarily on the final state of the load step and secondarily on the step size. For steps from the same operating point, response time decreased near exponentially with the final cell voltage. Results from EIS indicated that the fuel cell response was controlled by the oxygen reduction reaction. Results from AFC and PEMFC measurements showed the same trends, but response times for PEMFC were faster than for AFC. Both technologies were sufficiently fast for automotive applications when oxygen was used as cathode gas.

In order to study the effect of mass transport on the dynamic response, current steps with short switching time were carried out on a PEMFC supplied with varying amounts of reactant gases and with a varying oxygen content in the cathode gas. The response up to appr. 0.01 s was unaffected by cathode gas composition or utilisation of the reactant gases. This part of the response was probably governed by double layer discharge and reaction with surplus oxygen residing in the catalytic layer. Mass transport limitations appeared as a further decrease in cell voltage up to appr. 0.1-2 s, depending on the applied current. The supply rate of air had a major impact on the dynamic response, while the supply rate of hydrogen was comparatively insignificant.

The load-following capability of the PEMFC was investigated applying a large-amplitude, sinusoidal current with varying DC value, amplitude and frequency. These experiments were carried out with both air and pure oxygen as cathode gases to investigate the effect of mass transport. Cell voltage followed the sinusoidal current without delay for frequencies up to 1-10 Hz in the voltage range dominated by ohmic losses. At cell voltages near the open circuit voltage, hysteresis in cell voltage appeared at frequencies higher than 0.1 Hz due to the sluggish PEMFC response in this voltage range. For frequencies higher than 100 Hz, most of the current was supplied by the charge double layer, causing a smaller amplitude in the cell voltage response. These measurements can be used to construct the PEMFC response to a given load profile using Fourier analysis.

In order to look into local dynamic processes and how they contribute to measurable quantities, a transient model of an AFC cathode was developed. Model results showed how transport of oxygen, ions and propagation of electrode potential contribute to the total faradaic and capacitive current. Ion diffusion was identified as a slow process with a characteristic time constant of 5 s for base case parameters. Oxygen diffusion and potential propagation were fast processes with characteristic time constants around 0.1 ms. An increasing agglomerate radius and double layer capacitance increased the time constants of oxygen transport and potential propagation, respectively. Coupled effects of oxygen transport and rapid changes in electrode potential gave an overshoot in faradaic current, but the large capacitive current masked this effect. A potential dependent response time for the oxygen concentration profiles appeared due to consumption of surplus oxygen in the agglomerates.

Chapter 8

Further work

This work has answered some questions regarding the dynamic behaviour of fuel cells, but also raised new issues. On basis of the reported results, the following directions for further work are suggested:

- Long-term effects of dynamic operation on fuel cell performance were not addressed in this work and should be systematically investigated. If dynamic operation accelerates performance degradation, the fuel cell must be protected from harmful power variations. Especially, long-term effects of ripple currents from power electronics should be assessed, since these represent a probable driving force for degradation.

- A high flow rate of air was found to improve the dynamic performance of the PEMFC. However, high flow rates cause large parasitic power losses in the mass flow controllers. Based on reported results, control regimes and criteria for optimal selection of flow rates should be developed for practical applications.

- Transient step measurements mainly addressed steps from low to high power outputs. A more thorough mapping of steps back to low power outputs should be carried out to identify possibly harmful power over- or undershoot at low load.

- A linearly decreasing cell voltage with time was observed for current steps with air as cathode gas. This effect was not explained and should be further investigated.

- Oscillations in cell voltage were observed after current steps with air as cathode gas. The origin of these oscillations should be identified. If formation of water droplets affects the frequency of the oscillations, this effect may be used for diagnostic purposes to study transport of liquid water in the cathode.

- Cell voltage response to a sinusoidal current load should be measured in a wider power range, including the region where mass transport limitations dominate the voltage loss. This will give information about the load-following performance at high power outputs. A set of measured cell voltage responses to sinusoidal currents with various DC values, amplitudes and frequencies can be used as basis for calculation of PEMFC response to a given load profile using Fourier analysis. Calculated results can be compared to measured PEMFC response to the same load profile.

- Measurements with AFC should be repeated for a set of electrodes with higher performance to obtain a more representative data set. By comparing the transient response of AFCs and PEMFCs, advantages or disadvantages of using a liquid vs. a polymer electrolyte under dynamic operation can be addressed.

- A comparison of measured AFC and PEMFC response indicated that the response time is inversely proportional to the current density after the step and proportional to the non-ohmic change in cell voltage. This hypothesis can be tested by comparing theoretical predictions with reported data.

- The reported model has a great potential for further development and use. A variety of potential perturbations and parameter sets can be applied as model input, suggesting how mass transport and potential propagation affect measurable quantities under various control regimes. Using a small-amplitude, sinusoidal potential perturbation, the electrode impedance can be calculated. This opens for various diagnostic tools that can be used in relation to experimental investigations.

- Some modifications of the model would improve the significance of calculated results: A solid phase ohmic resistance should be included to obtain a more realistic capacitive current and potential distribution. Also, diffusion of oxygen to the agglomerate surface should be accounted for. Kinetic expressions valid in the potential range near open circuit should be included to extend the range of the model. One should also consider replacing the dilute solution flux equations with relations from concentrated solutions theory.